# Multistage Magnetic Detwinning in Eu-based Iron Pnictides

## Dissertation

zur Erlangung des akademischen Grades

Dr. rer. nat.

eingereicht an der

Mathematisch-Naturwissenschaftlich-Technischen Fakultät

der Universität Augsburg

von

**Jannis Maiwald**

Augsburg, April 2017

Gutachter:

Prof. Dr. Philipp Gegenwart
PD Dr. Hans-Albrecht Krug von Nidda
Prof. Dr. Michael Lang

Tag der mündlichen Prüfung: 22. Juni 2017

*"Writing is easy. All you have to do is cross out the wrong words."*

Mark Twain

# Contents

# List of Figures

# List of Tables

Chapter 1

# Introduction

Basic research is the foundation of technological and social progress. The discipline of condensed matter physics and solid state physics in particular, led to a host of technological advances, for instance in the fields of transistors, semiconductors, and superconductors (SCs). Today, transistors and semiconductors are ubiquitous, as we encounter them in electronics, personal computers, smartphones, and other electronic devices, which continue to transform our societies. SCs, on the other hand, have also found a wide range of applications, despite their yet low transition temperatures. They are used, e. g., in extremely sensitive SQUID magnetometers, strong electromagnets needed for maglev trains, Magnetic Resonance Imaging and Nuclear Magnetic Resonance devices, magnetic confinement fusion reactors, such as the tokamaks, particle accelerators, electric motors and generators, etc. The technical applications, for materials without any electrical resistance, seem endless. Without basic research, the applied sciences would not have been able to make these incredible technological advances.

Superconductivity has been in the focus of solid state research since its discovery in 1911 [1]. After almost 50 years of research this intriguing phenomenon could finally be described microscopically, when Bardeen, Cooper, and Schrieffer presented their BCS theory in 1957 [2]. Following a phonon-mediated attractive interaction, electrons at the Fermi level can condense into Cooper pairs, which are the superconducting charge carriers of SCs. Materials that feature this pairing mechanism are called conventional SCs. Generally, there is no intrinsic upper limit to the transition temperature $T_c$ in these systems [3]. In fact, the current record holder hydrogen sulfide ($H_2S$), which becomes superconducting at an astonishing 203 K under extremely high pressure ($\sim$ 150 GPa), is conventional in nature [4]. However, due to, among other things, a relatively weak electron-phonon interaction, the $T_c$ of conventional SCs is typically limited to a few

tens of Kelvin. Cooling any material to such low temperatures is costly and technically challenging.

The situation was somewhat mitigated by the discovery of the copper-oxide *high-temperature superconductors* in 1986 [5]. With a $T_c$ of the order of 100 K they can be cooled using liquid nitrogen, which is comparatively inexpensive. The most recently discovered class of high-$T_c$ materials are the iron-based superconductors (IBSCs) [6, 7]. Despite having relatively moderate $T_c$'s, they are, in many aspects, similar to the copper-oxide SCs and have received much attention from the scientific community in the past years. However, the iron-based and copper-oxide systems belong to the class of unconventional SCs, in which the formation of Cooper pairs is not mediated by phonons. Even after decades of research, in the case of copper-oxide SCs and almost 10 years of research on the IBSCs, the microscopic paring mechanism of these systems—if a single one exits—still remains a mystery. Although the transition temperatures, even for the conventional SCs, continue to increase [8], an understanding of the physics of the unconventional SCs is paramount for a directed approach to further elevate $T_c$ in the future and perhaps to even overcome the gap to the much desired room-temperature superconductor one day.

One of the major problems with investigating the IBSCs is the formation of structural twin domains in their orthorhombic crystal phase. These domains obscure the in-plane anisotropy that was discovered in these materials. However, this anisotropy is closely related to the unusual antiferromagnetic ground state of the IBSCs and hence important to understand. Therefore, the IBSCs need to be detwinned, i. e. forced into a mono-domain state, if one is to probe their intrinsic behavior. This is typically achieved by application of uniaxial pressure through a mechanical clamp. This, however, is not only cumbersome to implement in a cryogenic environment, but also reportedly alters the physical properties of these materials and hence needs to be considered carefully. Nonetheless, it was, until now, the only practical detwinning method, because detwinning through application of magnetic field was unfeasible, considering the required fields of the order of 30 T.

This thesis reports the discovery of an unusual and unexpected physical phenomenon, namely, the *multistage magnetic detwinning* of $EuFe_2As_2$, which sets in at miniscule magnetic fields of the order of only 0.1 T. Moreover, the induced detwinning is persistent upon removal of the field and even subsequent heating of the material up to temperatures around 190 K, where the structural transition to the tetragonal phase occurs and the twin domains vanish. This observation opens an entirely new avenue for the investigation of the ground state of these materials, which is deemed crucial for the understanding of the physics of the IBSCs. Aside from the experimental evidence, this thesis also presents a novel microscopic theory of this effect, that fully and quantitatively describes

the phase-diagram of this system in its full richness and complexity. It is organized as follows:

Chapter 2 introduces basic concepts important for the understanding of this work. It includes a brief introduction to magnetism, superconductivity, crystal twinning, and the log-normal distribution. While the interplay between magnetism and structural aspects is central to this thesis, superconductivity, and, in particular, the difference between conventional and unconventional superconductivity, is introduced mainly for a better understanding of the review of the IBSCs that follows in Chapter 4.

Chapter 3 presents the experimental methods used to synthesize, characterize, and experimentally investigate the Eu-based iron pnictides. In particular, the synthesis of single crystals of the parent compound $EuFe_2As_2$, as well as its magnetically diluted variants $Eu_{1-x}Ba_xFe_2As_2$ and $Eu(Fe_{1-x}Ru_x)_2As_2$, is discussed. Subsequently, the conditions and parameters of the various characterization techniques employed during this research project are presented.

In order to give an overview of the current research field, a broad review of the IBSCs with a focus on the Eu-based iron pnictides is given in Chapter 4.

The general characterization of the synthesized materials is presented in Chapter 5. It includes structural and chemical aspects, such as the evolution of lattice parameters and doping concentrations. Transport and thermodynamic measurements are also included.

The main results of this project are discussed in Chapter 6. It is divided into three main parts. The first part introduces a novel microscopic theory for the magnetically induced detwinning effect. This is followed by a presentation of the experimental evidence, including indirect evidence from transport, dilatometric, and magnetic measurements, as well as direct evidence from neutron scattering. The last part elaborates on the data analysis, leading to the determination of the relevant coupling constants and the detwinning barrier. The chapter concludes with a consistency check of the theory and a summary.

In Chapter 7, the evolution of the magnetic detwinning effect with doping is briefly presented. Three types of doping are examined: Ba-doping on the Eu site (magnetic dilution), Ru-doping on the Fe site (magnetic dilution), and P-doping on the As site (chemical pressure), before the thesis concludes with a summary, given in Chapter 8.

Chapter 2

# Basic Concepts

This chapter briefly presents basic concepts important for this thesis. It serves not only as a prelude for the discussion of the multistage magnetic detwinning effect in $EuFe_2As_2$ presented in Chapter 6 and Chapter 7, but it should also be helpful for Chapter 4, which introduces the iron-based superconductors. The chapter starts with a concise review of magnetism, focusing on antiferromagnetism, spin-density waves, and the biquadratic coupling. This is followed by a succinct introduction to superconductivity, the log-normal distribution, and crystal twinning.

## 2.1 Magnetism

In the following, the most common types of magnetism will be introduced. The discussion conceptually follows that found in Ref. [9], while some figures in this section were inspired by Ref. [10]. This section concludes with a brief discussion of spin-density waves and the biquadratic coupling.

### 2.1.1 Common Types of Magnetism

#### Diamagnetism

Diamagnetism is characterized by a negative and temperature-independent susceptibility ($\chi < 0$) as depicted in Fig. 2.1. It occurs due to screening currents, which are a consequence of an applied external magnetic field in accordance with Lenz's law. Therefore, all materials exhibit diamagnetism and a small diamagnetic contribution to the total magnetization of any given material is always present.

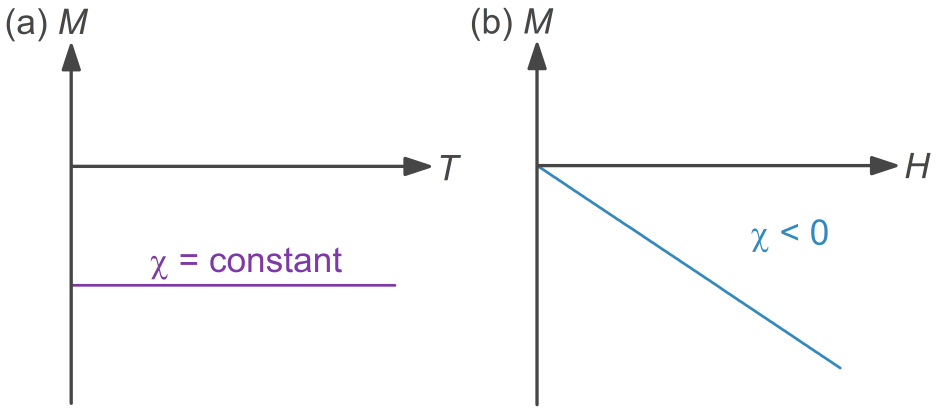


FIGURE 2.1: Magnetization of a typical diamagnet (a) for constant magnetic field as a function of temperature and (b) at constant temperature as a function of applied magnetic field.

In most materials this effect is small. Carbon and Bi, for instance, are among the strongest diamagnets with a susceptibility of the order of $\chi \sim -10^{-4}$ (in SI-units), but superconductors in the Meissner phase, are perfect diamagnets with a susceptibility of $\chi = -1$.

**Paramagnetism**

Paramagnets are materials with disordered non-interacting magnetic moments and hence do not show any spontaneous magnetization. The magnetic moments can either stem from localized unpaired electrons, or from the itinerant electrons of the electron gas. The latter is referred to as "Pauli paramagnetism", while the former is typically referred to as just "paramagnetism".

The Pauli paramagnetism is weak, because only electrons close to the Fermi energy contribute. An applied magnetic field $H$ lifts the degeneracy of the spin-up and spin-down states, leading to an unequal distribution of electrons per unit volume with spin up ($n_\uparrow$) and spin down ($n_\downarrow$) and consequently to a net magnetization $M$. The susceptibility

$$\chi_\mathrm{P} = \frac{M}{H} = \frac{\mu_\mathrm{B}(n_\uparrow - n_\downarrow)}{H} \approx \frac{3n\mu_0\mu_\mathrm{B}^2}{3E_\mathrm{F}}$$

is positive and temperature independent in the degenerate limit $\mu \gg k_\mathrm{B}T$, with chemical potential $\mu$, Bohr magneton $\mu_\mathrm{B}$, carrier density $n$, Bolzmann constant $k_\mathrm{B}$, magnetic constant $\mu_0$, Fermi energy $E_\mathrm{F}$, and temperature $T$.

The paramagnetism of local magnetic moments is much stronger in comparison, as it

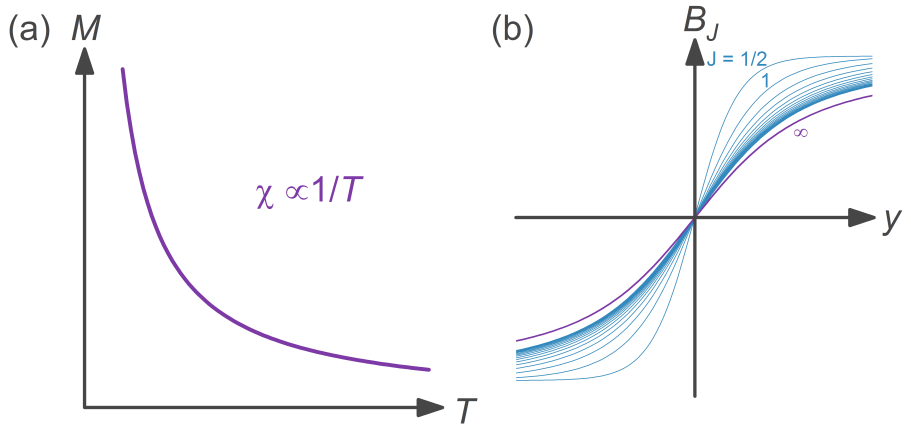


FIGURE 2.2: The magnetization $M$ of a paramagnet follows the (a) Curie law $\chi \sim 1/T$. (b) The field dependence is determined by the Brillouin function (shown for various $J$), where $y \sim JH/T$ is the ratio between Zeeman energy and thermal energy.

involves unpaired electrons from each magnetic lattice site in the bulk. These randomly distributed moments will gradually follow an applied magnetic field and eventually align in field direction in order to minimize their Zeeman energy. However, thermal fluctuations compete with this field-induced polarization, as they tend to randomize magnetic moments. The susceptibility of a paramagnet is, therefore, positive ($\chi > 0$) and depends on the ratio between the Zeeman energy and the thermal energy: $y = E_{\text{mag.}}/E_{\text{therm.}} \sim JH/T$, with $J$ the total angular momentum, $H$ the magnetic field and $T$ the temperature. The magnetization $M = M_{\text{s}} B_J(y)$ is given by the Brillouin function:

$$B_J(y) = \frac{2J+1}{2J} \coth\left(\frac{2J+1}{2J} y\right) - \frac{1}{2J} \coth\left(\frac{y}{2J}\right),$$

with the saturation magnetization $M_{\text{s}}$. For constant $H$ (and $J$) the temperature-dependent magnetization follows an $1/T$ behavior (Fig. 2.2a), while the field-dependent magnetization at constant $T$ is given by the Brillouin function (Fig. 2.2b), which is linear for small $y$.

**Ferromagnetism**

Ferromagnets are materials that show spontaneous magnetization below a critical temperature $T_{\text{C}}$. This is due to exchange interaction ($J_{ij} < 0$), which favors the parallel alignment of magnetic moments.

In real materials, magnetic domains are formed. Inside a domain all spins point in the same direction, but across the bulk, the orientation of different domains is such that the net magnetization of the material is zero. The domain walls are usually pinned, due to crystal defects, strain, etc. and arbitrarily small magnetic fields can not reorient the

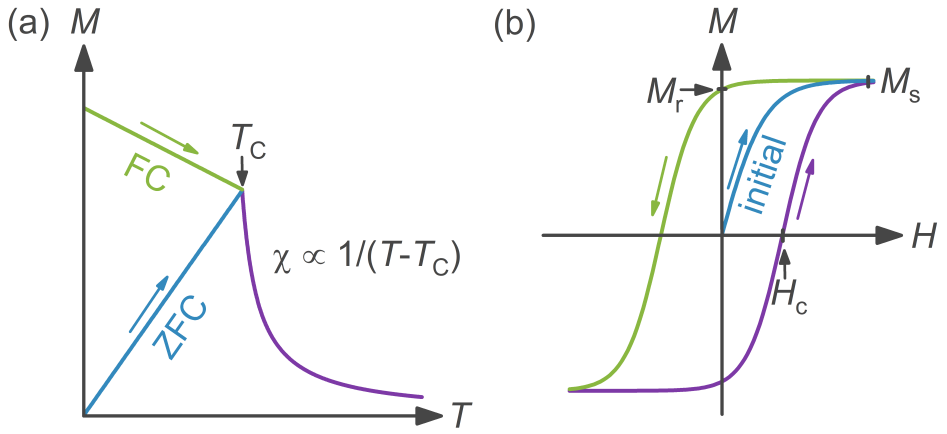


FIGURE 2.3: Magnetization $M$ of a ferromagnet. (a) For small magnetic fields $M(T)$ depends on whether the sample was field-cooled (FC) or zero-field-cooled (ZFC). Above $T_C$ it follows the Curie-Weiss law $\chi \sim 1/(T-T_C)$. Note, this is the most basic mean field behavior. (b) The field-dependent magnetization below $T_C$ shows hysteresis, due to the irreversible movement of magnetic domain walls. Characteristic points are the saturation magnetization $M_s$, remanent magnetization $M_r$ and coercive field $H_c$. Furthermore, the initial magnetization curve is never recovered in further field cycles. Arrows indicate increasing or decreasing field.

domains, as a consequence. This leads to interesting effects in the $M(T)$ and $M(H)$ curves.

The $M(T)$ curve under application of a small magnetic field (Fig. 2.3a) depends on whether the material was cooled in field (FC) or in zero field (ZFC). Starting from $T = 0$, the distribution of the magnetic domains results in a vanishing magnetization after ZFC. A small magnetic field alone can not overcome the pinning energies of the domains, but as thermal fluctuations increase with increasing temperature, the effective pinning energies reduce. Subsequently, domains can reorient parallel to the field, and the magnetization increases. In the case of FC, the broken rotational symmetry, due to the applied magnetic field, leads to a preferred direction of alignment of the spins during cooling through $T_C$. Consequently, the magnetization in the ordered phase is higher compared to ZFC, but reduces with increasing $T$, as thermal fluctuations tend to disorder the spin alignment. Above $T_C$, in the paramagnetic state, the susceptibility follows the Curie-Weiss law $\chi \sim 1/(T - T_C)$.

The $M(H)$ curve below $T_C$ exhibits hysteresis (Fig. 2.3b), due to the irreversible movement of the magnetic domains. Initially, after ZFC below $T_C$ no net magnetization is observed. With increasing field, $M$ increases as domain walls start to move when their respective pinning energies are overcome and the moments align in field direction. At $M_s$ all moments are aligned. With decreasing field, most moments stay in field direction and the system exhibits a remanent magnetization $M_r$ at $H = 0$. Only an additional (negative) field, called coercive field $-H_c$, removes the remanent magnetization. This

behavior is repeated in the opposite direction with further field cycling. Due to this irreversible behavior the initial magnetization curve is never recovered.

**Antiferromagnetism**

An antiferromagnet, on the other hand, favors an antiparallel spin alignment ($J_{ij} > 0$). It can often be thought of as a system with two interpenetrating, ferromagnetic sublattices, which are antiparallel to each other. The susceptibility also follows Curie-Weiss behavior $\chi \sim 1/(T-\theta)$ above the magnetic ordering. However, the Weiss temperature $\theta$ is negative and the ordering temperature $T_\mathrm{N} = -\theta$ is called Néel temperature. The magnetization below $T_\mathrm{N}$ depends strongly on the direction of the applied magnetic field. The molecular field of a given crystal typically results in a preferred axis the moments tend to align along, called *easy axis*, while the less favorable directions of alignment are consequently labeled *hard axes*. The corresponding energy term is called magnetocrystalline anisotropy $\Delta$. Furthermore, one needs to distinguish between the application of small and large fields, as in the case of a ferromagnet, because the associated Zeeman energy has to be measured against $\Delta$ and the antiferromagnetic (AF) exchange energy.

The magnetization for small magnetic fields applied along the easy axis ($\chi_\parallel$) at $T = 0$ is zero (Fig. 2.4a) as both sublattices are fully saturated and hence cancel each other out. In particular, small fields can not counteract the molecular field of the antiparallel sublattice, and hence have no effect on $M$. In the perpendicular case ($\chi_\perp$), the moments of both sublattices will deflect slightly from their initial resting position, giving rise to a

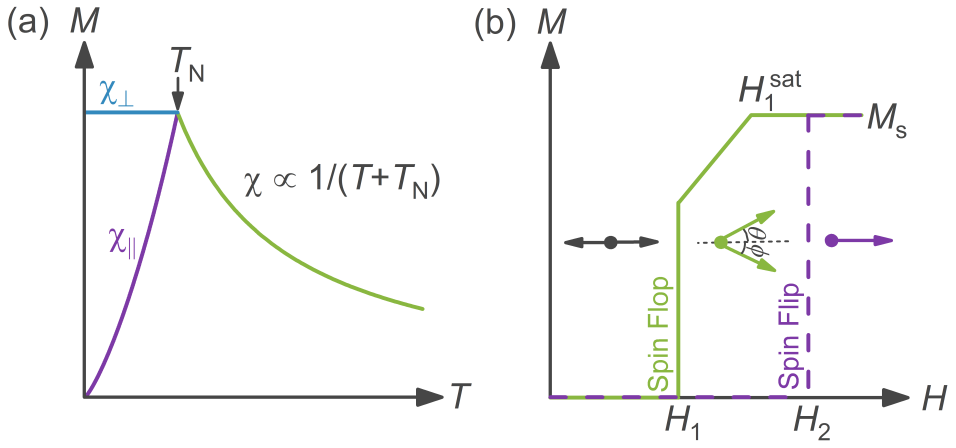


FIGURE 2.4: Magnetization $M$ of an antiferromagnet. (a) For small fields the temperature-dependent $M$ is strongly direction-dependent below the ordering temperature $T_\mathrm{N}$. Above $T_\mathrm{N}$ it follows the Curie-Weiss law. Note, this is the most basic mean field behavior. (b) For high fields parallel to the easy axis at $T = 0$ the field-dependent $M$ shows a step at the spin-flop field $H_1$, followed by a gradual increase until saturation ($M_\mathrm{s}$) sets in at $H_1^\mathrm{sat}$. If the magnetocrystalline anisotropy is strong the spins can also directly 'flip' into the FM configuration (violet, dashed line), shown here for $H_2 > H_1$. Colored arrow indicate the spin alignment in the respective field regions.

net magnetization. When increasing the temperature towards $T_N$, thermal fluctuations effectively start to decrease the molecular field. The effect on $\chi_\perp$ is negligible as both sublattices are affected symmetrically. However, $\chi_\parallel$ is strongly influenced by this, because the magnetic field affects the spins of the sublattices asymmetrically, thus enhancing the moments parallel to the field and reducing those that are antiparallel.

The field-dependent magnetization for the parallel configuration (Fig. 2.4b) exhibits discontinuous changes. Initially, $H$ is weak compared to $\Delta$ and the AF exchange, therefore, the spins stay locked in their antiparallel configuration (black arrows, field enters from the left like the abscissa) below a certain field $H_1$. At $H_1$, however, the associated energies are overcome and the antiparallel spins suddenly change into a different configuration (green arrows). Due to the AF exchange, the spins that were already parallel to the field direction are now deflected from their initial positions. This scenario is called a *spin-flop* transition. With further increasing field the moments gradually reduce their Zeeman energy by rotating towards the FM configuration until they reach saturation at $H_1^{\mathrm{sat}}$. However, if the magnetocrystalline anisotropy is strong ($\Delta \geq J$) all spins directly flip into the parallel configuration. This is called a *spin-flip* transition. This behavior is in stark contrast to the magnetization perpendicular to the easy-axis, which is continuous and linear. More details can be found in Refs. [9, 11].

### 2.1.2 Spin-Density Waves

Typically, magnetism is called *local*, when the magnetic phase emerges out of (localized) magnetic moments that are already present in the disordered (paramagnetic) phase. Accordingly, for *itinerant* magnetism, no localized magnetic moments need to be present in the disordered state. The latter type of magnetism is the result of a spontaneous self-organization of the itinerant electron spin density. The resulting periodic spatial modulation is called spin-density wave (SDW) [12, 13], which is closely related to the charge-density wave (CDW). The SDW arises from an instability of the electronic system due to Fermi surface (FS) nesting.

Fermi surface nesting implies that certain parts of the FS are connected by a so-called nesting vector $\mathbf{Q} = 2\mathbf{k}_F$. In other words, different parts of the FS are geometrically similar. This effect is strongest in low-dimensional systems. In 1D, the nesting between the point-like FSs is perfect, while in higher spatial dimensions, it becomes easier for the electrons to avoid each other and nesting is reduced.

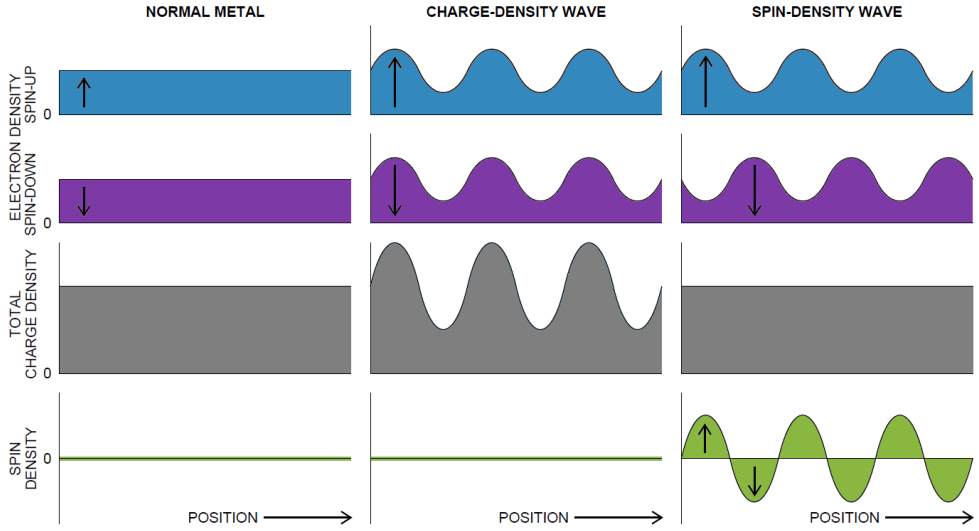


FIGURE 2.5: Illustrations of the electronic charge and spin densities in the normal (metallic), charge-density wave (CDW) and spin-density wave (SDW) states. The SDW can be thought of as two superimposed CDWs—one for each spin channel—with shifted peak positions. Adapted from Ref. [14].

In a normal metal, the conduction electrons with spin up and spin down are equally distributed (Fig. 2.5), and the total spatial distribution of the charge-carrier density

$$\rho(\mathbf{r}) = \rho_{\uparrow}(\mathbf{r}) + \rho_{\downarrow}(\mathbf{r})$$

is flat. For a SDW the carrier density is modulated

$$\rho_{\uparrow(\downarrow)} = \frac{1}{2}\rho_0(\mathbf{r})[1 \pm A\cos(\mathbf{Q}\mathbf{r})]$$

with the amplitude $A$ and can be thought of as two superimposed CDWs, in which the spin density for each spin channel is modulated with translated peak positions. Since the wavelength $\lambda = 2\pi/Q$ is determined by the FS [15], the SDW state may be incommensurate with the crystal lattice, i. e. the periodicity of the lattice and the SDW are no rational multiples of each other. Due to the periodic modulation a gap in the electronic density of states opens, like in the case of superconductors or CDWs.

The canonical example of a purely itinerant (SDW) antiferromagnet is elemental chromium [16], while the parent compounds of the cuprate superconductors are examples of systems with local magnetic character. Generally. localized and itinerant magnetism can be thought of as opposing ends of a continuum. A given system can be located somewhere in between and might consequently exhibit characteristics of both. We will see later in Chapter 4 that this is the case for the iron-based superconductors and one of the reasons for their intriguing physics.

### 2.1.3 Biquadratic Coupling

The Hubbard model is probably the most famous and simplest model of correlated electrons. Although highly oversimplified, it captures a wide range of interesting phenomena, such as magnetic ordering, a metal-insulator transition, and superconductivity, to name just a few. The defining Hamiltonian is comprised of two terms, a single particle part and a two-particle interaction. The first one is often called kinetic energy and models electron hopping on the lattice. It, therefore, describes a tendency to delocalize electrons into itinerant Bloch states, which leads to metallic behavior. The second part represents the electron-electron interaction, which, in this model, is approximated by a local, i. e. on-site Coulomb interaction with strength $U$. This interaction favors the localization of electrons to the lattice sites and thus drives the transition to a Mott insulator. The one-band Hubbard Hamiltonian is given by

$$\mathcal{H} = -\sum_{\langle ij\rangle,\sigma} t_{ij}(c^{\dagger}_{i\sigma}c_{j\sigma} + \text{h.c.}) + U\sum_{i} n_{i\uparrow}n_{i\downarrow}$$

where $c^{\dagger}_{i\sigma}$ creates an electron with spin $\sigma$ at lattice site $i$, $c_{j\sigma}$ removes an electron with spin $\sigma$ from site $j$ and h.c. denotes the Hermitian conjugate, i. e. $c^{\dagger}_{j\sigma}c_{i\sigma}$, while the sum over $\langle ij\rangle$ runs over pairs of atoms and $n_{i\sigma} = c^{\dagger}_{i\sigma}c_{i\sigma}$ is the occupation number operator, i. e. counts the number of electrons with spin $\sigma$ on site $i$. Finally, $t$ is the so-called hopping parameter, and $U$ is sometimes referred to as Hubbard-$U$.

Under certain circumstances (half-filling, $t_{ij}/U \ll 1$) the low-energy excitations of the Hubbard model can be mapped [17] to the well-known Heisenberg model

$$\mathcal{H} = J\sum_{\langle ij\rangle} \mathbf{S}_i \cdot \mathbf{S}_j,$$

with the spin operators $\mathbf{S}_k$ and coupling constant $J = 4t^2_{ij}/U$ (bilinear exchange). In fact, the Heisenberg model is only the leading term of the effective Hubbard Hamiltonian, i.e the expression for $J$ is derived from second-order perturbation theory in $t_{ij}/U$. Higher-order terms include so-called ring exchange processes, biquadratic interactions, etc.

In a general form, the isotropic pairwise coupling between two spins of magnitude $S$ can be expressed by

$$\mathcal{H} = J_1\mathbf{S}_1 \cdot \mathbf{S}_2 + J_2(\mathbf{S}_1 \cdot \mathbf{S}_2)^2 + ... + J_{2S}(\mathbf{S}_1 \cdot \mathbf{S}_2)^{2S},$$

with the exchange constants $J_i$. The first term, as just mentioned, is the typical bilinear Heisenberg term, while the second term is called biquadratic coupling. It is the essential isotropic correction to the standard Heisenberg Hamiltonian, because higher powers of

$(\mathbf{S}_1 \cdot \mathbf{S}_2)$ appear in higher orders of perturbation theory [17]. Such a correction was observed experimentally for the first time for $Mn^{2+}$ ions ($S = 5/2$) in antiferromagnetic MnO [18] and in Mn-doped MgO [19], where the biquadratic coupling constant is roughly 20 times smaller than the leading Heisenberg term, i. e. $J_2/J_1 \approx 0.05$.

Soon after the discovery of the iron pnictides, a biquadratic coupling between the Fe-3$d$ moments was proposed by Yaresko *et al.* in order to explain the observed collinear stripe AF order in the SDW state [20] (see also Chp. 4). Its strength has been estimated to be of the order of a few tens of meV, which is sizable compared to the ∼30 meV found for the nearest-neighbor bilinear exchange constant on the Fe square lattice [21, 22]. This biquadratic coupling is likely rooted in the multiorbital nature of the iron pnictides [23], while the coupling itself is intimately related to their nematic behavior [24].

As I will discuss in more detail throughout this thesis, we propose such a biquadratic interaction between the Eu and Fe moments in $EuFe_2As_2$, which can explain the observed multistage magnetic detwinning effect in this compound.

## 2.2 Superconductivity

Superconductivity (SC) is a macroscopic quantum state. The constituents of this phase are Cooper pairs—paired electrons—which form a spin singlet with vanishing relative orbital momentum. The corresponding order parameter (known as wave function or gap function) may have $s$-wave symmetry, i. e. it is isotropic in momentum space. This pairing symmetry, which is mediated by electron-phonon interactions, is known as conventional superconductivity.

The main property of a superconductor is the Meissner effect—the expulsion of external magnetic fields from its bulk. This feature makes the superconductor a perfect diamagnet with a magnetic susceptibility of $\chi = -1$. Consequently, superconductors exhibit zero electrical resistance, which is their most sought-after feature for technological applications.

The early description of this state—which was first discovered in 1911 in Hg by H. K. Onnes [1]—was of purely phenomenological nature (Ginzburg-Landau theory). Due to their macroscopic character, quantities like the Ginburg-Landau coherence length that describes the length scale over which the SC order parameter can vary, and the London penetration depth, the characteristic depth over which a magnetic field is screened to $1/e$ of its initial value, are still widely used today.

It took almost 50 years until Bardeen, Cooper and Schrieffer (BCS) developed a microscopic theory of conventional SC [2]. The underlying idea of the BCS theory is the formation (*condensation*) of electrons into Cooper pairs. Cooper recognized in 1956 that the ground state of an electron gas is unstable if even the weakest attractive interaction between each pair of electrons is introduced. This interaction is mediated by virtual phonons[1]. The dependence on the lattice vibrations is famously shown by the isotope effect. The Fermi surface instability and the consecutive formation of Cooper pairs lowers the system's energy and a gap develops at the Fermi level, separating the SC ground state from the normal state. The Cooper pairs, which have opposite momentum and spin ($\mathbf{k}^{\uparrow}, -\mathbf{k}^{\downarrow}$), have bosonic character and can, therefore, occupy the same ground state. However, excitations of the SC ground state still have fermionic character, as Cooper pairs are disbanded. As mentioned above, this conventional SC corresponds to an $S = 0$ state in spin space with orbital $s$-wave symmetry.

Consider the following: For negligible spin-orbit coupling the superconducting wave function $\psi_{\mathrm{SC}}$ can be separated into a spin $\chi$ and an orbital component $\phi(\mathbf{r})$: $\psi_{\mathrm{SC}} = \chi\phi(\mathbf{r})$. Although Cooper pairs have bosonic character, the overall wave function must be antisymmetric against the exchange of two electrons (fermions), due to the Pauli exclusion principle. For the spin part we have four ways of combining the two spin-1/2 spins: $|\uparrow\uparrow\rangle$, $|\downarrow\downarrow\rangle$, $|\uparrow\downarrow\rangle$, and $|\downarrow\uparrow\rangle$. This leads to a triplet with even parity:

$$|\chi^{S=1}\rangle = \begin{cases} |\uparrow\uparrow\rangle \\ \frac{1}{\sqrt{2}}(|\uparrow\downarrow\rangle + |\downarrow\uparrow\rangle) \\ |\downarrow\downarrow\rangle \end{cases}$$

and a singlet with odd parity:

$$|\chi^{S=0}\rangle = \frac{1}{\sqrt{2}}(|\uparrow\downarrow\rangle - |\downarrow\uparrow\rangle).$$

The symmetry of the orbital part is determined by the parity of the spherical harmonics $Y_l^m(-\mathbf{r}) = (-1)^l Y_l^m(\mathbf{r})$. That means we could have $p$, $f$, $h$, ... symmetry for a spin singlet state and $s$, $d$, $g$, ... symmetry for a triplet state. In the case of the conventional $s$-wave symmetry, the SC order parameter is isotropic and does not change sign, which

[1] Virtual particles are a concept of quantum field theory (QFT), where they are commonly used to describe, for instance, the gauge bosons of the standard model of particle physics. These so-called off-shell particles do not obey the relativistic energy-momentum relation $E^2 - p^2 = m^2$ ($c = 1$) and thus have no well-defined mass. They are "spontaneous fluctuations of the quantum field", which can not be observed directly. In our case, this means that the phonon is only exchanged between the electrons and can not dissipate into the lattice. An extensive discussion of QFT and virtual particles can be found, e. g., in the book by Peskin and Schroeder [25].

leads to a $k$-independent gap $\Delta$ of constant size within the BCS theory:

$$2\Delta_{T=0} = 3.5 k_{\mathrm{B}} T_{\mathrm{c}}.$$

In contrast, unconventional superconductivity is characterized by an order parameter of lower than $s$-wave symmetry. The first evidence for unconventional pairing was, interestingly, observed not in an electronic system but rather in the super-fluid state of $^3$He. The paired $^3$He atoms form a spin-triplet with angular momentum 1. This type of (p-wave) pairing can not be mediated by electron-phonon interaction, but is, among other factors, likely based on spin fluctuations and van der Waals interactions [26, and references therein]. Only later, unconventional superconductivity was also observed in strongly correlated electron systems, namely, the heavy Fermion compounds, organic- and cuprate superconductors and—most recently— the iron pnictides. However, in the case of the unconventional superconductors the general pairing mechanism—if a single one exists—is so far unknown.

A more detailed discussion of the iron-based unconventional superconductors follows in Chapter 4. Their order parameter in particular is discussed in Section 4.5.

## 2.3 Crystal Twinning

In crystallography and, specifically, in geminography—the branch of crystallography that deals with twinning—crystal twinning refers to an oriented association of two or more individuals (domains) of the same crystalline phase. Those domains are related by a symmetry operation, called twin operation, which does not belong to the symmetry of the underlying crystalline phase. If it did, it would simply produce a parallel growth instead of the twin. In that sense the formation of twins increases the symmetry of the crystal.

Twins can be classified by several criteria, like their formation mechanism, morphology, dimensionality of the "twin lattice", etc. The most common one is the classification from the viewpoint of their genesis. Three categories are distinguished: *growth twins*, *mechanical twins* and *transformation twins*.

Growth twins form during the crystal growth either at the time of nucleation or by oriented attachment of pre-formed crystals [30], while mechanical twins, also called gliding twins, are formed as a result of a mechanical stress—typically oriented pressure. Transformation twins, on the other hand, originate from phase transitions that change the crystal structure. The symmetry elements lost in the transition then act as twin

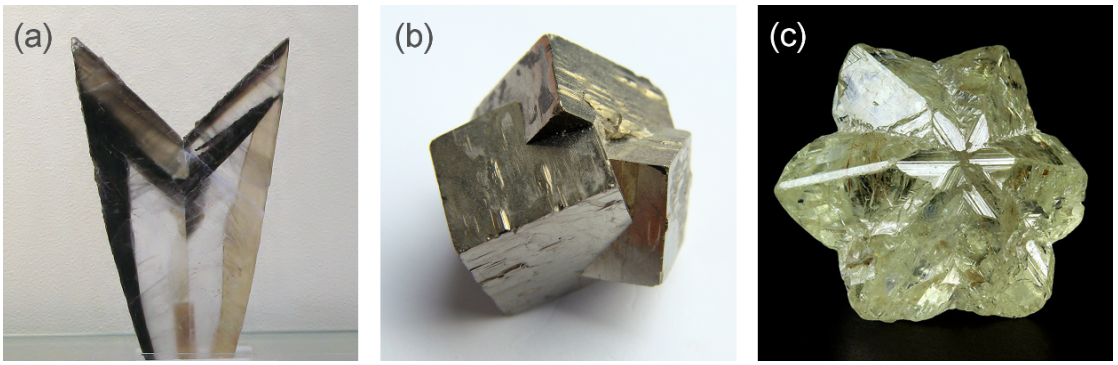


FIGURE 2.6: Photographic images of twinned crystals as they occur in nature: (a) Swallow-tail (contact) twin of Gypsum, (b) penetration twinning of three cubic domains of a pyrite crystal and (c) Chrysoberyl cyclic twin. Pictures adapted from Refs. [27–29]

elements—the geometric elements about which twin operations are preformed. Thus, twins are further categorized as reflection twins, rotation twins and inversion twins. This is related to the morphological classification of twins, which distinguishes *contacts twins*, *penetration twins* and *cyclic twins* to name just a few. The first ones are separated by a surface, while the second share a volume and in the last case, domains are repeated around an axis to form a closed structure in which the N-th domain is in contact with the first (Fig. 2.6). More detailed discussions can be found in the respective textbooks or e. g. in Refs. [31, 32].

The iron-based superconductors (IBSCs) form µm-sized transformation twins upon undergoing a tetragonal to orthorhombic phase transition. For instance, in $BaFe_2As_2$ the structural (and coincident magnetic) transition occurs at $T_{Fe} = 137\,K$. Above $T_{Fe}$, the system is tetragonal (Fig. 2.7a) with in-plane lattice parameter $a_T = b_T$. In the orthorhombic phase below $T_{Fe}$, the lattice distorts along the in-plane diagonals of the tetragonal structure (Fig. 2.7b). This leads to a rotation of the unit cell by roughly 45° and the formation of plate-like twin domains. The faces of these domains, which span the entire crystal, are oriented parallel to the $c$-axis, corresponding to the $(1\,1\,0)_O$ and $(1\,\bar{1}\,0)_O$ planes in the orthorhombic notation [33]. Four twin domain types (O1-O4) form at the transition. The domains of the pairs (O1,O2) and (O3,O4) are mirror images of one another and thus retain $C_4$ symmetry despite the orthorhombic structure ($C_2$). More important for our purposes is that the respective in-plane lattice vectors of the (O1,O3) and (O2,O4) twin domains are collinear. This property will allow us later to treat only two effective domains during the discussion of the detwinning theory in Chapter 6.

Crystal twinning can be problematic for the investigation of materials, because many experiments require samples to have minimum single crystalline dimensions. Neutron diffraction and resistivity measurements, for instance, become typically infeasible for crystals with sub-millimeter twin dimensions. Therefore, the formation of µm-sized

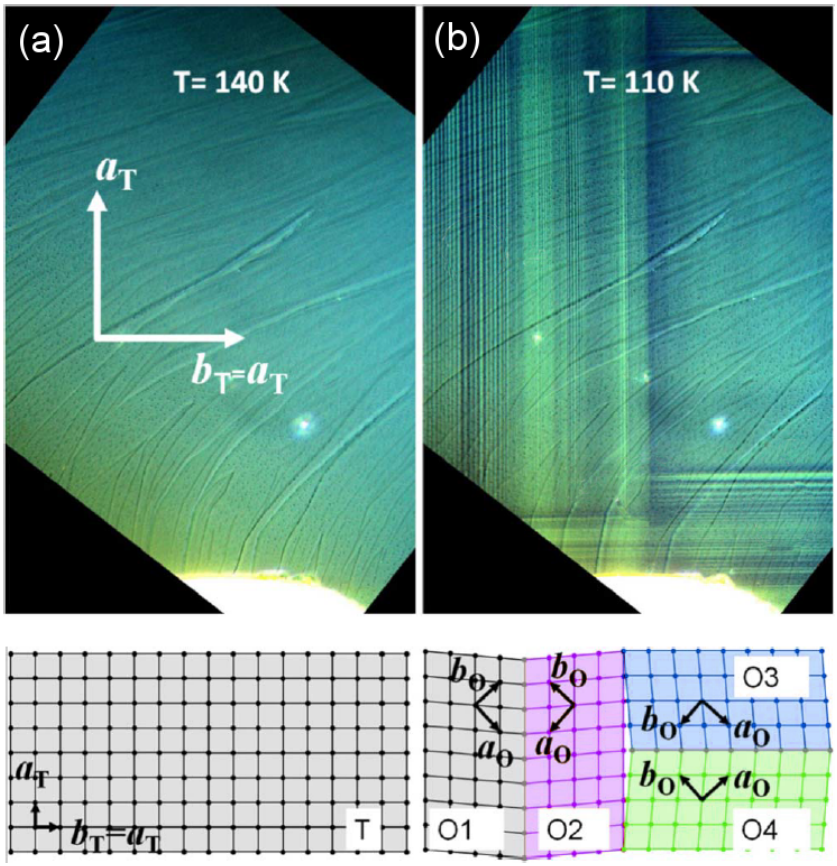


FIGURE 2.7: (Top) Polarized microscopy images of $BaFe_2As_2$ (a) above $T_{Fe}$ in the tetragonal state without twins and (b) below $T_{Fe}$ where $\mu$m-sized twin domains (colored stripes) form in the orthorhombic state. (Bottom) Illustrations of the basal plane structure in the respective phase. The distortion of the crystal lattice along the in-plane diagonals of the tetragonal structure leads to the formation of four twin domain types (O1-O4) below $T_{Fe}$. Note, the respective in-plane lattice vectors of (O1,O3) and (O2,O4) are collinear. Adapted from Ref. [33].

twin domains in the IBSCs below $T_{Fe}$ obstructs the investigation of these materials. However, this problem is not unique to IBSCs. It is also encountered in other systems like the cuprate superconductors, e. g. in $YBa_2Cu_3O_7$ [34, 35].

In order to allow experiments to be performed on large single crystals, theses materials need to be *detwinned*, i. e. transformed into a structurally mono-domain state. This is most commonly achieved by application of uniaxial stress, which favors a certain domain orientation. Typical stresses for the cuprate and iron pnictide superconductors are of the order of 10 MPa [36–38]. The structural phase transition that leads to the formation of twins in the cuprates occurs well above room temperature. Therefore, the crystals can be detwinned by uniaxial force at ambient conditions. However, the structural phase transition in the IBSCs, which leads to twinning, occurs typically below 200 K and thus requires detwinning to take place in a cryogenic environment. The resulting technical challenges complicate the investigation of these materials. A more feasible and less

cumbersome detwinning method is the application on an in-plane magnetic field, which will be presented in detail in Chapter 6.

## 2.4 Log-normal Distribution

Formally, a random variable $X$ is said to be log-normally distributed if $\log(X)$ has a normal distribution. The probability density function (PDF) of such type of variable has the form

$$f_X(x) = \frac{1}{x \cdot \sigma\sqrt{2\pi}} \exp\left[-\frac{(\log(x) - \mu)^2}{2\sigma^2}\right],$$

with the two parameters $\mu$ and $\sigma$ that specify a log-normal distribution. Consequently the cumulative distribution function is given by

$$F_X(x) = \frac{1}{2}\,\mathrm{erfc}\left(-\frac{\log(x) - \mu}{\sigma\sqrt{2}}\right),$$

with $\mathrm{erfc}(x) = 1 - \mathrm{erf}(x)$ the complementary error function, where $\mathrm{erf}(x) = 2/\sqrt{\pi}\int_0^x e^{-t^2}dt$ denotes the error function.

The log-normal distribution is skewed to the left (Fig. 2.8a), while the CDF has a step-like character (Fig. 2.8b). The position of this distribution is determined by $\mu$, while $\sigma$ defines its shape. Only positive values for $x$ are possible.

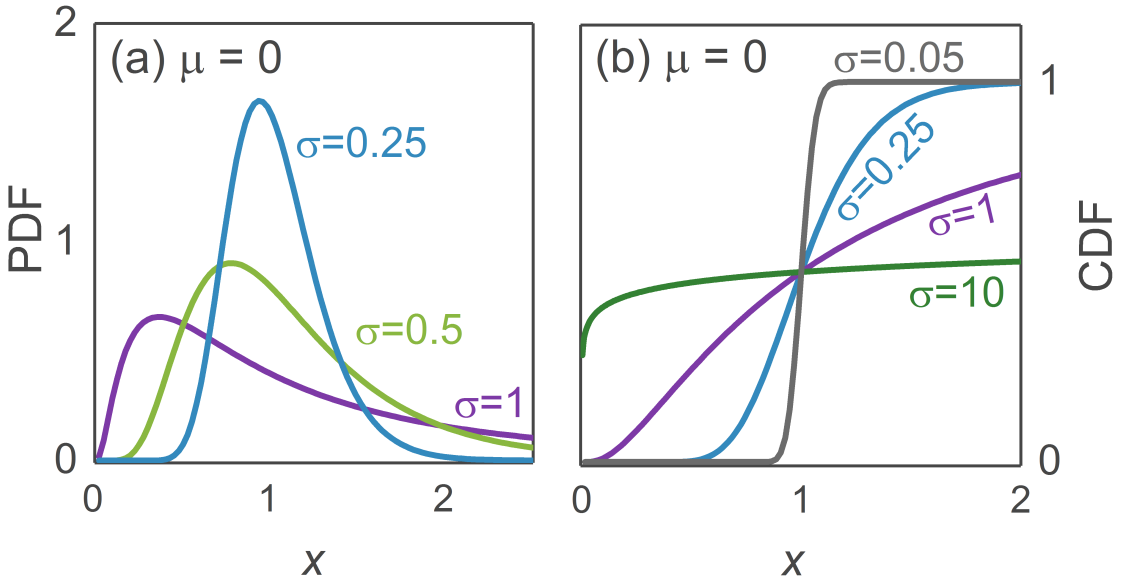


FIGURE 2.8: Generic representations of the (a) probability density function (PDF) and the (b) cumulative distribution function (CDF) for a log-normally distributed variable with $\mu = 0$ and for various $\sigma$.

In nature the different manifestations of both the normal and log-normal distribution arise when various forces act independently of one another on a specific variable. However, while the effects leading to the normal distribution are additive, the ones responsible for the log-normal distribution are multiplicative [39].

We will use the log-normal distribution later in Chapter 6 to model the distribution of the detwinning energy barrier.

Chapter 3

# Experimental Methods

This chapter summarizes the experimental methods used in this thesis. It starts by discussing the lab setup prior to the crystal synthesis, and then moves on to explain the procedures used for the single crystal growth of the Eu-based iron pnictides. This is followed by a presentation of the techniques and methods used for characterizing, processing, and further investigating the obtained samples.

## 3.1 Lab Setup

For the synthesis of single crystals various lab equipment was needed. These were, among other things: an inert glove box for handling volatile and toxic elements, a welding station to seal quartz ampoules with an oxyhydrogen torch, an electric arc melter to seal Ta/Nb crucibles for the high-temperature synthesis, and the furnaces for the actual crystal growth. In the following, the lab setup is exemplified by the setup of the high-temperature furnaces and the new (in-box) electric arc melter.

### High-Temperature Furnaces

The high-temperature synthesis of Eu-based iron pnictide single crystals requires furnaces operating under inert atmosphere, which are capable of reaching temperatures up to approximately 1500 °C. Therefore, two vertical heating units[1] with a $T_{\mathrm{max}} = 1800\,^{\circ}\mathrm{C}$ were acquired. The units were modified to meet the above criteria. The final furnace assemblies (Fig. 3.1) consist of the commercial heating units, a sealed growth chamber made out of a half-open alumina ($Al_2O_3$) tube which is permanently bonded to a custom made, water-cooled metal flange that connects to the vacuum pump and an Ar-gas

[1] GERO Hochtemperaturöfen GmbH & Co. KG, Model: HTRV 70-250/18


FIGURE 3.1: (Left) High-temperature furnace assembly with (a) commercial heating unit, (b) power supply unit, (c) vacuum tubing, and (d) sealed growth chamber. (Right) Sealed furnace chamber during growth at 1500 °C with (e) water cooled (f) metal flange covered by (g) a radiation shield made of Al foil to protect the adhesive bond between the flange and the $Al_2O_3$.

line for purging of the growth chamber. The metal-ceramic connection is crucial for the entire hermetic operation of the furnaces, the developed installation process will, therefore, be briefly presented in the following.

The metal flange and the ceramic alumina tube were bonded with an off-the-shelf, two-component epoxy. However, prior to the glue-up, the corresponding faces were first sand blasted to increase the surface area and then treated by flame-pyrolytic surface silicatization. Through this technique a 20 nm to 50 nm thin, but very dense, film of silicon dioxide is deposited on the two contact faces. This film adheres strongly to metals, glasses, ceramics, and polymeric materials and increases the surface energy of the involved parts significantly. The high surface energies, in turn, increase the wetting on the surfaces and, therefore, improve the adhesion to the epoxy. I found that this preparation leads to a long-term and hermetic adhesive bond.

Although I collected no quantitative data, the sealing of the furnaces turned out to be excellent and long lasting. Judging by the lack of substantial oxidation on the Zr-foil—which is used as an oxygen getter during growth—the leak rate is now distinctly better

then in the setups that were previously used in our labs at the University of Göttingen. In fact, the sealing is so stable that the furnaces are now generally operated under static atmosphere, instead of the previously used (99.999 % pure) Ar-flow, which turned out to actually transport more oxygen into the furnace than in the static operating mode. In this mode, the Nb and Ta crucibles can withstand temperatures of about 1500 °C for roughly a week without showing significant signs of oxidation.

Recently, I retrofitted one of the furnaces with a custom-made thermocouple, which is connected to the bottom of the sample batch. This should in principle allow for the tracking of phase transitions during the growth, which will facilitate the optimization of the growth profiles.

**Electric Arc Melter**

An electric arc melter is ideal to seal Nb or Ta crucibles under protective Ar atmosphere for the growth process. Initially only a large, commercial arc melter outside the Ar-filled glove box was available for sealing. However, this meant exposing the samples to air while transferring them from the glove box to the device.

In order to avoid this step, I initiated the design and construction of a new arc melter which is operated inside the existing glove box (Fig. 3.2). The power supply unit provides a maximal current of $I_{\mathrm{max}} = 80\,\mathrm{A}$ at voltages of $U_{\mathrm{weld}}$ =10–18 V for welding. The power output can be conveniently regulated by a foot pedal from outside the glove box. A massive ($M_{\mathrm{Cu}}$ =14.7 kg) Cu disc acts as a solid base for the arc melter, providing a significant thermal mass with excellent thermal conductivity. This allows for a rapid and efficient heat dissipation away from the sample, which is particularly important when highly toxic or volatile elements, such as As or K, need to be sealed. In addition, it makes a water-based cooling circuit obsolete, which removes the risk of contaminating the glove box with water. For an even more efficient heat transport and in order to seal more than one batch at a time, I further designed a new batch holder, which can now accommodate four, instead of one crucibles at a time.

## 3.2 Single Crystal Growth

An important goal of this thesis was the synthesis of high-quality single crystals of the parent compound $EuFe_2As_2$ and its magnetically diluted variants $Eu(Fe_{1-x}Ru_x)_2As_2$ and $Eu_{1-x}Ba_xFe_2As_2$ for the investigation of the magnetic detwinning effect. Since directional-dependent measurements are necessary, easy to prepare polycrystalline samples were not an option.


FIGURE 3.2: New in-box arc melter, with (a) copper base, (b) glass recipient, (c) vacuum tubing, and (d) thermocouple to monitor the temperature of the Cu block during welding. The electrode (e) can be moved freely within the entire glass recipient and, in particular, allows for sealing crucibles of varying height. The inset shows a magnification of the improved sample holder, which can now accommodate four samples (three shown) and features a depression for the oxygen getter—a piece of Zr.

### 3.2.1 Sequence of Operations

$EuFe_2As_2$ and $Eu(Fe_{1-x}Ru_x)_2As_2$ were grown using a modified Bridgman method, while the $Eu_{1-x}Ba_xFe_2As_2$ system was synthesized employing the common FeAs self-flux method. For the former two an ultra low (5 % excess) self-flux method, which basically relies on a congruent melt, was used. The Ba-doped samples were synthesized with a flux to sample ratio of 2:1 or 4:1.

Elemental Eu is very volatile and needs to be stored and handled under protective atmosphere, while arsenic and especially its oxides are highly toxic. Therefore, during all the steps the materials were kept under inert argon atmosphere. Highly purified elemental Ba (99.3 %), Eu (99.9 %) and phase-pure precursors of FeAs and RuAs were used for the synthesis.

**0 - Precursor Preparation**

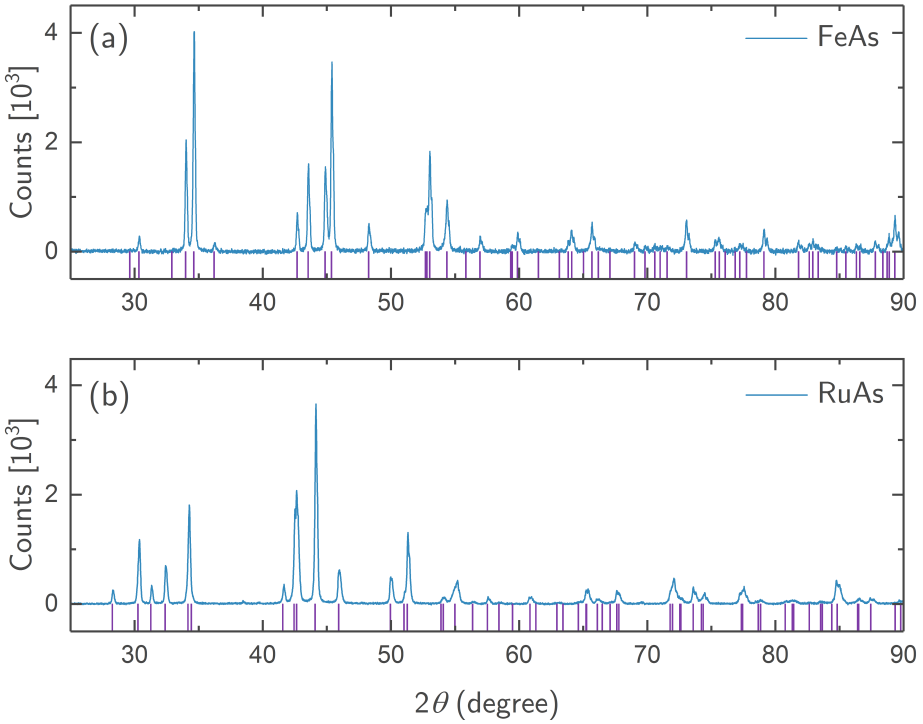


FIGURE 3.3: Representative x-ray powder diffraction patterns of phase-pure (a) FeAs and (b) RuAs precursors. Markers (violet) indicate indexed peak positions of the orthorhombic crystal structure (space group: *Pnma*) [41].

In order to reduce the high vapor pressure of elemental arsenic ($\sim$1 bar at 600 °C [40]), precursors of FeAs and RuAs were prepared using solid-state reaction. Fine powders of highly purified elemental Fe (99.998 %), As (99.999 %), and Ru (99.98 %) were mixed in a ratio of 1:1. The mixtures were placed in $Al_2O_3$ crucibles covered with lids and finally sealed under 600 mbar Ar pressure in a Nb crucible using electric arc melting. This setup is very similar to the one used for the single crystal growth (see Fig. 3.4), only larger crucibles were used here. These crucibles were then placed into one of the high-temperature furnaces (Fig. 3.1), which are also sealed under Ar atmosphere. Zr-foil can be added as oxygen-getter material to further protect the metal crucible from oxidization.

Temperature profiles for the precursor synthesis are given in Tab. 3.1. The dwell time at $T_1$ is to allow for some pre-reaction of the Fe and As ($T^{\mathrm{As}}_{\mathrm{sublim.}} = 613\,°\mathrm{C}$). After the last dwell time the batches were cooled to room temperature by switching off the furnace. Note that for a weighted portion of more than 10 g the hold durations were doubled to ensure proper reaction of the elements. Finally, the precursor lumps were ground into fine powders using a mortar and acetone, before storing them in the argon glove box.

The quality of the precursors was determined by x-ray powder diffraction. The XRD

TABLE 3.1: Temperature profiles for precursor synthesis. $T_n$, $R_n$ and $t_n$ denote set point, heating rate, and dwell time at $T_n$, respectively.

| Precursor | $T_1$ [°C] | $R_1$ [°C h$^{-1}$] | $t_1$ [h] | $T_2$ [°C] | $R_2$ [°C h$^{-1}$] | $t_2$ [h] |
|---|---|---|---|---|---|---|
| FeAs | 600 | 100 | 10 | 700 | 80 | 20 |
| RuAs | 550 | 100 | 10 | 900 | 80 | 20 |

patterns (Fig. 3.3) indicate phase-pure compounds, as all peaks could be indexed with the orthorhombic $AlB_2$ structure (space group: *Pnma*). A comparison of the lattice parameters can be found in Tab. 3.2. With an average relative difference on the order of $10^{-3}$, they agree very well with literature data.

TABLE 3.2: Refined and published precursor lattice parameters.

| | Lattice Parameter | | |
|---|---|---|---|
| Compound | $a$ | $b$ | $c$ |
| FeAs | 5.444(5) | 3.367(2) | 6.019(4) |
| Ref. [41] | 5.43927(4) | 3.37252(2) | 6.02573(4) |
| RuAs | 5.717(3) | 3.322(3) | 6.316(4) |
| Ref. [41] | 5.71685(8) | 3.33790(5) | 6.31294(9) |

**I - Packaging**

The starting materials for the crystal growth were mixed and placed in alumina crucibles. The Eu and Ba lumps were cut into small pieces with a strong wire cutter to increase the surface area for the reaction. The alumina crucibles for the ultra low flux growth were covered with lids and placed in Nb crucibles, which were then sealed under Ar atmosphere using the electric arc melter inside the glove box. The alumina crucibles for the FeAs-flux growth were covered with a strainer and a catch crucible for later spinning in a centrifuge. This assembly was then placed into a quartz tube that had been cushioned with quartz wool. The quartz tube was pumped to $10^{-3}$ mbar and then purged with Ar gas several times before it was sealed with an oxyhydrogen gas torch.

**II - Growth**

The sealed Nb crucibles were placed, with some Zr-foil as oxygen getter, in a high-temperature furnace (Fig. 3.1). The batches were heated with a ramp of 120 °C h$^{-1}$ to $T_{start}$ (Tab. 3.3), where they stayed for 10 h to ensure proper mixing of the materials. The growth occurred while ramping the temperature with 3 °C h$^{-1}$ down to $T_{stop}$, followed by a subsequent cooling to room temperature by switching off the furnace. The values for $T_{start}$ and $T_{stop}$ needed to be increased with increasing Ru-content in order

to ensure proper synthesis, likely, because the melting point of the Ru-doped series increases significantly with Ru-content. Following these profiles, the single crystal growth takes 3 to 6 days.

TABLE 3.3: Growth temperatures for $EuFe_2As_2$ and $Eu(Fe_{1-x}Ru_x)_2As_2$ single crystals.

| Ru [%] | 0 | 7.5 | 15 | 20 | 22.5 | 25 | 30 | 35 | 40 | 45 |
|---|---|---|---|---|---|---|---|---|---|---|
| $T_{start}$ [°C] | 1375 | 1325 | 1400 | 1400 | 1400 | 1400 | 1400 | 1450 | 1450 | 1450 |
| $T_{stop}$ [°C] | 1050 | 1050 | 1325 | 1325 | 1325 | 1325 | 1325 | 1350 | 1350 | 1350 |

The sealed quartz tubes of the Ba-doped batches were put into a box furnace[2] and heated at a rate of 100 °C $h^{-1}$ to 1125 °C with a dwell time of 5 h. The growth was realized by a ramp of 1.5 °C $h^{-1}$ down to 1050 °C, at which temperature the batches were extracted from the furnace and centrifuged to remove the liquid flux.

**III - Extraction**

The hot quartz tubes of the Ba-doped series were placed upside down in a centrifuge and spun at a rate of approximately 750 rpm for a few seconds. This ensures proper separation of the liquid flux from the crystals. The right-hand side of Fig. 3.4 shows the quartz-tube assembly with the growth and catch crucible directly after spinning. The red glowing flux is visible at the bottom of the catch crucible.

The extraction process, up to the point where the centrifuge reaches full speed, must be kept as short as possible in order to avoid solidification of the flux. In our case, it should take less than 5 s to remove the batch from the furnace and start the centrifuge. Therefore, it is highly recommended to practice this procedure several times beforehand with a dummy-batch, including all the necessary protective gear, like gloves, welding goggles, heat shield, etc.

The cold Nb crucibles of the Ru-doped series were opened under a fume hood using a pipe cutter, and the crystals were extracted from the alumina crucible by breaking it with a wire cutter.

A batch of $Eu(Fe_{1-x}Ru_x)_2As_2$ after synthesis is shown in Figure 3.5(a-b). The largest single crystal of this batch (Fig. 3.5c-d) has dimensions of approximately 8 mm × 3 mm × 3 mm and weighs more than 900 mg. Compared to the self-flux method used for Eu-based iron pnictides [42, 43], these values are extraordinarily high.

The single crystals of the synthesized systems are not very air sensitive, in the short to medium term. However, an inert atmosphere for longtime storage is advised, as e. g.

[2] Nabertherm GmbH, Model: L9/13/P330


FIGURE 3.4: (Left) Niobium and alumina crucibles with caps for high-temperature synthesis of the $Eu(Fe_{1-x}Ru_x)_2As_2$ series. (Right) Quartz-tube assembly directly after separating the liquid flux from the $Eu_{1-x}Ba_xFe_2As_2$ crystals into the catch crucible (bottom) through a strainer (middle) from the growth crucible (top) via centrifuging at around 750 rpm for a few seconds. The glowing flux is still visible at the bottom.

$EuFe_2As_2$ crystals that had been exposed to air for several years tended to develop dull surfaces.

**IV - Etching (optional)**

The spinning process used during the synthesis of the $Eu_{1-x}Ba_xFe_2As_2$ system might not remove all the flux. However, the FeAs flux is readily dissolved in hydrochloric acid, while the crystals are much less affected. Therefore, they were further cleaned, if necessary, by exposing them to a diluted HCl solution for several minutes. A solution of roughly 18 % concentration was found to sufficiently remove the flux. However, higher concentrations up to 37 % were used as well, reducing the time of exposure, but affecting the crystals more severely.

The Ru-doped series should not be exposed to HCl, however. The acid reacts strongly with the crystals leaving them brittle with dull surfaces after a few minutes. The reactivity increases with increasing Ru-content.

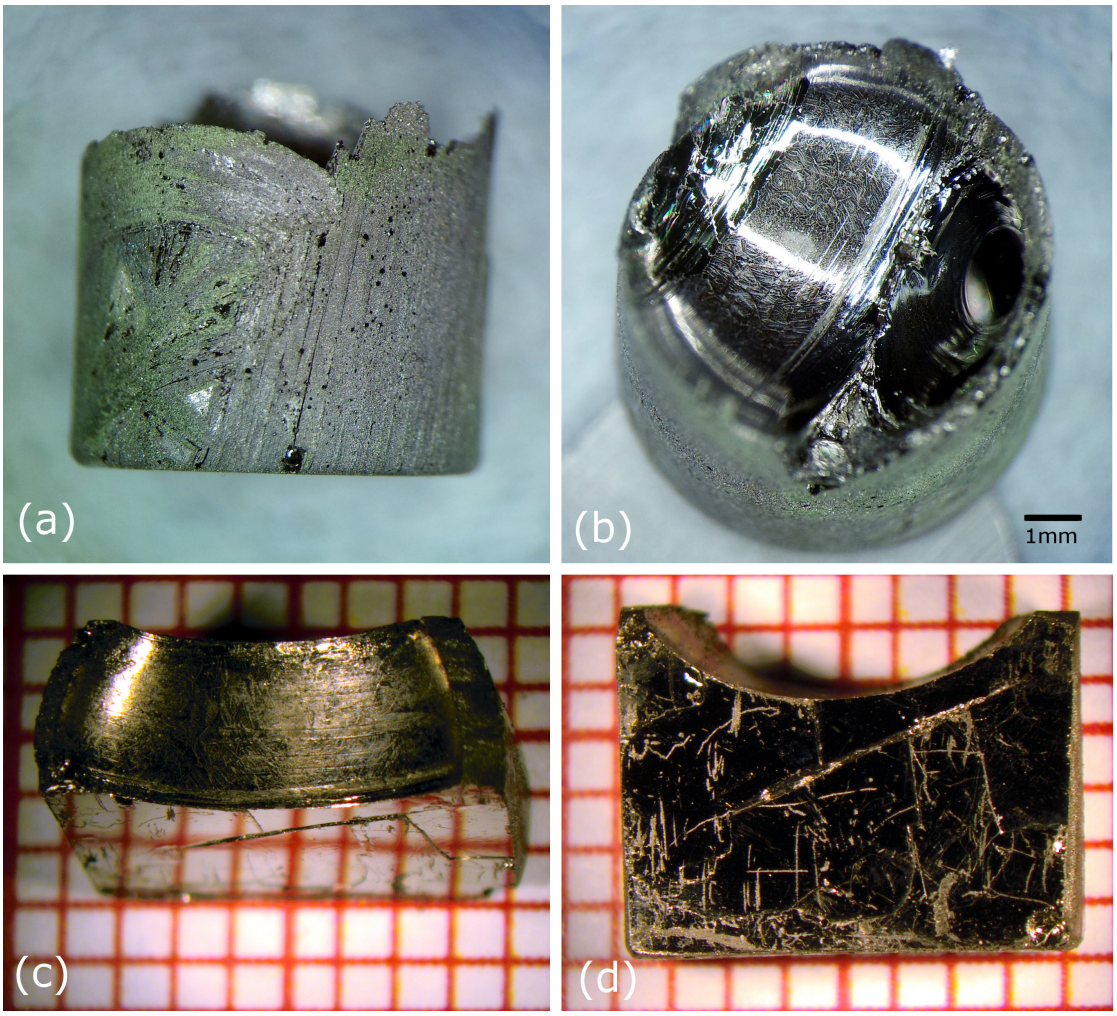


FIGURE 3.5: Photographic images of synthesis results for $Eu(Fe_{1-x}Ru_x)_2As_2$. (a) Side view and (b) top view of a batch of Ru-doped crystals after synthesis. The large single crystal in the bottom section was extracted from this batch. (c) The top view coincides with the crystallographic *ac*-plane, while (d) the side view coincides with the basal plane of the tetragonal crystal structure. The curved shape at the top is due to adhesive forces that pull the liquid melt up the crucible walls during growth.

## 3.3 Structural & Chemical Characterization

Prior to thermodynamic, transport or dilatometric measurements, the samples were structurally and chemically investigated. Lattice parameters and phase-purity were determined with x-ray powder diffraction (XRD). The chemical composition was determined by either energy-dispersive x-ray spectroscopy (EDX) or from Vegard's Law (see Chp. 5). The Laue backscattering technique was used to determine the orientation of the crystals and to estimate their structural quality. The surface roughness of one sample was further investigated with atomic force microscopy (see Appendix A). All doping concentrations stated throughout this thesis refer to the nominal composition, unless specifically stated otherwise.

### X-ray Powder Diffraction

A Rigaku Miniflex 600 x-ray powder diffractometer was used to determine the crystal structure and lattice parameters of the samples. For the measurements, a few mg of the respective samples were cut off and ground into a very fine powder using a mortar and acetone. The powder was then placed onto a "zero background" holder (an oriented silicon plate producing no reflections in the typical scanning range) and slightly compressed with a spatula-like scoop. A small drop of acetone consolidates the powder on the sample holder, ensuring that the powder sticks to the holder and does not come off during high-angle measurements. Details of the device, parameters and software used for the analysis can be found in Tab. 3.4.

Table 3.4: Detailed Information on Data Acquisition: XRD.

| Device | Parameter | Software |
|---|---|---|
| Diffractometer: | Voltage: 40 kV | Rigaku |
| Rigaku | Current: 15 mA | MiniFlex Guidance |
| MiniFlex 600 | $\lambda$: 1.5406 Å (Cu-$K_\alpha$) | (Version 1.4.0.3) |
| | Mode: Theta/2 Theta | PDXL2 |
| | Speed: 5 ° $min^{-1}$ | (Version 2.3.1.0) |
| | Stepsize: 0.01 °/step | DB: PDF-4+ 2014 |

### X-ray Spectroscopy

The chemical characterization, in particular, the determination of the doping content of the $Eu(Fe_{1-x}Ru_x)_2As_2$ and $Eu_{1-x}Ba_xFe_2As_2$ series, was performed at the University of Göttingen using a scanning electron microscope (SEM) equipped with an energy-dispersive x-ray detector (EDX) for the spectroscopic analysis. More detailed information regarding setup, parameters and software are collected in Tab. 3.5.

Table 3.5: Detailed Information of Data Acquisition: EDX.

| Devices | Parameter | Software |
|---|---|---|
| SEM: | Voltage: 20 kV | Noran Systems |
| Zeiss | Aperture: 60 mm | S/X v.1.8 |
| Leo SUPRA 35 | | |
| EDX Detectors: | Dead Time: | Thermo Scientific |
| SE2 & Inlense | 33-35 % | NSS v.3.1 |

### Laue Backscattering Technique

The Laue backscattering technique was mainly used to orient the samples before cutting them into a rectangular shape with their edges parallel to the $[1\,1\,0]_T$ directions. However, it is also an appropriate method to asses the crystallinity of the samples. Furthermore, it is a means of gauging the overall structural quality of the crystals.

The samples were exclusively oriented along the $[1\,1\,0]_T$ equivalent direction with the exception of one $EuFe_2As_2$ reference sample which was cut along $[1\,0\,0]_T$ direction. The $[1\,1\,0]_T$ direction can easily be distinguished from the $[1\,0\,0]_T$ direction by considering the $[2\,1\,0]_T$ direction, which is at an angle of 18.4° with the former and an angle of 26.6° with the latter. It, therefore, appears like a cone around the $[1\,1\,0]_T$ direction, making it easy to identify, see also Chapter 5 (Fig. 5.9). More detailed Information on the Laue data acquisition are given in Tab. 3.6.

Table 3.6: Detailed Information on Data Acquisition: Laue.

| Device | Parameter | Software |
|---|---|---|
| Generator:<br>Philips PW 1830 | Voltage: 15 kV<br>Current: 30 mA | n/a |
| Digital Laue Camera:<br>Photonic Science<br>Dual FDI NTX | Exposure: 300 s<br>Distance: 19 mm<br>(Sample-Screen) | PSL Viewer<br>3I-CFG |

## 3.4 Sample Preparation & Measurement Setups

In this section, the sample preparation processes used for the various measurements are discussed and the measurement setups and their parameters briefly stated.

### 3.4.1 Orientation & Cutting

For the physical investigation the crystals need to be oriented and cut along the $[1\,1\,0]_T$ tetragonal direction, which corresponds to the $[1\,0\,0]_O$ orthorhombic direction. The orientation was done with a standard Laue camera as discussed in Sec. 3.3. The samples were then cut into a rectangular shape using electrical discharge machining.

### 3.4.2 Electrical Transport

Transport measurements were performed with two standard Quantum Design *Physical Property Measurements Systems* (PPMS) equipped with 14 T and 9 T magnets, respectively, using the Electrical Transport Option and the Horizontal Rotator Option.

The samples were contacted using Cu & Au leads with a diameter between 50 µm to 100 µm. They were attached with silver paste after roughening the sample surface with abrasive paper (P1000 grid) for a better connection. Depending on the signal-to-noise ratio, the drive currents varied between 1 to 10 mA, while the AC frequency was fixed to 117 Hz.

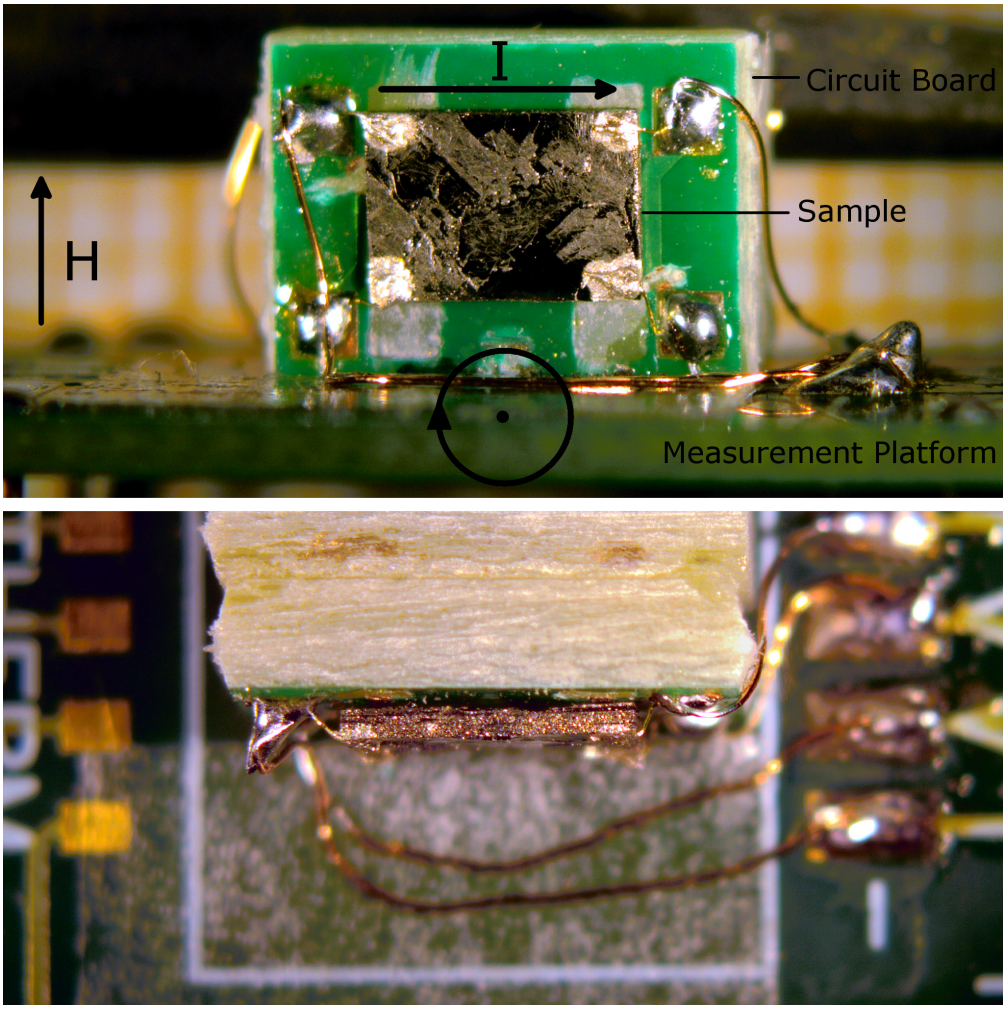


FIGURE 3.6: Electrical transport setup of a cut and contacted single crystal. (Top) The sample is mounted in Van der Pauw geometry on a circuit board, which in turn is glued perpendicular to the plane of the measurement platform. The edges of the crystal correspond to the $\langle 1\,1\,0\rangle_T$ directions. (Bottom) The sample is hovering parallel over the circuit board, leaving it free to expand in any direction. Arrows indicate field $H$ and current $I$ direction, as well as, the axis around which the measurement platform can be rotated.

The samples were mounted on a circuit board with 50 µm Au wires. The circuit board was, in turn, fixed on the measurement platform perpendicular to its surface. In order to minimize stresses exerted on the sample during measurements, the Van der Pauw (VdP) geometry was used for contacting. The samples were mounted such that they were hovering parallel to the circuit board attached to it only through the contact leads (Fig. 3.6). The edges of the crystals were aligned parallel to the edges of the circuit board. Soldered Cu wires (100 µm) connected the circuit board to the platform.

### 3.4.3 Capacitive Dilatometry

A capacitive dilatometer, developed by R. Küchler at the Max-Planck Institute for Chemical Physics of Solids in Dresden, in conjunction with a 9 T-PPMS for temperature and field control was used to determine the length change of the samples as a function of applied magnetic field and temperature. The capacity was measured with an AH-2500A Andeen-Hagerling bridge, with a maximum precision of $1 \cdot 10^{-7}$pF. In order to reduce noise, the device averages over 64 measurement points internally, before relaying the data to the computer. Length changes of the order of 0.1 Å can be resolved.

An operating range between 10 and 35 pF was used on the dilatometer. This corresponds to a spring force between 1.5 and 3 N that is exerted on the sample during measurements. The magnetic field can only be applied along the measurement direction due to technical limitations.

### 3.4.4 Magnetization

Magnetization data was acquired using a standard *Magnetic Property Measurement System* (MPMS) in DC mode. Specific information on the device can be found in Ref. [44].

### 3.4.5 Neutron Diffraction

High-resolution neutron scattering experiments were conducted on the cold-neutron triple-axis spectrometer IN12 at the high-flux reactor of the Institute Laue-Langevin (ILL) in Grenoble, France in cooperation with S. Nandi from the Universitiy of Kanpur, India and Y. Xiao from the Forschungszentrum Jülich in Germany. Neutrons with wave vectors of $k_f = 2.5\,\text{Å}^{-1}$ and $2.85\,\text{Å}^{-1}$ were used during the experiment, which corresponds to a neutron wavelength of 2.513 Å and 2.205 Å, respectively.

The crystals were mounted on a vanadium pin and covered with a Cd foil to increase the signal-to-noise ratio. The assembly was then mounted inside an ILL Orange cryostat

equipped with a 9 T magnet. Measurements were confined to the $(H\,0\,L)_{\mathrm{O}}$ scattering plane (in orthorhombic notation) and conducted between 2-300 K. The magnetic field was applied perpendicular to the scattering plane.

### 3.4.6 Thermopower

The thermopower was measured using a standard 9 T PPMS equipped with the *Thermal Transport Option* (TTO). The samples were contacted in the van der Pauw geometry, with 50 $\mu$m Au wires and silver paste. The sample was mounted on a circuit board as described in Sec. 3.4.2. Additional Cu leads (100 $\mu$m) were soldered to the circuit board to connect the sample via the board to the contact shoes of the TTO puck. Great care had to be taken to properly orient the sample on the holder and with respect to the magnetic field, which was applied in-plane along the $\langle 1\,1\,0\rangle_{\mathrm{T}}$ directions.

The measurements were then performed in the *Continuous Measurement Mode* with a temperature ramp between 0.05 and 0.2 K min$^{-1}$. The parameters "Temperature Rise" and "Period Ratio" were fixed to about 3 % and 20, respectively, in order to ensure the proper convergence of the internal fit algorithm of the TTO. Further information regarding the measurement technique can be found in Refs. [45, 46].

Chapter 4

# Iron-Based Superconductors

This chapter reviews some of the iron-based superconductors (IBSCs). Its purpose is to delineate the research field to which this thesis belongs in order to help the reader better understand the scope of this work. In this regard, it will serve as a solid background for the discussion of the Eu-based iron pnictides and our observation of a multistage magnetic detwinning effect in $EuFe_2As_2$. The chapter begins with a brief introduction with remarks on the discovery of the IBSCs, followed by a discussion of their crystal structures and phase diagrams. Subsequently, the electronic structure with a particular emphasis on the nematic phase is examined. Subsequently, I will introduce the reader to the ongoing debate on the nature of the superconducting order parameter in these systems and to the most common methods to synthesize this class of materials. The final section of this chapter focuses on the Eu-based iron pnictides.

The IBSCs receive a huge amount of sustained attention in the scientific community, since their discovery in 2008. As of 2015, more than 15,000 papers have been published on these materials [47]. Therefore, a vast body of original papers, review articles, and lately, also more and more textbooks are available for further information. While this review conceptually follows the discourse found in Refs. [48–50], other, more detailed reviews can be found e. g. in Refs. [47, 51–56].

## 4.1 Introduction

The iron-based superconductors are the most recently discovered class of unconventional superconductors and, therefore, follow the preceding discoveries of superconductivity in heavy-fermion systems, 1D organic compounds, and the layered $CuO_2$-based cuprates. The latter feature the highest critical temperatures ($T_c$), commonly exceeding the boiling

point of liquefied nitrogen (77 K) at ambient pressure, which makes them the most promising candidates for practical applications.

The IBSCs were discovered in 2006 when the group of Hideo Hosono found superconductivity (SC) in LaOFeP with a $T_c$ of about 4 K [6]. However, worldwide attention from the physics community was only attained in 2008 when the same group reported SC in fluorine-doped LaFeAsO with a $T_c = 26$ K [7]. The discovery of SC in materials containing magnetic elements, like Fe was a surprise, as even tiny amounts of magnetic impurities usually suppress SC. In fact, The discovery was (at least partially) coincidental, since Hosono *et al.* originally worked on transparent p-type semiconductors LaCuO*Ch*, with *Ch*= S and Se. The mobile holes in the valence band of these materials are responsible for the p-type conduction. The valence band consists of *Ch* $p$ orbitals and Cu $3d$ orbitals [57]. In order to investigate magnetic semiconductors, they wanted to make use of strong $d$-$p$ interactions by introducing magnetic $3d$ transition metal cations, like $Fe^{2+}$, to the nonmagnetic $Cu^{+}$ site. However, as charge-neutrality needed to be kept, they further replaced the $Ch^{2-}$ with pnictogen anions with a charge state of 3-, like $P^{3-}$ [58]. This led to the investigation of the electronic and magnetic properties of La*TM*O*Pn* (with *TM*= $3d$ transition metal and *Pn* = P, As) and, consequently, to the discovery of the IBSCs.

These materials feature the second highest $T_c$ of the unconventional superconductors, reaching up to 58 K in Sm-based compounds, like $SmFeAsO_{0.74}F_{0.26}$ [59], $SmFeAsO_{0.85}$ [60], and $SmFeAsO_{0.8}H_{0.2}$ [61]. Very recently, an even higher $T_c$ was reported in a mono-layer of FeSe grown on doped $SrTiO_3$ [62].

## 4.2 Structure and Phase Diagram

The IBSCs are typically categorized into iron pnictides and iron chalcogenides, which are further divided into three classes for the iron pnictides, namely, the 1111-, 111-, and 122-family, while the iron chalcogenides form a unique class called the 11-family[1]. The names are derived from their stoichiometric composition, i. e. LaFeAsO is of type 1111, while $BaFe_2As_2$ belongs to the 122-family and so forth. Most research was performed on the 122-family ($MFe_2As_2$, with $M$ = Ca, Sr, Ba and Eu) of the IBSCs, largely due to the availability of large single crystals of relatively good quality. However, lately attention seems to shift towards the more correlated 11-type materials.

[1] There are also other systems with perovskite-type blocking layers and skutterudite intermediary layers, which will not be discussed here. Detailed information on these systems can be found e. g. in Ref. [48].

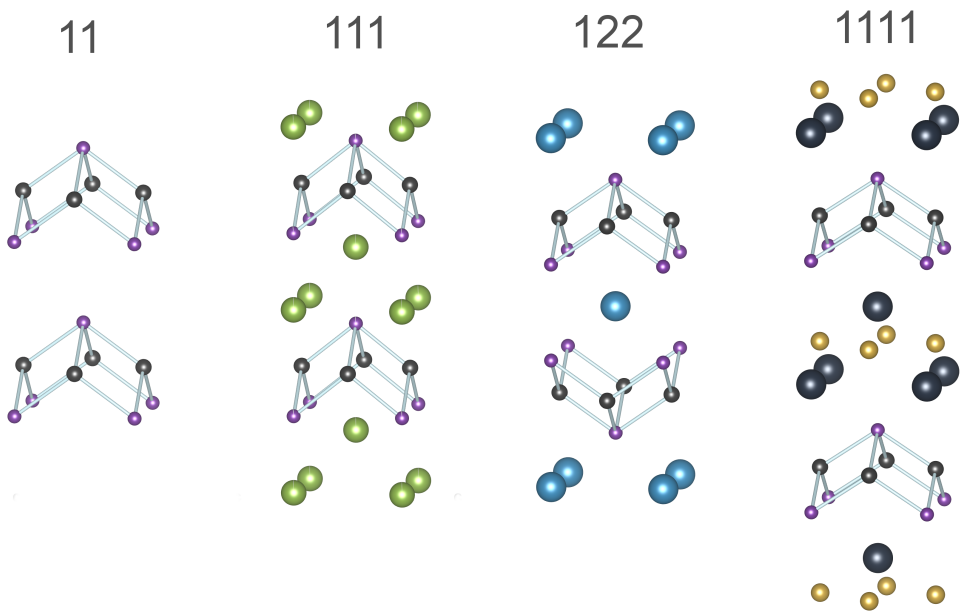


FIGURE 4.1: Tetragonal structures of the four IBSCs (e. g. FeSe, LiFeAs, $BaFe_2As_2$, LaFeAsO) introduced in the main text. All share an iron (gray) square layer in which the iron is tetrahedrally surrounded by chalcogen or pnictogen anions (violet). The iron pnictides (111, 122, 1111) feature spacer layers between the iron-pnictogen layers, which usually consist of either an alkaline earth or a rare earth element and oxygen/fluorine (Li-green, Ba-blue, La-black, O-yellow).

Like the cuprates, the IBSCs are layered compounds. The iron sits on a square lattice and is tetrahedrally surrounded by either pnictogen or chalcogen anions (Fig. 4.1). In the case of the iron pnictides, these layers are separated by spacer layers, which typically consist of either an alkaline-earth or rare-earth element and oxygen/fluorine. At ambient conditions, theses materials are in a paramagnetic, metallic state with a tetragonal crystal structure, where the different layers are alternatingly stacked along the $c$-axis.

In LiFeAs, the prototypical 111 system, the FeAs layers are interleaved by double Li planes to form the anti-PbFCl-type structure (space group: $P4/nmm$) with two formula units per unit cell. The FeAs tetrahedra are distorted, with two distinct As-Fe-As bonds ($\alpha$, $\beta$). While LiFeAs does not change its crystal structure upon cooling, the sister compound NaFeAs changes to orthorhombic lattice symmetry with space group $Cmma$ around 50 K.

The 1111 systems have the ZrCuSiAs-type structure ($P4/nmm$). Upon cooling they also change to an orthorhombic structure ($Fmmm$), which for LaFeAsO sets in below 155 K.

$BaFe_2As_2$ is the prototype of the 122 systems and perhaps the most studied of all the IBSCs. As the other 122's, it adapts the $ThCr_2Si_2$-type structure. Similar to the 111's, they feature edge-sharing tetrahedra. However, the adjacent FeAs layers are only

separated by a single layer of Ba ($M$) atoms. The body-centered tetragonal structure has space group $I4/mmm$ and undergoes a structural transition to an orthorhombic structure with space group $Fmmm$ below 140 K.

The structural transition in the iron pnictides is accompanied by an antiferromagnetic (AF) transition of the electronic system. The Fe moments order in a columnar, spin density wave (SDW) type structure with AF order along the crystallographic $a$-axis and $c$-axis and ferromagnetic (FM) order along the $b$-axis. The iron chalcogenides can also feature diagonal stripe order, instead of this collinear arrangement. The term SDW is used here to emphasize the more itinerant character of the Fe $3d$ moments, compared to the localized Cu $3d$ electrons of the cuprates.

However, the IBSCs exhibit itinerant as well as localized character of the electronic system and are, therefore, located somewhere between the two extremes (see also Chap. 2.1.2). According to Ref. [50], the itinerant character of antiferromagnetism in the iron pnictides is, among other things, indicated by:

- Moderate electronic correlations, which are unlikely to cause strong localization.
- Good nesting between electron- and hole-like sheets of the Fermi surface in most compounds, which favors the formation of an SDW state.
- Relatively small ordered moments $\mu_{\mathrm{sat}}$ of typically 0.3 to 1 $\mu_{\mathrm{B}}$, considering the six electrons in the Fe-3d orbitals ($Fe^{2+}$: [Ar] $4s^0$ $3d^6$).

While evidence for a more local character includes:

- A magnetic moment in the disordered state, comparable to the ordered state value, which is uncommon for itinerant systems.
- Some materials exhibit a considerable bandwidth renormalization, compared to LDA calculations, which indicates strong correlations. In LiFeAs, for instance, the renormalization is $\sim 3$ [54, 63].

These points illustrate the dual character of the magnetism in the IBSCs.

Superconductivity can be induced by the application of external pressure or chemical substitution. In the case of chemical substitution one distinguishes between electron doping, hole doping, and isovalent doping, which is also called chemical pressure. In the 122 materials, all three lattice sites can be doped to induce SC (Fig. 4.2). By increasing the tuning parameter $x$ (pressure, doping), the electronic and structural transitions temperatures decrease continuously. Eventually, SC sets in with $T_{\mathrm{c}}$'s between a few K

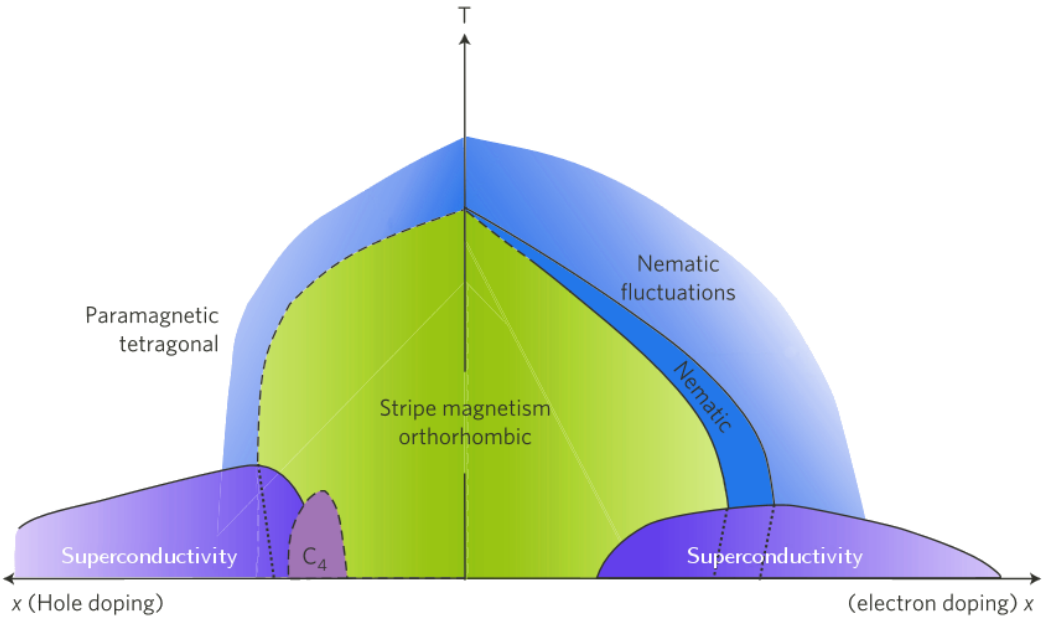


FIGURE 4.2: Generic phase diagram of iron pnictides for hole- and electron doping. The green area indicates stripe type magnetism in the orthorhombic state. The blue area denotes nematic/orthorhombic paramagnetic order, while the violet area corresponds to superconductivity. The pink area indicates a magnetically ordered state that preserves the tetragonal crystal structure. The dark blue area marks a regime with strong nematic fluctuations, while the dotted lines depict the nematic and magnetic transition lines inside the superconducting state. Solid (dashed) lines denote second-order (first-order) transitions. Upon doping the structural and magnetic phase transition are suppressed until SC emerges. Furthermore, a nematic state is observed as discussed in the text. Adapted from Ref. [55].

and almost 60 K [51]. While in some systems the transitions need to be completely suppressed for SC to set in, neutron diffraction measurements have shown that SC can coexist with AF order and even FM order [64].

The continuous suppression of magnetic order with doping or pressure suggests the existence of a quantum critical point (QCP) hidden inside the SC dome. The region above the tentative QCP is characterized by non-Fermi liquid behavior of the electronic system, e. g. a linear $T$-dependence of the electrical resistivity. Indeed, measurements of the Seebeck coefficient and the electrical resistivity in P-doped $EuFe_2As_2$ are compatible with a 2D magnetic QCP [65]. With further increasing $x$ SC is suppressed and Fermi liquid behavior is often recovered. The phase space between the structural and magnetic transition lines is characterized by an electronically driven nematic phase.

## 4.3 Nematic Phase

In the orthorhombic phase, the crystal lattice of the 122-type iron pnictides distorts along the basal plane diagonals of the tetragonal structure. As a consequence, the new orthorhombic unit cell rotates by approximately 45° around the $c$-axis and roughly doubles in size [33, 51, see also bottom row of Fig. 2.7]. The lattice distortion $\delta = a - b/(a + b)$ of order of 1 % is very small and leads to the formation of twin domains, as discussed in Chapter 2. This formation obscures the investigation of the in-plane anisotropy in these compounds. The anisotropy is of the order of 2, which is surprisingly large, considering the small lattice distortion. It is discussed in terms of an electronic nematic phase, which is said to drive the structural phase transition, i. e. nematic fluctuations are present in the tetragonal phase [55, 66]. The term nematic is borrowed from liquid crystal theory and refers to the breaking of rotational symmetry ($C_4 \rightarrow C_2$), while preserving translational and time reversal symmetry of the tetragonal system [67]. It is used to stress the fact that this breaking of rotational symmetry is driven by the electronic system rather than structural degrees of freedom, meaning that it would still happen in a system with a perfectly rigid lattice [66].

Several proposals have been made to explain the origin of this phase. One is that it is caused by a conventional structural transition induced by phonons. Another one is the development of spontaneous orbital order, which in the case of IBSCs manifests itself in different occupations of the Fe $d_{xz}$ and $d_{yz}$ orbitals [68]. Yet another proposal are magnetic fluctuations, which are no longer equivalent along $x$ and $y$ in this now-called "spin-nematic" phase, in which the long-range magnetic stripe order has yet to set in [56].

It is still a matter of debate which mechanism is responsible for the nematic order. At least, the first proposal seems unlikely, since the lattice distortion is much smaller than the electronic anisotropy, as already mentioned. However, it is very difficult to settle this debate, because the various types of order (structural, orbital, and spin-nematic) are strongly entangled, because they all break the tetragonal symmetry of the system. This means that one will always observe an anisotropy stemming from all types of order, because one leads to the appearance of the other two [55]. As the nematic phase—which is also discussed in the cuprates [69]—extends to high temperatures, far beyond the SC region, it could be essential for high-$T_c$ SC in general.

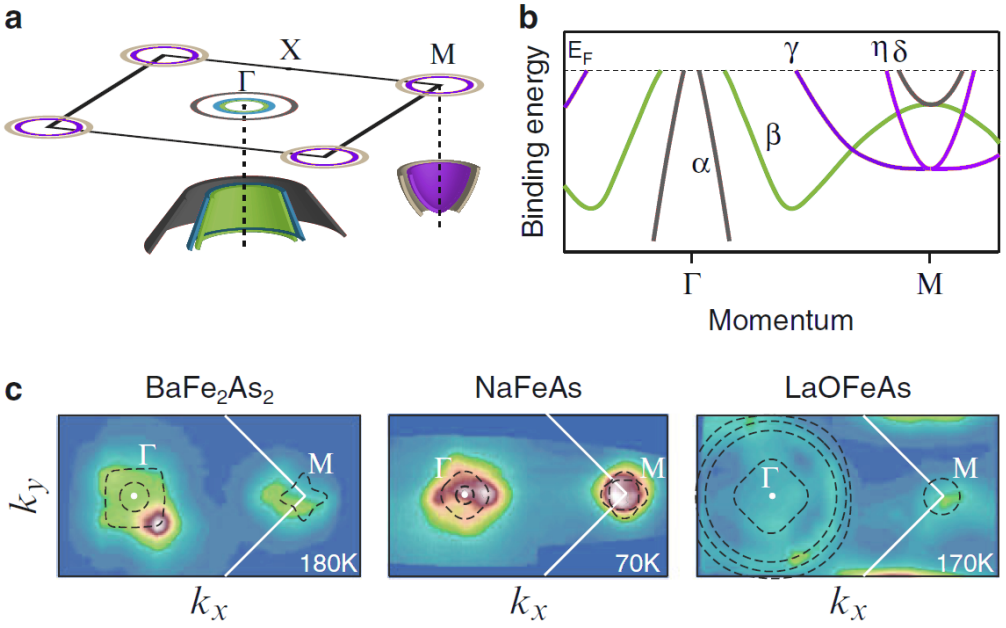


FIGURE 4.3: Electronic structure of undoped IBSCs. (a) Illustration of the Fermi surface topology of the "folded" Brillouin zone and (b) $\boldsymbol{\Gamma}$-$\boldsymbol{M}$ band dispersion, with $\alpha$, $\beta$, $\gamma$ and $\eta$ and $\delta$ denoting the hole-like and electron-like pockets of the Fermi surface, respectively. (c) Examples of ARPES intensity distributions for three prototypical iron pnictides in the tetragonal phase. Adapted from Ref. [48].

## 4.4 Electronic Structure

The electronic band structure of the IBSCs near the Fermi energy is dominated by the outer Fe $3d$ and pnictogen/chalcogen electrons. Although the details of the Fermi surface topology depend on the specific crystallographic structure and chemical doping-levels, all IBSCs have been found to exhibit multiband character with several hole and electron sheets of the Fermi surface in the Brillouin zone. The Fermi surface of the parent iron pnictides, for instance, consists of up to five electron-like and hole-like pockets (Fig. 4.3). Three hole-like pockets ($\alpha, \beta$, and $\gamma$) around the $\boldsymbol{\Gamma}$-point [$\boldsymbol{k} = (0, 0)$] and two electron-like sheets ($\delta$ and $\eta$) at the corners near the $\boldsymbol{M}$-point [$\boldsymbol{k} = (\pi, \pi)$] of the folded, i. e 2-Fe Brillouin zone (BZ). The outer hole sheet $\gamma$ has a more 3-dimensional character due to a larger dispersion along $\boldsymbol{k}_z$ compared to the other, more 2-dimensional sheets. Exemplary ARPES intensities of three typical iron pnictides are shown in Fig. 4.3(c).

'Folded' BZ refers to the actual (physical) BZ of the lattice. However, the electronic structure is also discussed in terms of the 'unfolded' BZ, particularly by theoreticians. This ambiguity is a frequent source of confusion and shall, therefore, be explained briefly.

The pnictogen/chalcogen atoms of the IBSCs have two non-equivalent positions above and below the Fe planes (see also Fig. 4.1). As a consequence, a layer has two Fe atoms ($Fe_2$) per unit cell, rather than one. The corresponding BZ of this lattice is called

folded. If, however, the pnictogen/chalcogen atoms are neglected, a simplified unfolded BZ is obtained, which is rotated by 45° and enlarged by a factor of $\sqrt{2}$ with respect to the folded BZ. For instance, the electron sheets at the $\boldsymbol{M}$-point of the folded BZ are, therefore, at the $\boldsymbol{X}$- and $\boldsymbol{Y}$-point of the unfolded BZ, etc. The folded BZ can be constructed by *folding*[2] the unfolded BZ, which explains the terminology.

Apart from the multiple Fermi surface sheets, the IBSCs also exhibit multi-orbital character. Band structure calculations, as well as, polarization-dependent ARPES measurements indicate that the hole and electron bands around the Fermi energy $E_\mathrm{F}$ consist primarily of the $t_2$ orbitals: $d_{xz}$, $d_{yz}$, and $d_{xy}$ with some degree of hybridization (orbital mixing) with the $e$ orbitals: $d_{z^2}$ and $d_{x^2-y^2}$ [70, 71]. The observed discrepancies between theoretical calculations of the Fermi surface topology and band structure on one hand and experimental results on the other hand indicate the correlated character[3] of the IBSCs [72–74]. In general, the correlation strength, e. g. the ratio of effective mass and band mass is smaller in iron-phosphides, while it increases in iron-arsenides and iron-chalcogenides. The reason is the successive increase of the iron-anion bond length, which leads to a reduction of the kinetic energy of the electrons [72, 75]. Furthermore, the observed correlations show orbital dependence, which seems to support the proposed [76] coexistence of itinerant and localized orbitals having weaker and stronger correlations, respectively.

In contrast to the single-band undoped cuprates, which are magnetic insulators, the parent compounds of the IBSCs are metallic multiband systems as indicated above. However, their electronic behavior is characterized by 'bad metal' properties, which manifest themselves in a large room temperature resistivity of about a few hundreds of $\mu\Omega$cm.

According to Ref. [68], a bad metal can be defined by the Mott-Ioffe-Regel criterion, which states that coherent metallic transport vanishes in systems where the mean free path of the carriers $l$ is of the order of the inter-atomic spacing: $k_\mathrm{F} l \sim 1$, where $k_\mathrm{F}$ denotes the Fermi wavevector. In IBSCs, usually 4 to 5 Fe $3d$-bands cross the Fermi energy and the estimated $k_\mathrm{F} l$ per band is indeed 1 [77]. This—together with the fact that electron-phonon interaction typically accounts only for several $\mu\Omega\,$cm of the electrical resistivity— implies significant electron-electron correlations.

Furthermore, a 70 % reduction of the spectral weight of the Drude peak compared to the case of non-interacting electrons has been observed in the real part of the optical conductivity $\sigma_1$ [78]. The area below $\sigma_1$ is proportional to the carrier density $N$, and

[2] Along the two face diagonals, which are shifted by $\pm a/2$ along the equivalent <110>-directions.

[3] The results of LDA calculations need to be renormalized and scaled in energy to fit the experimental data.

inversely proportional[4] to the effective mass, $m$, and thus the shift from the low-energy part of the spectrum to higher energies has been proposed as another indication for electronic correlations [68].

In addition, ARPES measurements indicate that this reduction is accompanied by an enhancement of the effective electron mass compared to the bare band mass in the paramagnetic state. The enhancement factor is 3-4 for iron pnictides [74, 79] and goes as high as 20 for some bands in iron chalcogenides [80–82].

Based on these experimental observations, it has been proposed that the parent compounds of the IBSCs are in the vicinity of a Mott transition [68]. In fact, ARPES measurements have found evidence for an orbital-selective Mott phase in doped iron chalcogenides [81, 82], which refers to the observation that only a subset of the Fe $3d$ orbitals undergo Mott localization[5] while the others stay itinerant. In particular, in the iron selenide system, the spectral weight of the $3d_{xy}$ orbitals vanishes at temperatures above 100 K, while for the $3d$ $xz/yz$ orbitals no change is evident [82].

## 4.5 Superconducting Order Parameter

The SC order parameter symmetry of the IBSCs is still a matter of debate. However, there is a consensus that the Cooper pairs are in a singlet state ($S = 0$), possibly with some sort of $s$-wave symmetry. The most favored at the moment is the so-called $s_{\pm}$-symmetry, but others, including $d$-wave character, are also being discussed. Figure 4.4 depicts cartoon sketches of several order parameters under consideration. The conventional $s$-wave symmetry (Fig. 4.4a) is given for reference. The $s_{\pm}$-symmetry (Fig. 4.4b) is commonly believed to be the accurate symmetry for most of the IBSCs at the moment, mostly due to the observation of a so-called resonance peak in neutron scattering experiments [56, 83]. Here the gaps on the hole and electron Fermi surfaces are isotropic, differing only in sign.

However, the $s_{\pm}$ gap function can have an angular variation, which leads to nodes (Fig. 4.4c). The positions of these nodes are not determined by symmetry and they are, therefore, called accidental nodes. The $d$-wave gap (Fig. 4.4d), on the other hand, has

[4] The f-sum rule relates the area below $\sigma_1$ to $N$, $m$ and the charge $q$, according to:

$$\int_0^\infty \sigma_1(\omega) d\omega = \frac{Nq^2\pi}{2m}.$$

[5] Mott localization refers to the localization of electrons due to electronic correlations, i. e. when the on-site Coulomb repulsion $U$ is much larger than the hopping term $t$, which models the kinetic energy of the electrons, see also Section 2.1.3.

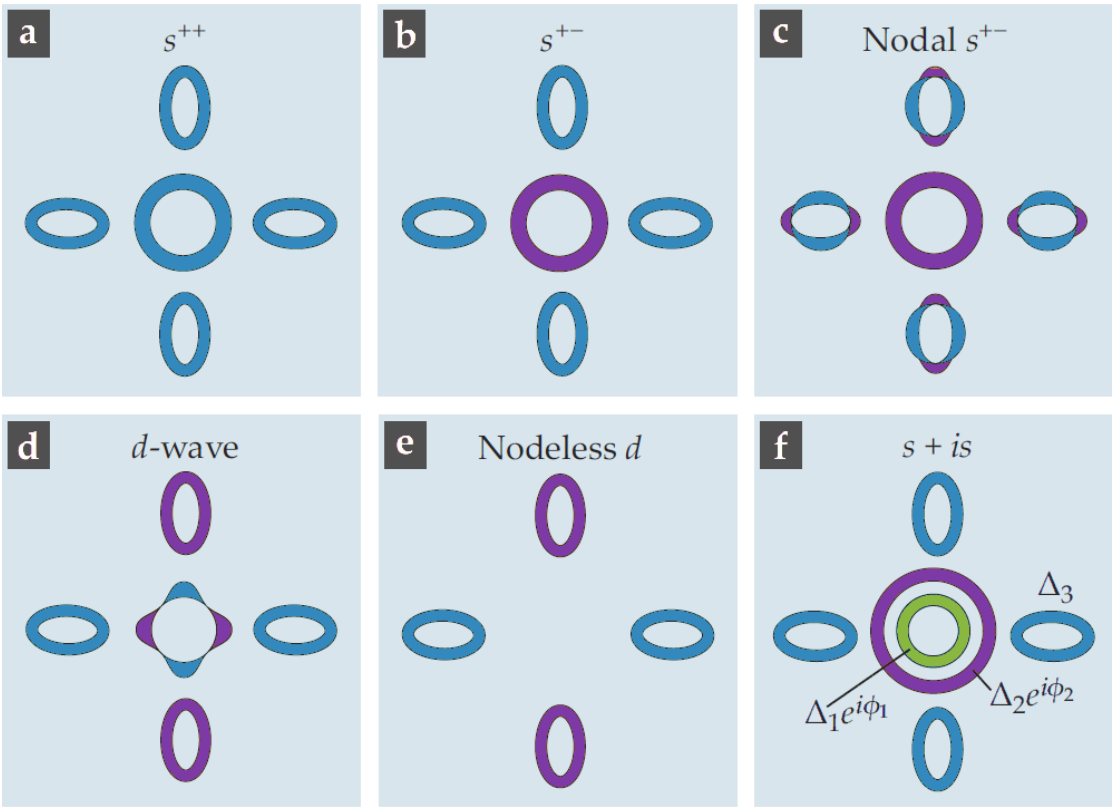


FIGURE 4.4: Superconducting gap functions of several $s$-wave and $d$-wave symmetries discussed for the IBSCs. Different colors indicate different signs of the gap. Adapted from Ref. [56].

nodes along certain symmetry directions, but only on the hole sheets. Without them the $d$-wave gap can be nodeless (Fig. 4.4e).

Another option in multiband systems (Fig. 4.4f) is a gap function similar to the $s_\pm$ case, but with an additional sign change between hole pockets, and a phase difference, which is no integer of $\pi$. A more detailed description regarding the superconducting order parameter of the IBSCs can be found in Refs. [56, 84].

## 4.6 Synthesis Methods

A variety of techniques are being used for the synthesis of IBSCs. Unlike the extensively studied cuprates, the IBSCs are not synthesized in open furnaces, due to the air- and moisture sensitivity of the reactants (rare-earths, alkali metals, and alkaline-earth metals) and the reactants toxicity or volatility, e. g. of arsenic and selenium. Furthermore, As and Se have high vapor pressures, which further complicates the crystal growth. Consequently, the preparation steps are carried out under inert atmosphere. For the synthesis the starting materials are typically sealed in silica tubes or metal crucibles

either in vacuum or also under inert gas atmosphere. The following sections give a brief overview of the most commonly used synthesis techniques of IBSCs. First, simple solid state reactions are covered, before the preparation of single-crystals is discussed.

### Polycrystals

The solid-state method was initially used for the IBSCs. Powders of the starting materials (elements or binaries) are stoichiometrically weighed and then heated to high temperatures. The reaction occurs within the solid state (no melting). The ions of the reactants diffuse across contact points between the grains. This diffusion can be significantly improved by raising the temperature, increasing the surface area through grinding of the starting materials, and by pressing the mixture into a pellet.

All of the main types of IBSCs can be synthesized with this method. For instance, the 11-type $FeSe_{1-x}$ system can be prepared according to

$$Fe + (1-x)Se \rightarrow FeSe_{1-x},$$

by annealing stoichiometrically weighed, mixed and pelletized powders of Fe and Se in an evacuated quartz tube at 700 °C for 40 h with an intermediate re-grinding [85], while e. g. the hole-doped 122-system $Ba_{1-x}K_xFe_2As_2$ can be fabricated according to

$$(1-x)Ba + xK + 2Fe + 2As \rightarrow Ba_{1-x}K_xFe_2As_2,$$

by placing stoichiometric amounts of the reactants in an alumina crucible sealed in a silica tube filled with argon [86]. The mixture is first pre-reacted at 600 °C for 15 h to reduce the vapor pressure of As and then—after an intermediate step of cooling, grinding and pelletizing the products—heated at 650 °C and 750 °C. The isovalently doped compound $BaFe(As_{1-x}P_x)$ can be synthesized in a similar fashion, requiring only higher reaction temperatures [87].

Apart from the solid-state method, polycrystalline samples can also be prepared using other methods such as the high-pressure method, the liquid ammonia method, or the hydrothermal method. However, these methods shall not be discussed here, but further information can be found in Refs. [88–90].

### Single Crystals

Two common ways to synthesize single crystals of the IBSCs are the Bridgman method and the flux method, which will be briefly introduced in the following. These methods

were used in this thesis to synthesize the $EuFe_2As_2$ compounds, as discussed in Chapter 3. Information on other methods, such as the high-pressure method [61, 91, 92] or the ammonothermal method [48, 49, and references therein], can be found in the respective literature.

### Flux Method

Metallic fluxes are commonly used for growing intermetallic compounds [93]. The goal is to reduce growth temperatures and increase the reactant diffusion [94]. In this way, materials can be synthesized that either melt incongruently, melt only at very high temperatures, or decompose before melting. Therefore, the typical flux is a solvent (to the reactants) with a low melting temperature that offers good solubility and diffusivity for the reactants. Furthermore, the flux must be easy to remove from the grown crystals and, in particular, should not be incorporated into the crystal (inclusions, chemical substitutions, etc.). Additionally, the flux must also not form stable compounds, that would compete with the desired system. In the case of the IBSCs, flux methods are typically used to grow the 122-type compounds. Rarely, is it used for the 11 and 1111 systems, however. [49].

Elemental metals like Sn ($T_{\mathrm{melt}} = 232\,^{\circ}\mathrm{C}$) and In ($T_{\mathrm{melt}} = 157\,^{\circ}\mathrm{C}$) are typical fluxes that can be used to grow mm-sized crystals of the 122-family. However, reports indicate that these flux materials are incorporated into the crystals. This can significantly change the intrinsic properties of the 122 systems [95, 96].

Single crystals can also be grown out of transition-metal arsenides ($T$As) according to:

$$A + 4T\mathrm{As} \rightarrow AT_2\mathrm{As}_2 + 2T\mathrm{As}$$
$$A + (4-x)\mathrm{FeAs} + xT\mathrm{As} \rightarrow A\mathrm{Fe}_{2-x}T_x\mathrm{As}_2 + 2T\mathrm{As},$$

with $A$ = Ca, Sr, Ba, Eu and $T$ = Cr, Mn, Fe, Co, Ni, Mo, etc. The $A$ to $T$As ratio ranges typically between 1:4 and 1:5 [49]. The growth technique is similar to the aforementioned methods. The starting materials are placed in an alumina crucible, which is sealed under partial inert gas atmosphere in a metal (Ta, Nb) crucible or silica tube. In the case of metal crucibles, the growth chamber has to be kept under inert gas as well to prevent oxidation of the crucible material. Typical growth profiles are: heating to 1180 °C, dwelling for about 5 h, cooling to slightly above $T_{\mathrm{melt}}$ of the flux ($\sim$ 1090 °C) by $\sim 3\,^{\circ}\mathrm{C\,h^{-1}}$, and then either quickly cooling to room temperature by switching off the furnace, or in the case of silica tubes, decanting the flux by spinning the growth assembly upside down in a centrifuge to separate the crystals from the flux (see also

Fig. 3.4). The remaining flux can either be removed mechanically, or by etching with acids.

The most common flux that is reported to produce large and high quality 122-type crystals is the binary FeAs ("self-flux") [97]. The crystals grow in a plate-like shape with the crystallographic $c$-axis perpendicular to the plate surfaces. This rather untypical flux with $T_{\mathrm{melt}} = 1042\,^{\circ}\mathrm{C}$ is prepared by careful solid-state reaction of powdered Fe and As. Special care must be taken, as arsenic sublimes and has a high vapor pressure (see Chp. 3 for more details).

#### Bridgman Method

The Bridgman method uses no flux for the growth of single crystals. Instead, a stoichiometric mixture of starting elements or binaries (in a sealed inert crucible) is heated above their melting temperatures (congruent melt). By slowly cooling, crystals grow (nucleate) out of the melt on the cooler part of the crucible due to an existing temperature gradient. This gradient can be established in different ways, e. g. by pulling either the crucible out of the furnace, or the furnace away from the crucible, or by reducing the furnace temperature, when the sample has previously been moved out of the homogenous heating zone of the furnace. Several modifications to this technique exist. For instance, the crucible can be rotated to improve sample homogeneity, or a point-bottom crucible with or without a seed crystal can be used to regulate and optimize the orientation and growth direction of the crystal.

Large several mm-sized single crystals of $A_x\mathrm{Fe}_{2-y}\mathrm{Se}_2$ ($A$ = K, Rb, Cs), $\mathrm{Fe}_{1.05}\mathrm{Te}$, and $\mathrm{Fe}_{1.03}\mathrm{Se}_{0.30}\mathrm{Te}_{0.70}$ were obtained using this technique. In fact, for the $\mathrm{FeTe}_x\mathrm{Se}_{1-x}$ system even very large cm-sized crystals could be grown [98–102]. There are also reports of relatively large crystals of 122 compounds grown with this technique [103, 104].

A disadvantage of this method is the high temperature that may be needed for the congruent melt, which, for instance, restricts the materials that can be used for the growth crucible.

## 4.7 Eu-based Iron Pnictides

In many regards $\mathrm{EuFe_2As_2}$ is a typical member of the 122 family of the iron pnictides: $M\mathrm{Fe_2As_2}$ ($M$ = Ca, Sr, Ba, and Eu). It is composed of alternately stacked layers of $[\mathrm{Fe_2As_2}]^{2-}$ and $M = \mathrm{Eu}^{2+}$. It crystallizes in the tetragonal $\mathrm{ThCr_2Si_2}$ structure with space group $I4/mmm$ and lattice parameters $a = 3.907(4)\,\text{Å}$ and $c = 12.114(3)\,\text{Å}$.

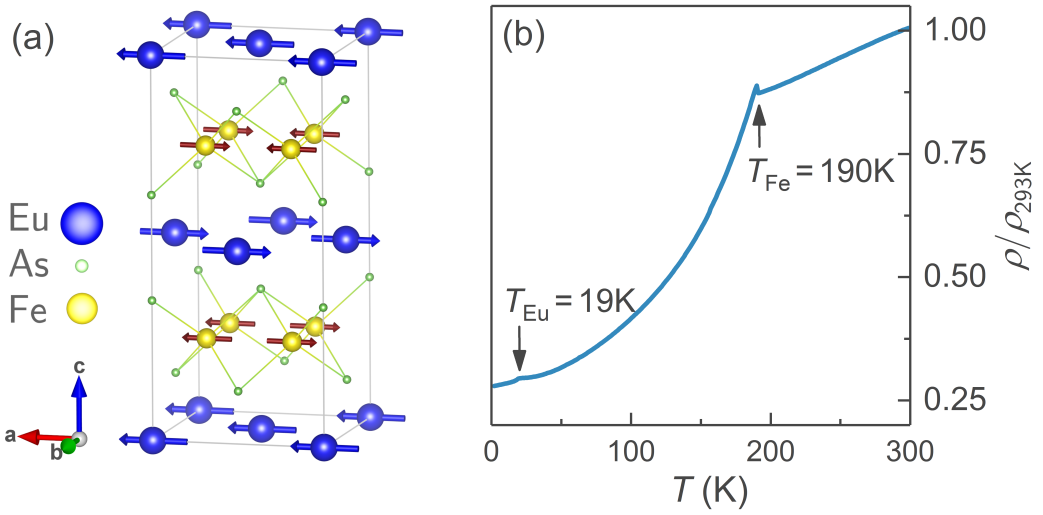


FIGURE 4.5: (a) Low-temperature magnetic structure and (b) in-plane electrical resistivity of $EuFe_2As_2$. Arrows indicate the structural and $3d$ magnetic ordering at $T_{Fe} \approx 190\,K$ and $4f$ AF ordering at $T_{Eu}$. Blue and red arrows indicate the Eu $4f$ and Fe $3d$ ordered moments, respectively. Adapted from Ref. [105].

However, it has one feature that sets it apart from the other 122 systems, namely, its large localized $4f$ magnetic moments, which stem from the Eu ions. These moments lead to a rich and intriguing phase diagram, and to an intricate interplay between structural order, Fe and Eu magnetism, and superconductivity. In the following, a short review on the Eu-based iron pnictides, with a particular focus on the interplay between the Fe $3d$ and Eu $4f$ moments, is given. We recently published a review on the same topic in Physica Status Solidi, which can be consulted for further details [105]. After the introduction of the parent compound $EuFe_2As_2$, the effect of carrier doping, exemplified for the case of K-doping on the Eu site, is discussed. This is followed by the cases of hydrostatic and chemical pressure. Finally, the less investigated systems $Eu(Fe_{1-x}Ru_x)_2As_2$ and $Eu_{1-x}Ba_xFe_2As_2$ will briefly be covered.

$EuFe_2As_2$ undergoes a structural transition from the tetragonal to the orthorhombic structure (space group: *Fmmm*) in conjunction with a SDW ordering of the Fe $3d$ moments around 190 K. The $3d$ moments order in the typical stripe structure with the ordering vector $\boldsymbol{k} = (1, 0, 1)$. Fe spins are ordered AF along the $a$-axis and $c$-axis, while the arrangement along the $b$-axis is FM. Additionally, the Eu $4f$ moments order in a so-called A-type AF structure below $T_{Eu} = 19\,K$, with the ordering vector $\boldsymbol{k} = (0, 0, 1)$. This refers to FM order (in-plane) along the $a$-axis and AF order along the $c$-axis (Fig. 4.5a) [106]. The effective moment per $Eu^{2+}$ is with roughly $7.5\,\mu_B$, close to the expected free-ion value of $7.94\,\mu_B$ for a $S = 7/2$ ion, while the moment per Fe atom was estimated to $1.8\,\mu_B$, which corresponds to one unpaired electron ($S = 1/2$) [107].

A metamagnetic transition of the $Eu^{2+}$ moments to FM order can be induced by small magnetic fields around 1 T [108].

The in-plane electrical resistivity $\rho(T)$ (Fig. 4.5b) exhibits metallic behavior down to $T_{Fe}$, where a small but sharp increase signals the gap formation of the SDW state [109]. At $T_{Eu} = 19\,K$ another hump is evident, that appears due to the $4f$ magnetic ordering. Typical values for the in-plane electrical resistivity of $\rho(300\,K) = 630\,\mu\Omega cm$ and $\rho(2\,K) = 200\,\mu\Omega cm$ indicate bad metal behavior as discussed in Sec. 4.4. The temperature dependence along the $c$-axis is qualitatively similar, but absolute values of $\rho$ are enhanced by a factor of 8 [110], indicating that the electrical transport occurs mostly within the FeAs-layers.

As implied by band-structure calculations [109], the electronic structure of $EuFe_2As_2$ is similar to its sister compound $SrFe_2As_2$, which contains no $4f$ moments. Consequently, it is not surprising, that SC can be induced in $EuFe_2As_2$ by similar means. In particular, electron and hole doping as well as chemical or hydrostatic pressure lead to SC [65, 105, 108, 111–113].

### Carrier doping

The unreconstructed Fermi surface (FS) of $EuFe_2As_2$ consists of three hole-like sheets near the $\boldsymbol{\Gamma}$-point and two electron-like sheets near the $\boldsymbol{M}$-point of the folded Brillouin zone [114, 115]. The outer hole-like sheet has a more 3D character than the other two, due to a larger dispersion along $\boldsymbol{k}_z$. The SDW order is related to FS nesting, as mentioned in Chapter 2. The corresponding nesting vector $\boldsymbol{Q}_n$ points along the $\boldsymbol{\Gamma}$-$\boldsymbol{M}$-direction. Upon hole-doping, e. g. by replacing $Eu^{2+}$ with $K^{1+}$, the electron-like sheets shrink, while the hole-like sheets expand within the $k_xk_y$-plane. This leads to a reduction of the nesting condition, which causes a suppression of $T_{Fe}$ [115].

The phase diagram of $Eu_{1-x}K_xFe_2As_2$, as derived from resistivity and susceptibility data, (Fig. 4.6a) reveals several phases. A paramagnetic (tetragonal) phase at high temperatures and the SDW (orthorhombic) state at low $T$, which extends up to $x \approx 0.2$. Above $x \approx 0.3$, bulk SC with a $T_c$ of up to 34 K for $x = 0.5$ develops [108, 111]. Furthermore, the AF order of the $4f$ moments below $T_{Eu}$ weakens with doping until it disappears around $x = 0.5$. Coexistence of $Eu^{2+}$ short-range magnetic order with SC has been shown by Mössbauer spectroscopy [116]. The bulk nature of the SC has been confirmed by a sharp anomaly in the specific heat [117] and a strong Meissner effect in the magnetic susceptibility [111]. A SC gap $2\Delta_0 = 9.5\,meV = 3.7k_BT_c$ with $s$-wave symmetry and no nodes has been confirmed by optical conductivity measurements [118]. Electron spin resonance (ESR) measurements additionally found that the spin-lattice relaxation rate $1/T_1^{ESR}$ follows the Korringa relaxation $\sim T$ for simple metals

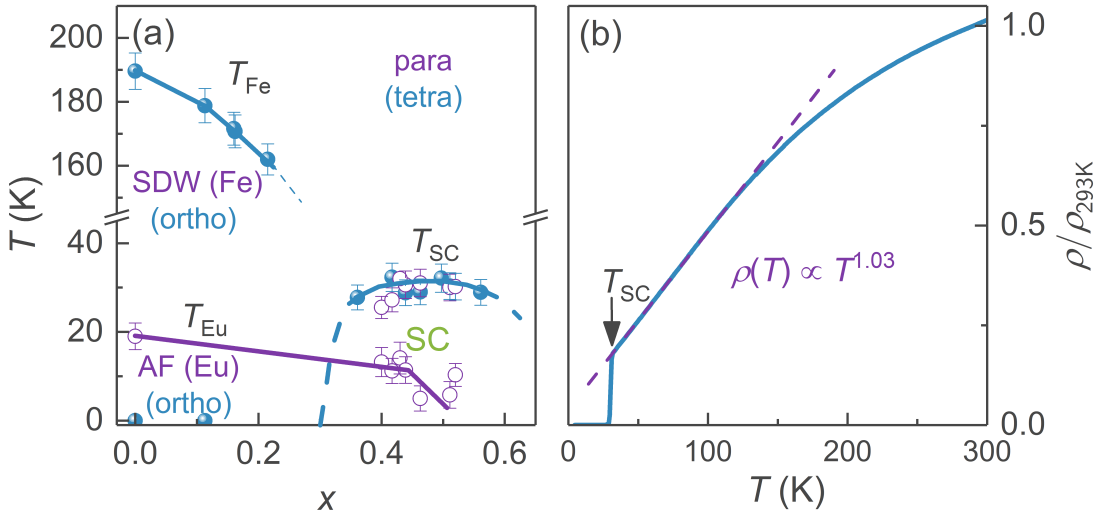


FIGURE 4.6: Effects of hole-doping in $EuFe_2As_2$. (a) Phase diagram of $Eu_{1-x}K_xFe_2As_2$. Solid symbols (blue) correspond to phase transition temperatures derived from resistivity data, while open (violet) symbols were extracted from susceptibility measurements. Lines are guides to the eye. (b) Normalized in-plane electrical resistivity of a near optimally doped (x=0.51) crystal. The dashed line accentuates the non-Fermi liquid behavior $\rho(T) = \rho_0 + AT^n$, with $n = 1.03$, while the arrow indicates the SC transition temperature $T_c$. Adapted from Ref. [65].

above 45 K. Below 45 K, clear deviations are evident, which signal the onset of magnetic fluctuations of the FeAs layers and a subsequent evolution of $1/T_1^{ESR} \sim T_1^{1.5}$ in the SC state. No Hebel-Slichter peak is observed, indicating a non-BCS (non $s$-wave) pairing scenario [119].

Diluting the $Eu^{2+}$ magnetic sublattice with K weakens the ordering of the $4f$ moments and reduces $T_{Eu}$. Eventually, the order of the $Eu^{2+}$ spins changes from long-range to short-range into a glassy frozen state near $x = 0.5$. This short-range order is demonstrated by a dip in the temperature dependence of the magnetic penetration depth near 5 K [120].

The suppression of the SDW order upon hole-doping and the emergence of SC might indicate the existence of a quantum critical point (QCP) in the vicinity of optimal doping $x = 0.5$. In fact, we reported evidence for a 2D SDW QCP in the form of a linear $T$-dependence of the electrical resistivity (Fig. 4.6b) and a logarithmic divergence in $S(T)/T$ of the Seebeck-coefficient $S$ earlier [65]. Similar behavior was also observed in other iron pnictides, like hole-doped $SrFe_2As_2$ [121]. Nonetheless, the temperature range in which this behavior is observed is rather small, leaving room for interpretations other than QC behavior. Indications for a so-called Lifshitz transition that might be related to the suppression of the SDW ordering have also been observed in the form of an anomaly in the doping dependence of the Seebeck coefficient $S(x)_{T=\text{const.}}$ near $x = 0.3$. In this context, a Lifshitz transition [122] refers to the situation when a Fermi surface

sheet of either hole-like or electron-like character crosses the Fermi surface upon doping or application of pressure.

**Chemical & hydrostatic pressure**

The suppression of the SDW order and consequent emergence of SC in $EuFe_2As_2$ can also be observed upon application of hydrostatic pressure of 2.5 GPa [112, 123]. Furthermore, a one-to-one correspondence between the P-doping and applied pressure has been found. P is smaller than As and subsitution leads to a linear decrease of the $c$-lattice parameter and the unit cell volume with $x$ [103]. Therefore, P-doping has a chemical pressure effect on $EuFe_2As_2$. The respective phase diagram (Fig. 4.7) has been established from P-doped samples at ambient conditions and under hydrostatic pressure. The effective P concentration under hydrostatic pressure was obtained by using the bulk modulus and lattice constants of $EuFe_2(As_{1-x}P_x)_2$ [124]. Most notably, the SC region is confined to a narrow range between $x = 0.18$ and 0.23 in this compound. This is in stark contrast to systems like $BaFe_2(As_{1-x}P_x)_2$, where SC forms over a broad range of doping concentrations [125, 126]. One reason for this behavior might be the presence of the large and ordered $Eu^{2+}$ magnetic moments, which could be detrimental for SC, despite a report of the coexisting SC and FM $Eu^{2+}$ order in a $x = 0.3$ polycrystal [127]. However, it is more likely that this behavior is caused by electronic changes driven by a Lifshitz transition of the inner hole-sheet in the first Brillouin zone (see discussion below).

ARPES data on $EuFe_2(As_{1-x}P_x)_2$ revealed that the electron-sheets at the Brillouin zone corners stay basically unchanged upon doping, while the inner hole-like sheets become more 3D, as a consequence of the $c$-axis compression and the resulting decrease in the $c/a$ ratio [103]. This decrease in the Fermi surface nesting leads to the continuous suppression of the structural and magnetic phase transitions (Fig. 4.7).

In the case of P doping on the As site, the Eu sublattice remains intact and a change from AF to FM order above $x = 0.23$ has been inferred from magnetization measurements with a field applied within the ab-plane [124]. However, recent neutron diffraction data revealed that the $Eu^{2+}$ moments order ferromagnetically and point along the c-axis already for $x = 0.19$ [128]. The proposed gradual canting of the $4f$ moments out of the ab-plane with increasing $x$, as derived from bulk magnetization measurements [129], was not confirmed [128]. The optimal doping with a $T_c^{max} = 28\,K$ is found around $x = 0.19$. SC coexists with $Eu^{2+}$ order only in a very narrow range [103], where the system is presumably, still in the SDW state with orthorhombic lattice symmetry [103, 124]. The abrupt change from AF to FM order, which is followed by the disappearance of SC, was confirmed by additional in-plane magnetization measurements [129]. ARPES indicates a vanishing of the inner hole-sheet around $x = 0.23$ [115], which is in agreement with

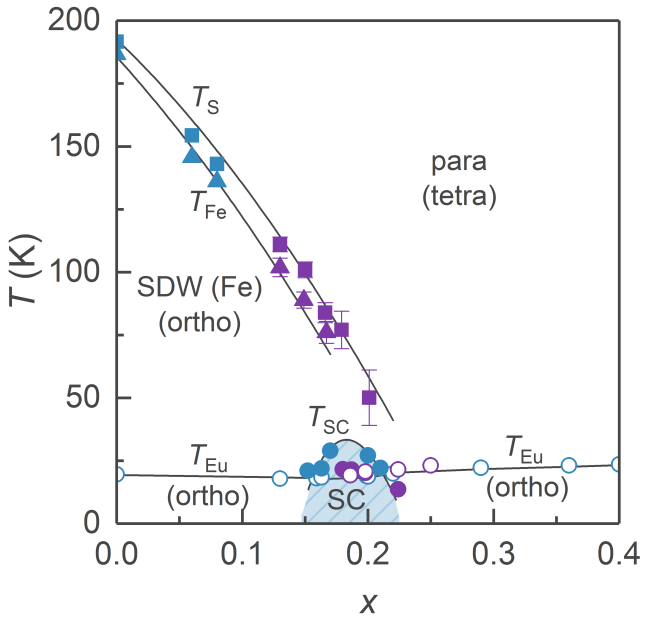


FIGURE 4.7: Phase diagram of $EuFe_2(As_{1-x}P_x)_2$ determined at ambient pressure (blue symbols) and under hydrostatic pressure (violet symbols). The structural $T_S$ and Fe SDW transition $T_{Fe}$ seperate upon doping. The system features a small SC region below $T_{SC}$. The Eu ordering temperature $T_{Eu}$ is virtually not affected by doping. Adapted from Ref. [124].

the non-monotonic evolution of the Seebeck coefficient $S(x)_{T=\text{const}}$ around the same concentration [65].

As in $Eu_{1-x}K_xFe_2As_2$, the $EuFe_2(As_{1-x}P_x)_2$ system exhibits distinct non-Fermi liquid behavior in the form of a linear electrical resistivity and a logarithmic divergence of $S/T$ [65]. Recent ARPES measurements found a linear energy dependence, but no enhancement of the scattering rates close to the expected QCP. The deviations from Fermi liquid predictions in the normal state have, therefore, been interpreted in terms of a Lifshitz transition, which causes an anomalous band dispersion at the Fermi level. This leads to a strong enhancement of the quasiparticle mass in the normal state [130].

**Fe Dilution**

Another way of isovalent doping in $EuFe_2As_2$ is replacing Fe atoms with non magnetic Ru. Therefore, this substitution serves also as a way of diluting the Fe moments. Only few data are available on this system. From investigations of polycrystalline samples it became evident that Ru substitution is capable of tuning the system through the phase diagram similar to P, although it influences the unit cell volume muss less than P. SC is only found in a narrow range around $x = 0.2$, the maximal $T$ at which it sets in is 24 K [131]. The authors of Ref. [131] also claim a change of the $Eu^{2+}$ order from AF to FM before the onset of SC, and hence a coexistence of the two. However, the ordering

temperature of the $Eu^{2+}$ moments stays virtually constant throughout the entire doping range.

### Eu Dilution

One way of diluting the Eu magnetism without doping carriers to the system is by substituting Ba on the Eu site. However, Eu dilution has mostly been studied in superconducting Co-doped compounds by means of Sr substitution, $Sr_xEu_{1-x}(Fe_{1-y}Co_y)_2As_2$. Here, the dilution has been found to stabilize SC and enhance its transition temperature [132–134].

This concludes the presentation of the Eu-based iron pnictides. For additional information one can refer to a very recent and comprehensive review of the Eu-based iron pnictides [135].

Chapter 5

# Sample Characterization

This chapter presents basic properties of the synthesized single crystals. It provides a characterization of the samples used for the investigation of the magnetically induced detwinning effect in the following chapters. It starts with the $EuFe_2As_2$ system, followed by the magnetically diluted systems $Eu_{1-x}Ba_xFe_2As_2$, and $Eu(Fe_{1-x}Ru_x)_2As_2$. The characterization includes both structural as well as electrical transport properties. A brief discussion of the surface topology and the effect of annealing in $Eu(Fe_{1-x}Ru_x)_2As_2$ is given in Appendix A. Furthermore, the influence of different growth techniques, i. e. sample dependence of the transport properties of the parent compound are also discussed.

High-quality single crystals of the $EuFe_2(As_{1-x}P_x)_2$ series were already available. Their specific synthesis conditions and characterization measurements were reported elsewhere [103, 109]. Additionally, reference samples of the parent compound were provided by H. S. Jeevan (Sn-flux) and S. Jiang (FeAs-flux).

## 5.1 The Parent Compound - $EuFe_2As_2$

Single crystals of $EuFe_2As_2$ were prepared using the ultra-low-flux method, as introduced in Chapter 3. The samples were subsequently characterized using x-ray powder diffraction (XRD), Laue imaging, and electrical transport.

All (non-Si) peaks on the room-temperature XRD pattern (Fig. 5.1) could be indexed using the $ThCr_2Si_2$-type tetragonal structure reported for $EuFe_2As_2$. No foreign phases were observed. The room-temperature lattice parameters have been refined to $a = 3.912(4)$ Å and $c = 12.175(12)$ Å in excellent agreement with literature reports [109, 136, 137]. A representative Laue diffraction pattern (Fig. 5.10a), also recorded at room

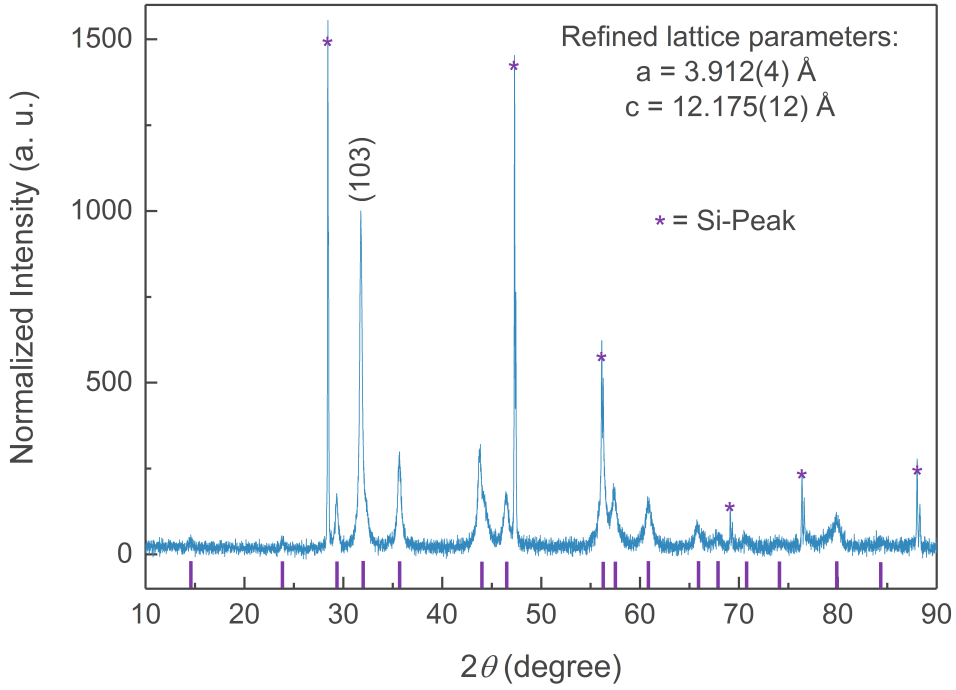


FIGURE 5.1: Representative x-ray powder diffraction pattern of $EuFe_2As_2$ normalized to the (103)-reflection. Violet markers indicate the peaks indexed with the $ThCr_2Si_2$ type tetragonal crystal structure, while stars indicate Si reference peaks. The pattern indicates a phase-pure sample of $EuFe_2As_2$.

temperature, shows sharp Bragg reflections, which are visible over a large angular range and with only a small diffuse background. These measurements, therefore, confirm that the samples are phase-pure and of high structural quality compared to typical 122-type iron pnictides.

The in-plane resistivity of $EuFe_2As_2$ exhibits metallic behavior at high temperatures (Fig. 5.2a) with the typical linear $T$-dependence. Around $T_{Fe} = 190\,K$, the structural and electronic phase transitions to the orthorhombic and antiferromagnetic stripe-ordered state of Fe occur. Below $T_{Fe}$, the steep decrease of $\rho$ signals this SDW state. The evolution is only interrupted by the onset of AF order in the Eu subsystem, in form of a hump around $T = 19\,K$. The evolution of the resistivity of the (UltraLow-flux grown) sample is, therefore, in good agreement with previous literature reports and the residual resistivity ratio (RRR) is with 7.1 comparatively large [38, 105, 109].

### 5.1.1 Sample dependence

Samples synthesized using FeAs-flux and Sn-flux show a similar temperature evolution of the resistivity (Fig. 5.2a) as the UltrLow-flux grown sample. The ordering temperature of the $Eu^{2+}$ moments (19.4 K) is virtually identical in all three samples and so is $T_{Fe}$ for the two samples grown in Sn-flux and UltraLow-flux, while the transition temperature of

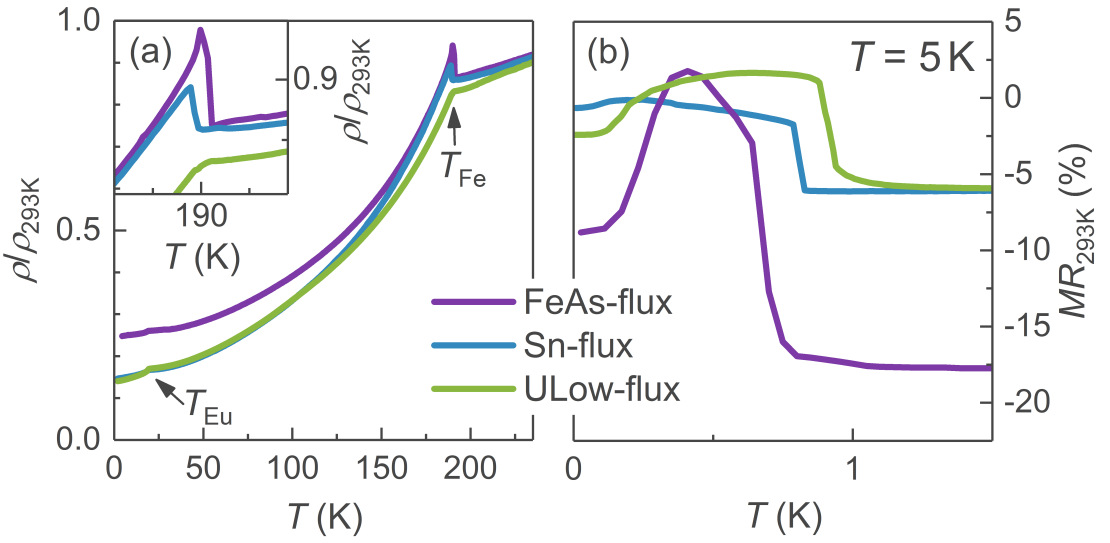


FIGURE 5.2: Electrical transport of $EuFe_2As_2$ crystals grown with different techniques, namely Sn-flux, FeAs-flux and Ultralow-flux. (a) Normalized in-plane resistivity with an (inset) enlarged view around $T_{Fe} \approx 190\,K$. (b) Magnetoresistance for increasing field normalized to $\rho_{293\,K}$ to reduce influence of the residual resistivity. Sn-flux and FeAs-flux samples were synthesized by H. S. Jeevan and S. Jiang.

the FeAs-flux grown sample is enhanced by roughly 1 K. Otherwise, the sample grown in FeAs-flux appears to be of lesser quality, since its RRR with a value of 4 is significantly smaller than that of the other two with a value of about 7. However, the lower RRR could also indicate an imbalance of twin domains, with more of the longer $a$-axes in measurement direction (see discussion below).

Despite the large RRR of the UltrLow-flux grown sample, the sharp increase of the resistivity directly at $T_{Fe}$ is virtually absent, while the corresponding increase in the FeAs-flux grown sample is pronounced. This increase has been attributed to the reduction of the density of states at the Fermi level due to the gap opening in the SDW phase [65, 105, 109]. Similar behavior has been observed in other systems that feature a SDW transition, like elemental Cr [138], $URu_2Si_2$ [139, 140], $PrAu_2Ge_2$ [141, 142], and $CeCu_2Si_2$ [143]. An explanation for the notable sample dependence of this increase is that the samples form an uneven distribution of a-twin and b-twin domains (an excess of the $a$ and $b$ parameter in the measurement direction, respectively) below $T_{Fe}$, leaving it partially detwinned. As we will see below, mechanically detwinned samples show that the resistivity measured along the crystallographic $a$-axis does not exhibit a notable increase at $T_{Fe}$, while $\rho(T)$ along $b$ does [38, and Fig. 6.10]. This observation is in agreement with the proposal of orbital ordering and a resulting uneven occupation of the $d_{xz}$ and $d_{yz}$ orbitals [144, 145] and, therefore, supports the claim of partially detwinned single crystals.

The magnetoresistance (MR) throughout this thesis is defined by $[R(H) - R(H =$

$0)]/R(293\,K)$, where $R(H = 0)$ refers to the final resistance value at $H = 0$ *after* the field sweep. The normalization to the room-temperature resistance $R(293\,K)$ was chosen over the standard convention (the measurement temperature, here typically at 5 K) in order to minimize any influence of defect scattering on the magnitude of the MR. This improves the comparability not only between different growth techniques, but also between different doping series.

The MR of $EuFe_2As_2$ (Fig. 5.2b) will be discussed in detail in Chapter 6. Here it is sufficient to note that there is a sample-dependent difference in the position of characteristic features, like the step-like decrease around ∼1 T and the maximum around ∼0.5 T, as well as a variation of the overall magnitude of the MR. However, this sample dependence does not affect the discussion of the magnetic detwinning effect qualitatively. It merely leads to a wider statistical spread of the derived constants in Chapter 6. Although the sample dependence is not critical to the following discussions, it might be helpful to the reader to keep it in mind.

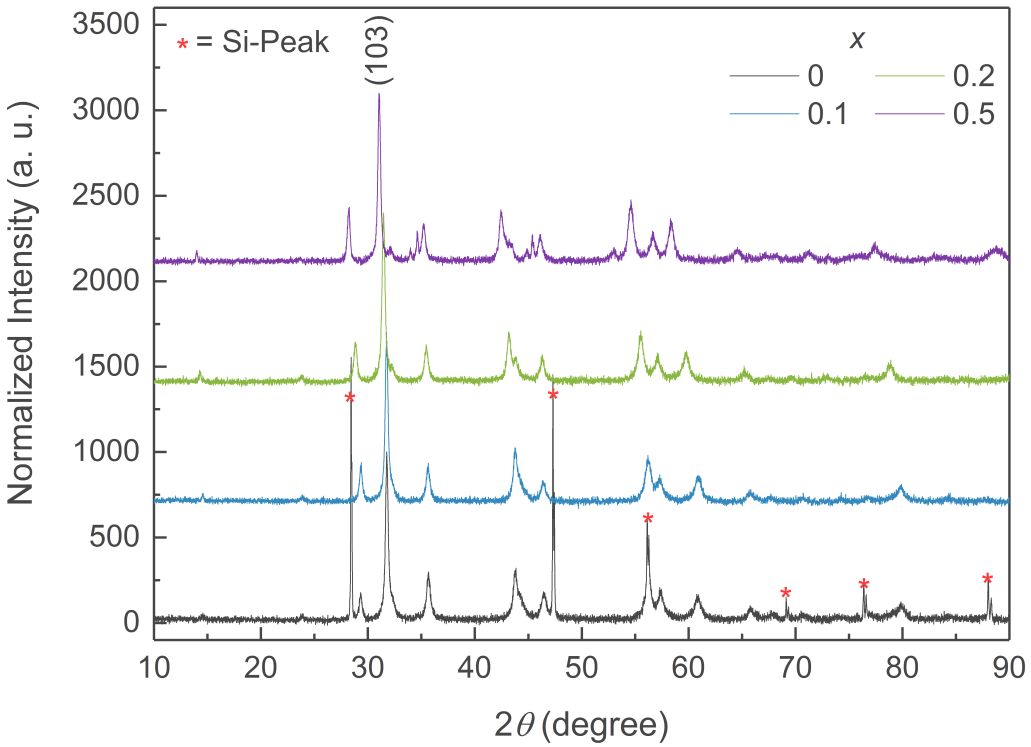


FIGURE 5.3: XRD patterns of $Eu_{1-x}Ba_xFe_2As_2$ for various $x$ normalized to the (103)-reflection and vertically shifted by 700 counts for clarity. Red stars indicate Si reference peaks.

## 5.2 Dilution of Eu-Moments - $Eu_{1-x}Ba_xFe_2As_2$

The substitution of Eu with Ba is an effective dilution of the $4f$ magnetic moments, as Ba is nonmagnetic. Three samples with nominal composition $x = 0.1$, 0.2, and 0.5 were synthesized using the self-flux method discussed in Sec. 3.2 and subsequently characterized.

The XRD Bragg-reflections (Fig. 5.3) exhibit a gradual shift to lower $2\Theta$ values, i. e. larger lattice spacings with increasing $x$, particularly for the $x = 0.5$ sample. The intensities are normalized to the (103) reflection and offset by 700 counts for clarity. The extracted lattice parameters and the unit cell volume (Fig. 5.4a-b) have an overall

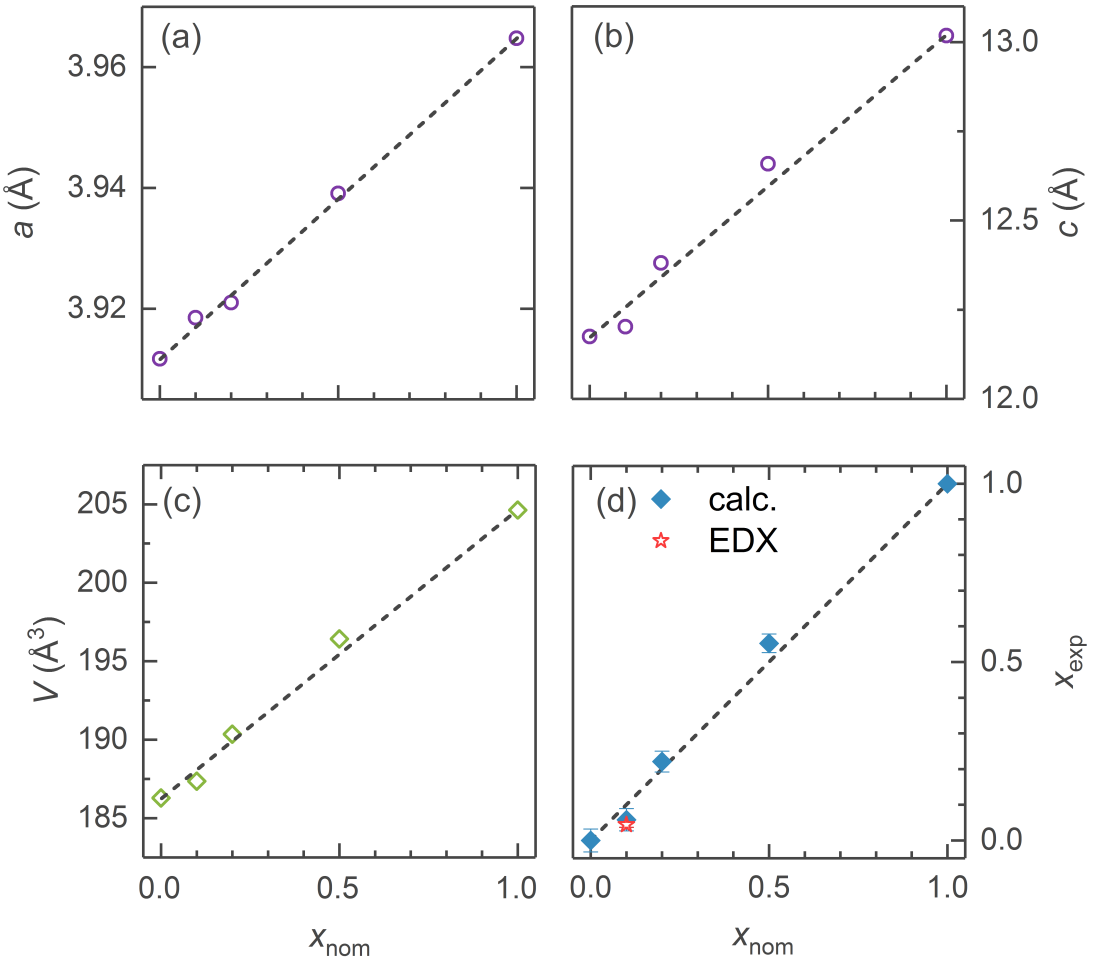


FIGURE 5.4: Lattice parameters and doping levels of $Eu_{1-x}Ba_xFe_2As_2$ as a function of $x$ extracted from XRD data. Refined room-temperature values for the (a) $a$-axis, (b) $c$-axis, and (c) unit cell volume. (d) Experimental Ba concentration $x_{exp}$ against nominal concentration $x_{nom}$ calculated using Vegard's law ($V$). The result for $x = 0.5$ should be taken with caution, as discussed in the text. The red star represents EDX data for comparison, while the dashed lines are guides to the eye. If not visible, error bars are within the symbols size. Data for $x = 1$ are taken from Ref. [146].

linear progression with $x$, following Vegard's law. However, the $c$-axis around $x = 0.5$ shows a slightly positive deviation.

Vegard's law—which, despite its name, is an approximation—typically holds when the lattice parameters of the end member compounds vary by less the 5 % [147]. The $c$-axes of $BaFe_2As_2$ and $EuFe_2As_2$ differ by roughly 7 %, while the $a$-axes differ by only 1.3 %. Therefore, a deviation from Vegard's law cannot be excluded in the case of $Eu_{1-x}Ba_xFe_2As_2$ for large $x$.

The ratio of the unit cell volumes $V_{Ba}/V_{Eu} = 1.098$ and the evolution of the lattice parameters are plausible, considering that the ionic radius of $Ba^{2+}$, $r_{Ba} = 149\,\text{pm}$, is roughly 14 % larger than that of $Eu^{2+}$ with $r_{Eu} = 131\,\text{pm}$. The unit cell volume (Fig. 5.4c) shows a linear evolution with $x$. Due to a lack of extensive EDX data, the doping concentrations of the Ba-doped samples were, therefore, estimated from the unit cell volume using Vegard's law:

$$x = \frac{V(x) - V_{Eu}}{V_{Ba} - V_{Eu}}.$$

The value obtained for the $x = 0.5$ sample should be taken with some caution, due to the slight deviation of the $c$ lattice parameter, which might impact the result. Otherwise, the experimental results $x_{exp}$ (Fig. 5.4d) are in good agreement with the nominal concentrations $x_{nom}$, indicating differences of only a few percent, which is supported by EDX data in the case of the $x = 0.1$ sample.

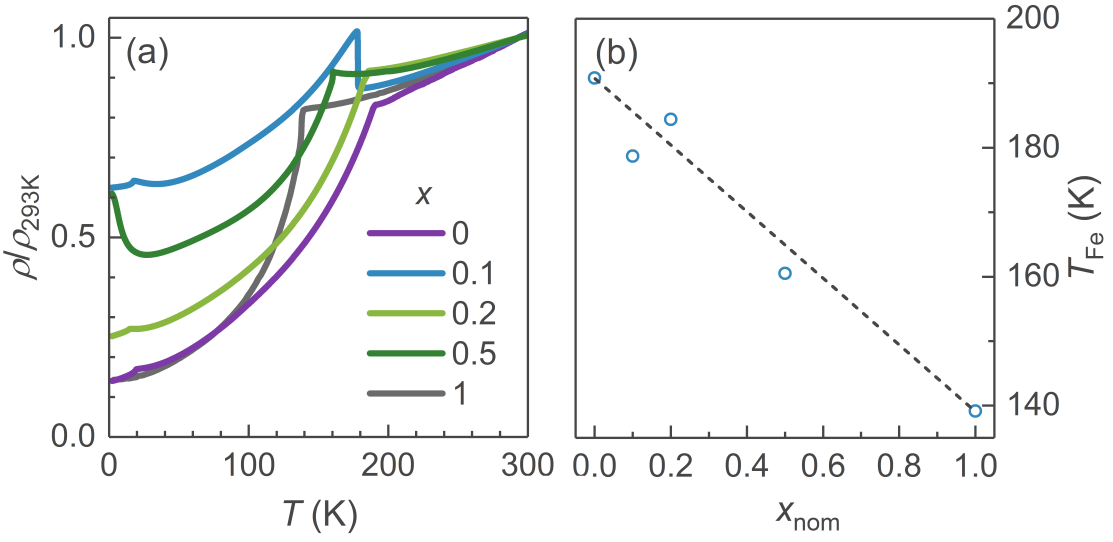


FIGURE 5.5: Electrical transport of $Eu_{1-x}Ba_xFe_2As_2$. (a) In-plane resistivity as a function of temperature for various Ba concentrations $x_{nom}$. (b) Evolution of $T_{Fe}$ as a function of $x_{nom}$. Data for $x = 1$ are taken from Ref. [148].

A representative Laue diffraction pattern (Fig. 5.9b) is depicted together with other Laue patterns in the following section. The reflections are sharp, clear and visible over a large angular range, with a modest diffuse background, indicating high sample quality. These results suggest that the $Eu_{1-x}Ba_xFe_2As_2$ system is a solid solution, in which the Ba atoms are randomly distributed within the Eu sublattice.

The in-plane resistivity (Fig. 5.5a) of $Eu_{1-x}Ba_xFe_2As_2$ shows significant changes upon doping. The high-temperature transition $T_{Fe}$ decreases roughly linearly in $T$ as more Eu is replaced with Ba (Fig. 5.5b). More specifically, it is reduced from about 190 K to 179 K, 160 K, and 140 K for $x = 0$, $x = 0.1$, $x = 0.5$, and $x = 1$, respectively. However, the sample with $x = 0.2$ shows a higher $T_{Fe}$ with 183 K. The upturn of $\rho(T)$ at $T_{Fe}$ increases significantly for $x = 0.1$, but dwindles again for higher concentrations, which might indicate an uneven formation of twin domains at $T_{Fe}$, as already indicated above. The ordering temperature of the $Eu^{2+}$ moments, defined by the drop in $\rho(T)$, continuously decreases with increasing doping from initially 19.3 K for $x = 0$, to 17.7 K, and 14.8 K for $x$ =0.1 and 0.2, respectively. No drop in $\rho$ is visible at low temperatures for $x = 0.5$. The RRR values of the doped samples are significantly reduced, naively indicating disorder induced by doping. However, an additional effect to the RRR due to the uneven formation of twin domains can not be excluded. Therefore, it is difficult to uniquely ascribe the drop in RRR to induced disorder.

$T_{Fe}$ of the sample with $x = 0.5$ is substantially decreased and the increase in $\rho(T)$ at $T_{Fe}$ is almost completely gone. A similar behavior was also observed in $BaFe_2As_2$ [149]. At temperatures below $T = 40$ K, the resistivity rapidly increases in a Kondo-like fashion,

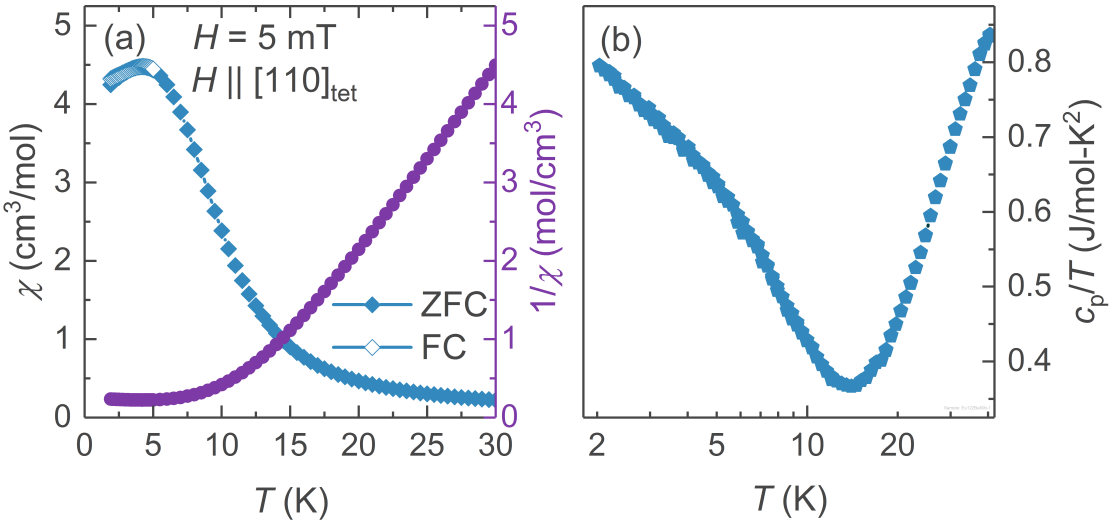


FIGURE 5.6: (a) Magnetic susceptibility $\chi$ and its inverse $1/\chi$ of $Eu_{1-x}Ba_xFe_2As_2$ with $x_{nom} = 0.5$ as a function of temperature. (b) Specific heat over temperature $c_p/T$ plotted as a function of $T$.

because the diluted $Eu^{2+}$ moments likely act as randomly distributed scattering centers for the conduction electrons. A positive Weiss temperature evident from the inverse magnetic susceptibility $1/\chi$ indicates predominantly FM interactions (Fig.5.6). $\chi$ itself exhibits a broad peak around 5 K, characteristic for a spin-glass-like freezing of the $Eu^{2+}$ moments. The shoulder visible in the specific heat over temperature $c_p/T$ around the same point is consistent with this picture.

## 5.3 Dilution of Fe-Moments - $Eu(Fe_{1-x}Ru_x)_2As_2$

Single crystals of $Eu(Fe_{1-x}Ru_x)_2As_2$ were synthesized for various $x$ using the UltraLow-flux method described in Sec. 3.2. Replacing Fe with nonmagnetic Ru dilutes the Fe magnetism, reduces the ordering temperature $T_{Fe}$, and eventually leads to superconductivity [131].

Normalized x-ray powder diffraction patterns (Fig.5.7) show an unequal evolution of the lattice parameters with doping, as can be seen e. g. from the shift of the (2 0 0) reflex around 46° to smaller 2Θ values or the shift of the (0 0 2) reflex around 15° to larger 2Θ values.

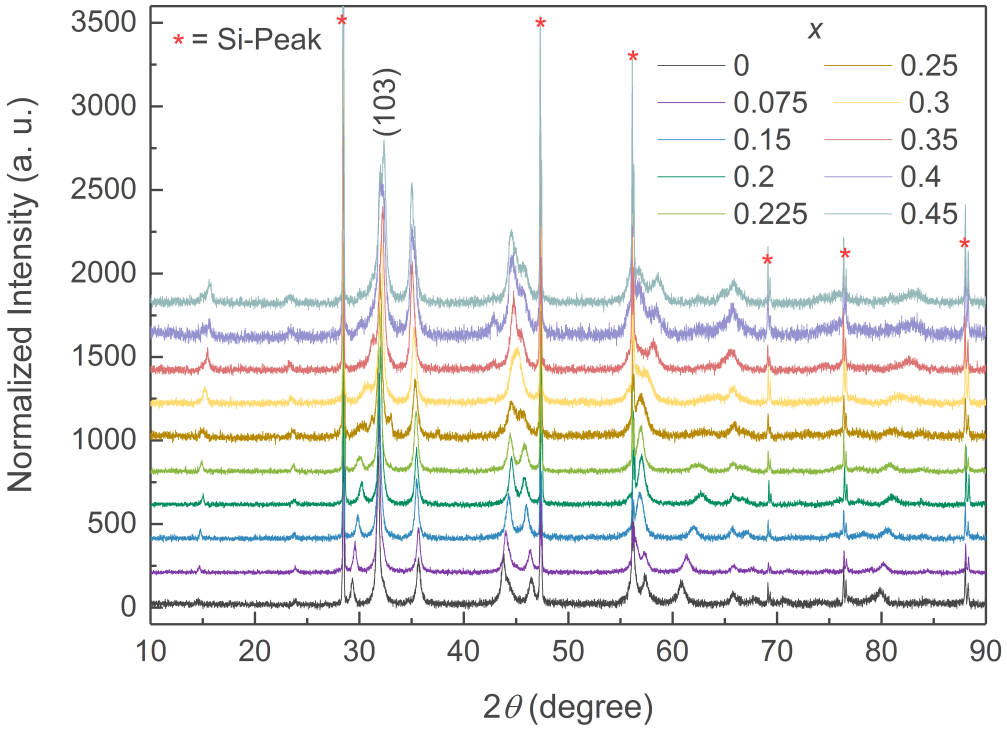


FIGURE 5.7: X-ray powder diffraction patterns of $Eu(Fe_{1-x}Ru_x)_2As_2$ for various $x$. The data are normalized to the (103)-reflection and vertically shifted by 200 counts for clarity starting from $x = 0$ at the bottom upwards. Red stars indicate Si reference peaks.

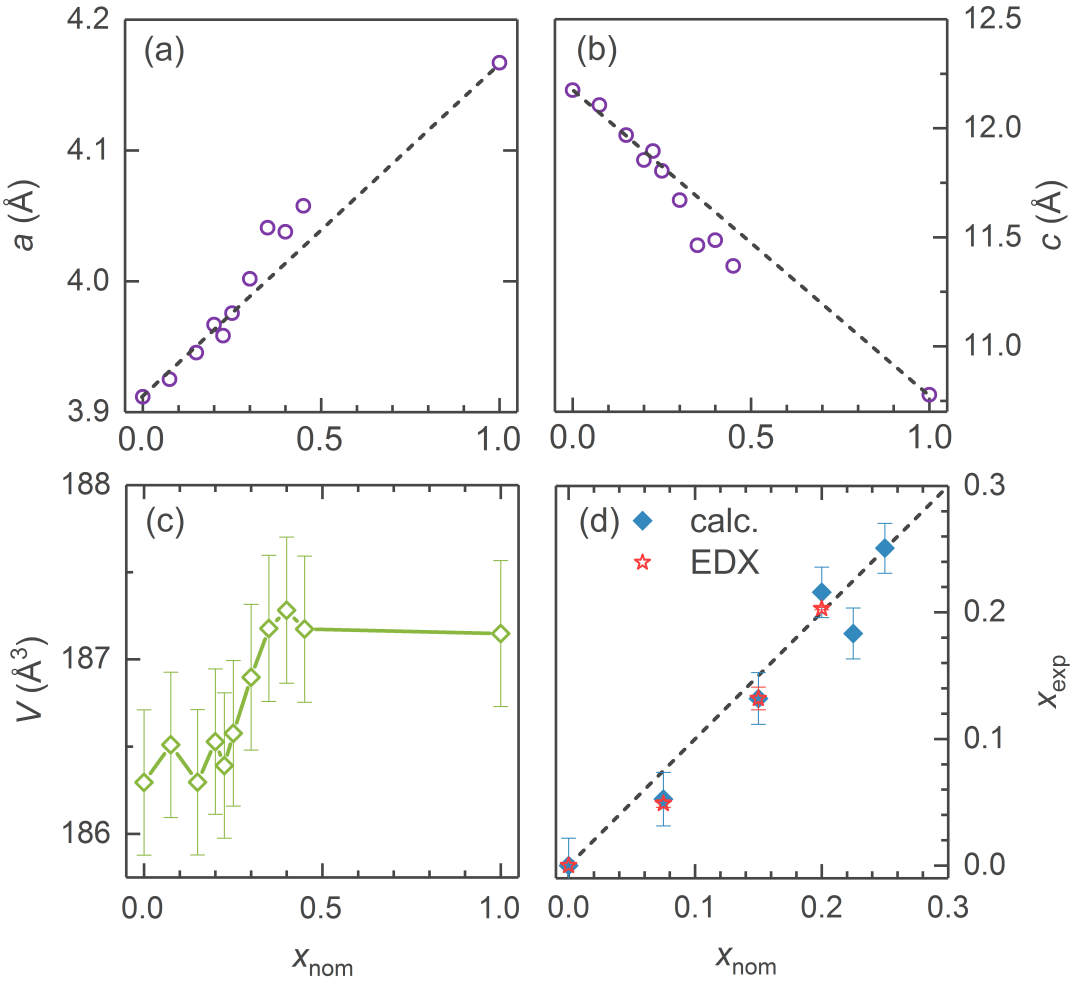


FIGURE 5.8: Lattice parameters and doping levels of $Eu(Fe_{1-x}Ru_x)_2As_2$ as a function of $x$ extracted from XRD data. Refined room-temperature values for the (a) $a$-axis, (b) $c$-axis, and (c) unit cell volume. (d) Experimental Ru concentration $x_{exp}$ against nominal concentration $x_{nom}$ calculated using Vegard's law ($a$-axis). Red stars represent EDX data for comparison, while the dashed lines are guides to the eye. If not visible, error bars are within the symbols size. Data for $x = 1$ are taken from Ref. [150].

This behavior is clearly reflected in the evolution of the refined lattice parameters (Fig. 5.8a+b). Initially both parameters vary linearly with doping. The $a$ parameter increases as expected for a larger substituent, but shows a positive deviation from Vegard's law around $x = 0.35$, while the $c$ parameter decreases with doping and exhibits a negative deviation from the linear progression. Over the entire doping range, the $c$-axis decreases by approximately 13 %, while the $a$-axis increases by roughly 7 %. As a consequence, the unit cell volume (Fig. 5.8c) stays almost constant, increasing only by 0.5 % in a step-like fashion around $x = 0.35$.

The decrease in $c$ and, correspondingly, in $c/a$ with increasing $x$ was also observed in other Ru-doped 122-compounds, like $Ba(Fe_{1-x}Ru_x)_2As_2$ and $Ca(Fe_{1-x}Ru_x)_2As_2$ [151, 152]. While the decrease observed in $EuFe_2As_2$ is larger than in the Ba-compound, it

is much smaller than in the Ca-system, where it was interpreted in terms of a collapsed tetragonal phase, which can also be achieved in the parent compound by applying pressure [153, 154].

Due to this non-linear evolution of the lattice parameters, Vegard's law can not be used for the determination of $x$ above $x \approx 0.3$. However, the main goal of this thesis is the investigation of the magnetically induced detwinning effect in the Eu-based systems. In the case of Ru-doping, this restricts us to small $x$ below $x \approx 0.2$, because higher doping levels lead to a suppression of the structural transition, leaving the system tetragonal down to the lowest temperatures, as we will see below.

Limiting the analysis to $x \leq 0.3$, we find that the experimentally determined composition from Vegard's law $x_{\mathrm{exp}}$ seems to be in good agreement with the nominal composition $x_{\mathrm{nom}}$. However, as evidenced by additional EDX data (Fig.5.8d), $x_{\mathrm{exp}}$ deviates for $x = 0.2$.

Various Laue diffraction patterns of a $Eu(Fe_{1-x}Ru_x)_2As_2$ crystal with $x = 0.35$ recorded at room temperature (Fig. 5.9c) show sharp reflections, indicating a high structural quality of the crystal. The fourfold symmetry of the tetragonal crystal structure is clearly evident. Furthermore, the scans reveal that the sample is grown homogeneously and confirm the structural quality throughout the entire sample surface. The diffuse background is slightly enhanced compared to the undoped sample (Fig. 5.9a). This can likely be attributed to the disorder introduced by the dopant. Note that the patterns were always recorded on as-grown crystals and the surfaces were not polished or otherwise prepared prior to measurement. Therefore, the marginally blurry reflections, e. g. in the (0,1)-grid picture, are likely due to surface irregularities of the crystal. The crystal is shown in Fig. 5.9d, together with the respective beam spots, which are not to scale. The dimensions of the crystal is noteworthy: with a diameter of 8 mm its size was only limited by the diameter of the growth crucible.

The metallic regime of the in-plane electrical resistivity observed at high temperatures extends to lower temperatures with increasing Ru-content (Fig. 5.10a), due to the continuous suppression of $T_{\mathrm{Fe}}$. Around $x = 0.2$ the signature of the structural and SDW order is virtually gone and the onset of superconductivity is visible, although zero resistance is not yet obtained. At $x = 0.225$ the resistance drops to zero below a critical temperature $T_{\mathrm{c}}$ of 24.3 K. The onset of SC with approximately 26 K is significantly higher than the $T_{\mathrm{c}}$ onset of 22 K reported for $x = 0.21$ [131]. In contrast to the report in Ref. [131], zero-resistance SC is not observed for any other composition. This might be related to the fact that the presented crystals were not annealed—except for $x = 0.15$ and $x = 0.225$, see Appendix. The results are summarized in a preliminary phase-diagram (Fig. 5.10a)

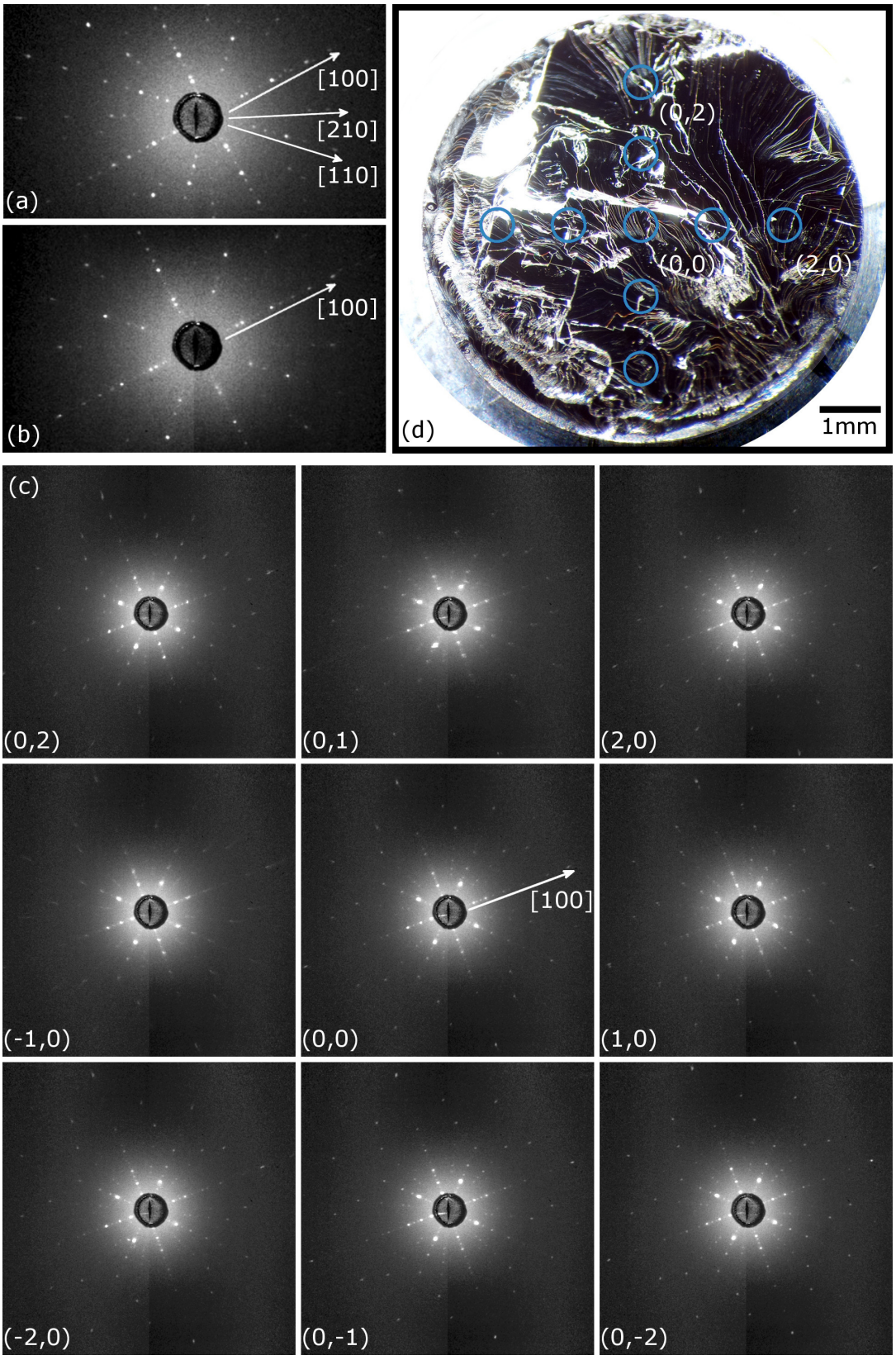


FIGURE 5.9: Laue diffraction patterns of Eu-based iron pnictides recorded at room temperature. (a) $EuFe_2As_2$, (b) $Eu_{1-x}Ba_xFe_2As_2$ ($x = 0.5$), and (c) $Eu(Fe_{1-x}Ru_x)_2As_2$ ($x = 0.35$). The grid-panel shows scans over several spots on the crystal depicted in (d). Coordinates indicate the respective positions (blue circles, not to scale!) on the sample. Arrows indicate selected crystallographic directions in tetragonal notaion.

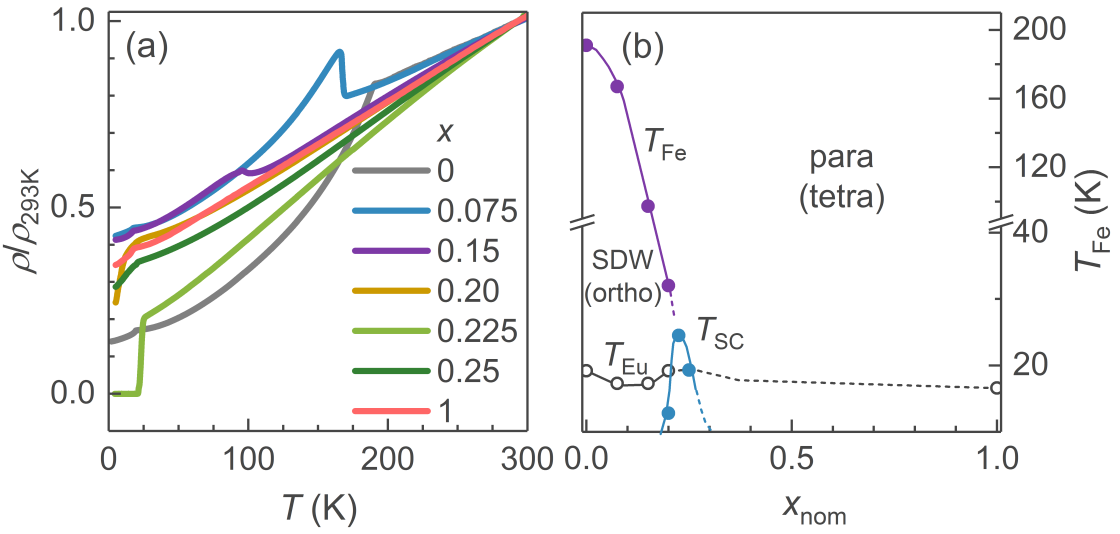


FIGURE 5.10: Electrical transport of $Eu(Fe_{1-x}Ru_x)_2As_2$. (a) In-plane resistivity as a function of temperature for some selected Ru concentrations $x_{nom}$. (b) Derived phase diagram. $T_{SC}$ denotes the onset of superconductivity. All lines are guides to the eye. Data for $x = 1$ are taken from Ref. [155].

derived from the transport data. The transition temperature of the $Eu^{2+}$ moments $T_{Eu}$ is barely affected by doping, in agreement with Ref. [131].

## 5.4 Summary

Single crystals of the undoped parent compound $EuFe_2As_2$ and the magnetically diluted systems $Eu_{1-x}Ba_xFe_2As_2$ and $Eu(Fe_{1-x}Ru_x)_2As_2$ were successfully synthesized by the methods described in Chapter 3. The samples are of very good quality, compared to typical 122-type iron pnictides, as evidenced by XRD, Laue, and electrical transport data. A sample dependence of the transport data was observed, which, however, is not critical to the following discussion.

The $Eu_{1-x}Ba_xFe_2As_2$ system appears to be a simple solid solution, with indications of spin-glassy behavior of the $Eu^{2+}$ moments at low temperatures and for large Ba concentrations. All lattice parameters and the unit cell volume increase basically linearly upon doping, as expected for a larger dopant. The structural and coincident electronic transition temperature $T_{Fe}$ decreases overall linearly from 190 K to roughly 140 K for pure $BaFe_2As_2$.

The Ru substitution on the Fe site exhibits a more complex behavior. In particular, the influence on the lattice parameters is much more pronounced than in the case of $Eu_{1-x}Ba_xFe_2As_2$. A deviation from Vegard's law was observed for $x_{nom} \geq 0.3$. The

reduction of the $c$ parameter indicates a chemical pressure effect similar to, but less pronounced than for P-doping on the As site [124]. The reduction of the $c$-axis in P-doped samples coincides with significant electronic changes as revealed e. g. by ARPES studies [105, 115, and references therein]. Similar changes could also explain the properties of Ru-doped samples, but further investigations are needed to draw reliable conclusions. Furthermore, Ru-doping reduces $T_{\mathrm{Fe}}$ and leads to superconductivity once $T_{\mathrm{Fe}}$ is suppressed. The ordering temperature of the $Eu^{2+}$ moments was found to be only marginally affected by the Ru content. Except for the $Eu^{2+}$ ordering, the derived phase diagram is qualitatively equivalent to the generic phase diagram of the iron pnictides discussed in Chapter 4.

In conclusion, the grown single crystals are fully suited for the investigation of the multistage magnetic detwinning effect in the Eu-based iron pnictides, which is discussed in the next two chapters.

Chapter 6

# Magnetic Detwinning in $EuFe_2As_2$

This chapter presents the findings of the investigation into the unusual domain dynamics discovered at low temperatures in $EuFe_2As_2$ upon application of small in-plane magnetic fields. It combines a novel microscopic theory with first-principles numerical calculations and experimental evidence, both supporting the theory.

The chapter is divided into three major parts: The first one presents the new microscopic theory that can fully and quantitatively explain the field-dependent low-temperature phase diagram of $EuFe_2As_2$ in its full richness and complexity. The key ingredient of this novel theory is a relatively small biquadratic coupling between Fe and Eu, which, however, has a tremendous effect on the field-induced domain dynamics. The second part presents the experimental evidence for this *multistage magnetic detwinning effect*. It starts by discussing strong signatures in dilatometric, transport, and neutron diffraction data, followed by more subtle signatures in the magnetization data. Finally, the third part pertains to the analysis of the experimental data using the new theory. The coupling constants of the interlayer exchange $J_\perp$ of the Eu subsystem and the biquadratic exchange $K$ between Fe and Eu, as well as the energy barrier $\Delta$ associated with the reorientation of structural domains, will be determined in this section.

The investigation of $EuFe_2As_2$ presented in this chapter was a collaborative effort. I developed the microscopic theory together with I. I. Mazin from the Material's Science and Technology Division of the Naval Research Laboratory in Washington and conducted the neutron diffraction measurements together with S. Nandi from the Indian Research Laboratory in Kanpur and Y. Xiao from the Forschungszentrum Jülich. The thermal expansion and magnetostriction data of the undoped compound were recorded by C. Stingl and N. Bach from the former group of P. Gegenwart at the University of Göttingen. Contributions from collaborators are acknowledged in the appropriate places.

Some of the experimental data presented in this chapter, together with an early phenomenological model of the magnetic detwinning effect in $EuFe_2As_2$, have already been published in collaboration with Sina Zapf and Martin Dressel from the University of Stuttgart in *Physical Review Letters* [156], while a manuscript presenting the microscopic theory has been submitted to *Physical Review X* for publication and is available on arXiv [157].

## 6.1 Introduction

The parent compounds of the IBSCs form an unusual symmetry-breaking antiferromagnetic (AF) ground state at low temperatures, which is occasionally succeeded by an even more unusual electronic nematic state. Insight into this electronic nematicity and the associated large in-plane anisotropy is believed to be crucial for the understanding of the physics of the IBSCs [38, 55, 158–164]. However, the formation of structural $\mu$m-sized twin domains in this phase impedes the investigation, since measurements that probe these materials over dimensions larger than the expanse of the twin domains cannot resolve the anisotropy (see also Chapter 2). In order to uncover and study the anisotropy and, consequently, the nematic state, these materials need to be forced into a detwinned, i. e. mono-domain state. This is typically achieved by the application of uni-axial pressure through a mechanical clamp [158, 159, 165]. However, this mechanical detwinning is cumbersome to implement, because, in contrast to the copper-oxide superconductors, it needs to be implemented in a cryogenic environment. More importantly, mechanical detwinning reportedly alters physical properties of the investigated samples [163]. This is because the uni-axial pressure acts as an external symmetry-breaking force to the sample and must, therefore, be expected to introduce additional extrinsic anisotropy. Consequently, results obtained through mechanical straining need to be considered very carefully. This is particularly true for the investigation of electronic nematicity, because the intrinsic nematic response can only be measured in the limit of zero external symmetry-breaking force [162].

An alternative to mechanical clamping is the application of in-plane magnetic fields. By utilizing magneto-elastic coupling between the Fe moments and the lattice, it is possible to partially detwin IBSCs. Unfortunately, the observed magnetic detwinning effect is rather small. The magnitude of the magnetoresistance of $Ba(Fe_{1-x}Co_x)_2As_2$, for instance, is only a few percent at a large field of $\sim 15\,\mathrm{T}$ [166]. Considering that the estimated in-plane anisotropy of the electrical resistivity $\rho_b/\rho_a$ in this compound is of the order of 2 [165, see also Chap. 4] this indicates a very small detwinning fraction. Near complete detwinning can, however, only be achieved in large pulsed fields of the

order of $\sim 30\,\mathrm{T}$ [167], which are not widely available. Thus mechanical straining remains the generally preferred detwinning option.

The report that a small in-plane magnetic field of less than 1 T influences the twin distribution in $EuFe_2As_2$ [168] was, therefore, unexpected and triggered the systematic investigation of this effect presented here. In the following, we will see that the reasons for this drastically reduced detwinning field in $EuFe_2As_2$ are the additional magnetic moments stemming from the $Eu^{2+}$ ions (see also Sec. 4.7) and their intricate interplay with the Fe subsystem.

## 6.2 Theoretical Description

This section is dedicated to the theoretical description of the multistage magnetic detwinning in $EuFe_2As_2$. A novel microscopic theory, based on a biquadratic coupling $K$ between the Eu-4$f$ and Fe-3$d$ moments is presented. The biquadratic coupling allows for a comprehensive description of the low-temperature field-dependent phase diagram of $EuFe_2As_2$.

### 6.2.1 Hamiltonian

It is well established that a minimum microscopic model of the Fe magnetism in IBSCs includes Heisenberg terms up to the third neighbors and a sizable nearest-neighbor (n.n) biquadratic coupling [169]. However, for our purposes of calculating the energy gain due to the Fe spin canting in an external magnetic field, it is not necessary to go that far. Therefore, we absorb these parameters into a single one, $\tilde{J}$, and use a minimal approximation of the n.n. Heisenberg model with a single-ion anisotropy $\tilde{D}$ to describe the Fe subsystem:

$$\mathcal{H}_{\mathrm{Fe}} = \underbrace{-\tilde{D}\sum_i f_{i,x}^2}_{\substack{\text{Single-ion}\\ \text{anisotropy}}} + \underbrace{\tilde{J}\sum_{\langle ij\rangle} \mathbf{f}_i \cdot \mathbf{f}_j}_{\substack{\text{Heisenberg}\\ \text{exchange}}} + \underbrace{\tilde{M}\sum_i \mathbf{f}_i \cdot \mathbf{H}}_{\text{Zeeman}}, \tag{6.1}$$

where $i, j$ label Fe sites, $\mathbf{f}_i$ is the unit vector directed along the Fe magnetic moment at site $i$, $\tilde{M}$ is its absolute value, $\tilde{J}$ the AF Heisenberg exchange constant, the summation is over all inequivalent n.n bonds, and $x$ denotes the magnetic easy axis, which is $a$ in the following. The external field in corresponding energy units is given by $\mathbf{H}$. Here and below, tildes over symbols refer to Fe related parameters. From neutron diffraction studies it is known that the Fe moments order with the magnetic propagation vector $\mathbf{k} = (1, 0, 1)$ within the $ab$-plane, oriented along the longer $a$-axis ($\tilde{D} > 0$, Fig. 6.1)

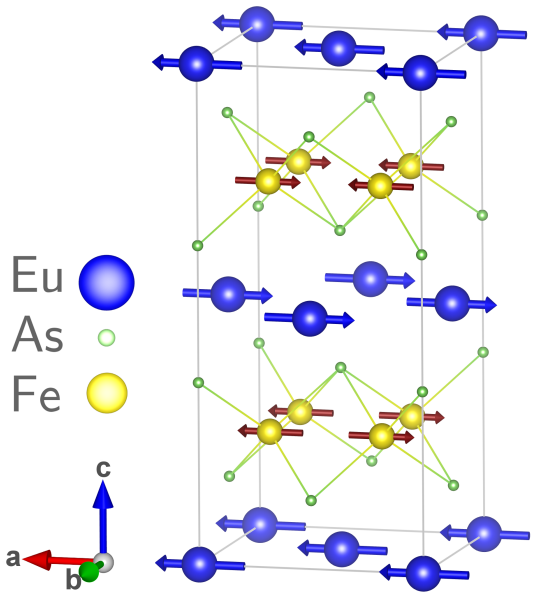


FIGURE 6.1: Illustration of the low-temperature magnetic structure of $EuFe_2As_2$. The typical stripe order of the Fe spins (red arrows) of the iron pnictides can be seen along the $b$-axis. The $Eu^{2+}$ moments order in an A-type AF structure with FM in-plane order. The crystallographic $a$-axis is the magnetic easy-axis in this system.

[170]. The above parameters have been estimated to $\tilde{J} \sim 30\,\text{meV}$, $\tilde{D} \approx 0.25\,\text{meV}$, and $\tilde{M} \approx 1\,\mu_\text{B}$ [106, 171], which we will use in the following. The interactions *inside* the Eu sublattice can be described by

$$\mathcal{H}_\text{Eu} = \underbrace{J_\parallel \sum_{\langle ij \rangle} \mathbf{e}_i \cdot \mathbf{e}_j}_{\substack{\text{In-plane} \\ \text{exchange}}} + \underbrace{J_\perp \sum_i \mathbf{e}_i \cdot \mathbf{e}_{i^+}}_{\substack{\text{Out-of-plane} \\ \text{exchange}}} + \underbrace{M \sum_i \mathbf{e}_i \cdot \mathbf{H}}_{\text{Zeeman}} \tag{6.2}$$

where $i, j$ now label Eu sites, $i^+$ the respective Eu site in the next layer, $\mathbf{e}_i$ the unit vectors directed along the Eu magnetic moment $M$ at site $i$, and the ferromagnetic $J_\parallel < 0$ and antiferromagnetic $J_\perp > 0$ exchange constants. The latter two determine the in-plane and out-of-plane ordering. Note that no single-ion anisotropy is included in Eq. (6.2). This is because Eu adopts a valence state of +2 in $EuFe_2As_2$. $Eu^{2+}$ has a half-filled $f$-shell and thus no angular momentum and negligible magnetocrystalline anisotropy. In other words, it is a large spin-only moment with $S = 7/2$ and $L = 0$. This is confirmed by our first principles calculations presented in Appendix B.

It is not sufficient to describe the interaction *between* Fe and Eu atoms in a simple Heisenberg picture, because the Eu projection sits in the center of the Fe-square plaquette and the Heisenberg exchange field induced by the Fe atoms on the Eu sites cancels by symmetry (and so is even the dipole field). Without an interaction between Fe and Eu sublattices, there is no physical mechanism by which the Eu spins may affect the

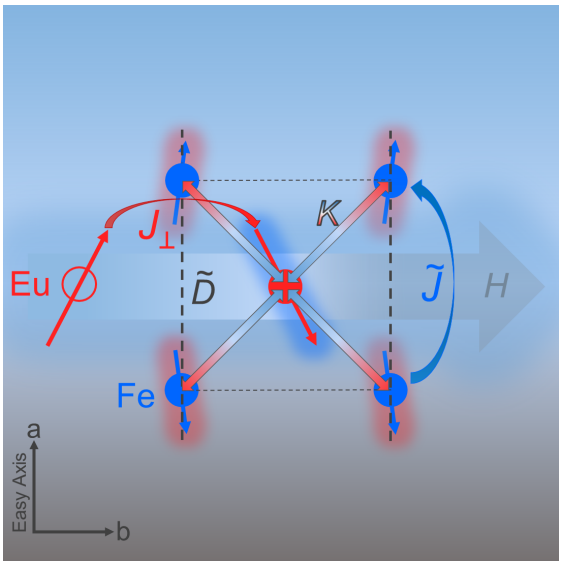


FIGURE 6.2: Illustration of the Hamiltonian Eq. (6.3). The single-ion anisotropy $\tilde{D}$ aligns the Fe moments (blue) along $a$, while the AF exchange energies $\tilde{J}$ (blue curved arrow) and $J_\perp$ (red curved arrow) favor the AF arrangement of Fe and $Eu^{2+}$ moments (red), respectively. The open circle depicts Eu in the next layer. The biquadratic coupling $K$ (blue-red colored arrows and colored haze around the spins) is the means by which the $Eu^{2+}$ moments can couple indirectly to the lattice via the Fe moments. The Zeeman terms model the external magnetic field $H$ (white-gray arrrow), leading to a canting of the moments, here shown for the b-twin domain, i. e. $H \parallel b$ configuration.

detwinning and could lead to the drastically reduced detwinning field in $EuFe_2As_2$ [156, 168].

It is well known that the IBSCs feature a considerable biquadratic coupling between the Fe atoms, which plays a crucial role in their nematic behavior [24]. In the following, we assume the existence of such a biquadratic interaction between the Fe and Eu layers, which allows for a physically meaningful description of the observed detwinning effect. Therefore, we combine Eq. (6.2) and Eq. (6.1) in the following way:

$$\begin{aligned}\mathcal{H} = &+ \tilde{M}\sum_{\alpha}\mathbf{f}_\alpha\cdot\mathbf{H} + \tilde{J}\sum_{\langle\alpha\beta\rangle}\mathbf{f}_\alpha\cdot\mathbf{f}_\beta - \tilde{D}\sum_{\alpha}f_{\alpha,x}^2 \\ &+ M\sum_{i}\mathbf{e}_i\cdot\mathbf{H} + J_\perp\sum_{i}\mathbf{e}_i\cdot\mathbf{e}_{i^+} \\ &- K\sum_{\alpha,n}\left(\mathbf{f}_\alpha\cdot\mathbf{e}_{\alpha+n}\right)^2,\end{aligned} \tag{6.3}$$

where the Greek subscripts label the Fe sites, Latin the Eu sites, $K$ the biquadratic coupling term, and the last summation runs over all n.n Fe-Eu pairs, i. e. $n = 1...4$ (see also Fig. 6.2). In $EuFe_2As_2$, there is one AF in-plane Fe-Fe bond and four out-of-plane Eu-Eu bonds. However, we will only consider one effective bond, as if the Eu layers were stacked directly on top of each other. The biquadratic coupling is defined

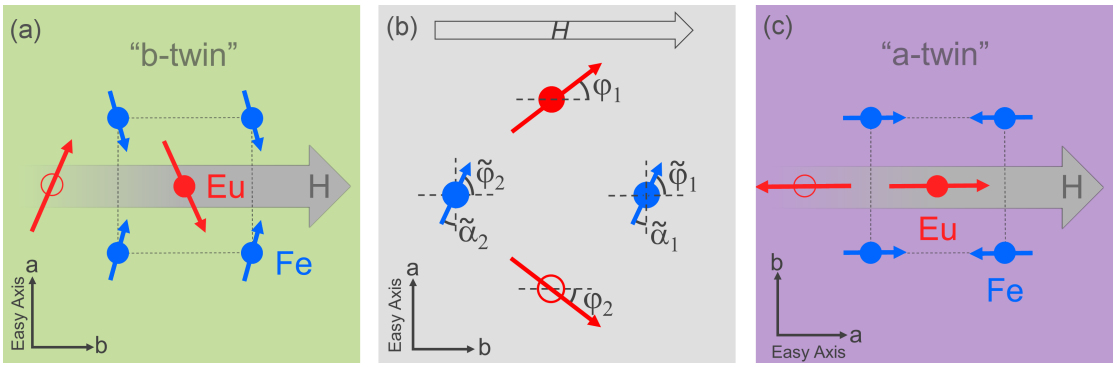


FIGURE 6.3: Illustration of the twin domains and angles. Depicted is part of the low-$T$ basal plane of $EuFe_2As_2$, with Fe spins and atoms (blue), Eu spins and atoms (red), while open circles indicate Eu atoms in the next layer. The magnetic field $H$ enters from the left. (a) Definition of the "b-twin" domain along the field direction, i. e. $H \parallel b$. (b) Angles of the Eu spins $\varphi_i$ and Fe spins $\tilde{\varphi}_i$ are defined with respect to the magnetic field $H$, while $\tilde{\alpha}_i$ denotes the angle of the Fe spins to the magnetic easy axis. (c) Definition of the "a-twin" domain along the field direction, i. e. $H \parallel a$.

in accordance with the exchange term, such that $K$ is given per bond. Our band-structure calculations (Appendix B) estimate the biquadratic Eu-Fe coupling term to $K \sim 0.4\,\mathrm{meV}$. Considering the uncertainty in the underlying approximations, this can be taken as indication that $K$ is not negligible. Later in this chapter we will also determine the actual magnitude of $K$ from the experiment.

### 6.2.2 Individual Twin Domains

Before I discuss the detwinning process of $EuFe_2As_2$, we will first investigate the individual twin domains separately in order to derive their field-dependent domain energies. This will allow us to determine the energy difference between the domains, i. e. the energy cost/gain of any reorientation and derive the *equilibrium* phase diagram.

Although the IBSCs exhibit four twin domain types in the orthorhombic phase [159], only two effective perpendicular domains need to be discussed, because the in-plane lattice vectors of each two domains types in the pairs (O1,O3) and (O2,O4) are collinear, as discussed in Chapter 2. Therefore, the following description is analogous within each pair.

We define the two domains by the direction of the respective lattice parameter to the considered direction, typically the "measurement direction". Therefore, the *b-twin* domain refers to the twin with the shorter $b$-axis along the considered direction, while the *a-twin* consequently denotes the twin with the longer $a$-axis along the same direction. If not stated otherwise, this direction coincides with the direction of the applied magnetic field, or previously applied magnetic field (Fig. 6.3).

The orientation of the Eu and Fe spins is characterized by their respective angles $\varphi$ and $\tilde{\varphi}$ with respect to the external magnetic field, while $\tilde{\alpha}_i$, denotes the angle of the Fe spins with the easy $a$-axis. Considering that there are eight n.n Fe-Eu bonds and twice as many Fe as Eu (Fig. 6.1), we can rewrite Eq. (6.3) in terms of these angles (per one formula unit) as

$$\begin{aligned} E = &- \tilde{M}H(\cos\tilde{\varphi}_1 + \cos\tilde{\varphi}_2) + 2\tilde{J}\cos(\tilde{\varphi}_2+\tilde{\varphi}_1) - \tilde{D}(\cos^2\tilde{\alpha}_1 + \cos^2\tilde{\alpha}_2) \\ &- MH(\cos\varphi_1 + \cos\varphi_2)/2 + J_\perp\cos(\varphi_2+\varphi_1) \\ &- 2K[\cos^2(\varphi_2-\tilde{\varphi}_2) + \cos^2(\varphi_2-\tilde{\varphi}_1) + \cos^2(\varphi_1-\tilde{\varphi}_2) + \cos^2(\varphi_1-\tilde{\varphi}_1)]. \end{aligned} \tag{6.4}$$

Starting from Eq. (6.4), I will first discuss the simpler b-twin ($H \parallel b$, where $b$ is the hard axis), and then the a-twin, in all field regimes. Two different regimes are considered separately: small and large fields. These are distinguished with respect to the field at which magnetic detwinning occurs in systems like $BaFe_2As_2$ ($\approx 30\,\mathrm{T}$), which will be called $H_2$ in the following. Thus at small fields below $H_2$ the canting of Fe moments can be safely neglected ($\tilde{J} \sim 30\,\mathrm{meV}$). As mentioned in Chapter 4, a metamagnetic transition to a FM state of the Eu moments can be induced by small magnetic fields of the order of 1 T, therefore, at large fields comparable to or larger than $H_2$, the Eu magnetization will already be saturated ($\varphi_1 = \varphi_2 = 0$).

#### 6.2.2.1 $b$-Domain: $H \parallel b$

**Small fields**

In this case, the external field is applied along the crystallographic $b$-axis. For small fields the Fe moments are locked in the ground-state configuration $\tilde{\varphi}_2 = \tilde{\varphi}_1 = \pi/2$, $\tilde{\alpha}_2 = \tilde{\alpha}_1 = 0$ and for Eu we have the boundary condition: $\varphi = \varphi_1 = \varphi_2$. Inserted into Eq. (6.4) this leads to:

$$\begin{aligned} E_b &= - MH\cos\varphi + J_\perp\cos 2\varphi - 8K\sin^2\varphi - 2\tilde{J} - 2\tilde{D} \\ &= - MHf + (2J_\perp + 8K)f^2 + E_0, \end{aligned} \tag{6.5}$$

with $f = \cos\varphi$ and the ground state energy $E_0 = -2\tilde{J} - 2\tilde{D} - J_\perp - 8K$. After minimizing this equation with respect to $f$ we get for $MH < 4(J_\perp + 4K)$:

$$f_b^{\min} = \frac{MH}{4J_\perp + 16K} \tag{6.6}$$

and the equilibrium energy

$$E_b^{\min} = -\frac{M^2H^2}{8(J_\perp + 4K)} + E_0. \tag{6.7}$$

Thus, we find that the energy is always below $E_0$ for sufficiently small fields, as the Eu moments continuously screen the field and reduce their Zeeman energy. The equilibrium tilting angle changes gradually according to $\varphi_b^{\min} = \cos^{-1}[MH/(4J_\perp + 16K)]$. Above $H_{\mathrm{b}}^{\mathrm{sat}} = (4J_\perp + 16K)/M$ (derived from $f_b^{\min} = 1$), the Eu moments are fully saturated in field direction and the energy changes to

$$E_b^{sat} = -MH + 2J_\perp + 8K + E_0. \tag{6.8}$$

**Large fields**

At higher fields, the Fe moments will eventually start to deflect ($\tilde{\alpha} = \pi/2 - \tilde{\varphi}$) from the easy axis, while the $Eu^{2+}$ moments are already saturated. Therefore, Eq.(6.4) leads to

$$\begin{aligned}\tilde{E}_b =& -2\tilde{M}H\cos\tilde{\varphi} + 2\tilde{J}\cos 2\tilde{\varphi} - 2\tilde{D}\sin^2\tilde{\varphi} - 8K\cos^2\tilde{\varphi} - MH + J_\perp \\ =& -2\tilde{M}H\tilde{f} + 2(2\tilde{J} + \tilde{D} - 4K)\tilde{f}^2 - MH + E_0 + 2J_\perp + 8K,\end{aligned}$$

where $\tilde{f} = \cos\tilde{\varphi}$. The equilibrium energy is now calculated by minimizing with respect to $\tilde{f}$, which yields via

$$\tilde{f}_b^{\min} = \frac{\tilde{M}H}{4\tilde{J} + 2\tilde{D} - 8K}$$

to Eq. (6.8) with an additional term stemming from the canting of the Fe moments away from the easy axis

$$\tilde{E}_b^{\min} = -MH + 2J_\perp + 8K - \frac{(\tilde{M}H)^2}{4\tilde{J} + 2\tilde{D} - 8K} + E_0.$$

At even higher fields, after the saturation of the Fe moments at $\tilde{H}_b^{sat} = (4\tilde{J} + 2\tilde{D} - 8K)/\tilde{M}$, the equilibrium energy will further evolve as

$$\tilde{E}_b^{\mathrm{sat}} = -MH + 2J_\perp - 2\tilde{M}H + 4\tilde{J} + 2\tilde{D} + E_0.$$

#### 6.2.2.2 *a*-Domain: $H \parallel a$

In order to discuss the a-twin, we now rotate the field by $\pi/2$ and apply it along the $a$-axis.

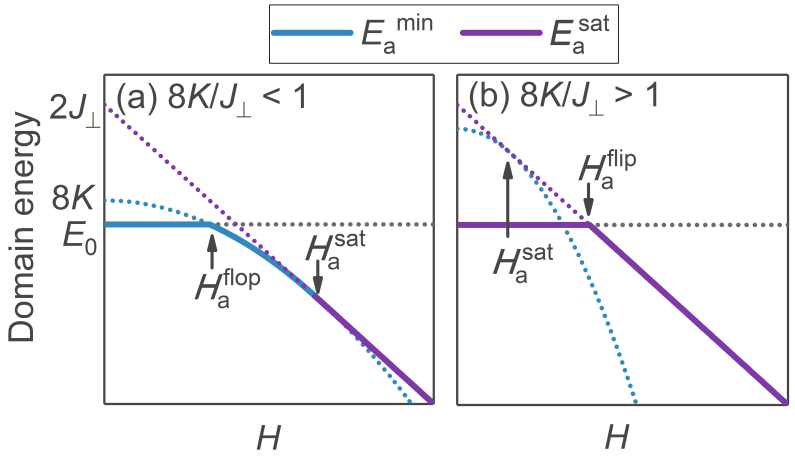


FIGURE 6.4: Generic field dependence of the a-twin domain for (a) the spin-flop and (b) the spin-flip case. Solid lines represent the equilibrium energy, while dotted lines represent regions in which the respective solutions are out of range.

### 1. Small fields

At small fields the Fe moments are again considered to be locked into the ground state configuration and we have the following conditions: $\tilde{\alpha}_1 = \tilde{\varphi}_1 = 0$, $\tilde{\alpha}_2 = \tilde{\varphi}_2 = \pi$ and $\varphi = \varphi_1 = \varphi_2$, leading to

$$\begin{aligned} E_a &= -MH\cos\varphi + J_\perp \cos 2\varphi - 8K\cos^2\varphi - 2\tilde{J} - 2\tilde{D} \\ &= -MHf + (2J_\perp - 8K)f^2 + 8K + E_0, \end{aligned} \tag{6.9}$$

again with $f = \cos\varphi$ and $E_0$. Minimizing Eq. (6.9) with respect to $f$, leads for $MH < 4J_\perp - 16K$ and $J_\perp > 4K$ to

$$f_a^{\min} = \frac{MH}{4J_\perp - 16K},$$

and after reinsertion into Eq. (6.9) to the energy of the $a$ domain:

$$E_a^{\min} = -\frac{M^2H^2}{8(J_\perp - 4K)} + 8K + E_0. \tag{6.10}$$

Note the sign change in the denominator and the additional $8K$-term compared to Eq. (6.7). Due to this $8K$-term Eq.(6.10) is initially above $E_0$ and becomes only populated at $H_a^{\text{flop}} = 8/M\sqrt{K(J_\perp - 4K)}$ ($E_a^{\min} = E_0$). At this field the $Eu^{2+}$ moments suddenly depart from their ground-state configuration and align roughly perpendicular to the easy $a$-axis. Therefore, we find a metamagnetic spin-flop transition, as introduced in Chapter 2, in which the biquadratic coupling ($8K$) takes the role of an effective magnetocrystalline anisotropy for the Eu subsystem.

With further increasing field, the $Eu^{2+}$ moments now gradually rotate towards saturation according to $\varphi_a^{\min} = \cos^{-1}[MH/(4J_\perp - 16K)]$. At $H_a^{\text{sat}} = (4J_\perp - 16K)/M$ saturation is

reached, and Eq. (6.10) changes to:

$$E_a^{\mathrm{sat}} = -MH + 2J_\perp + E_0,$$

as depicted in Fig. 6.4a.

If the biquadratic coupling $K$ is large compared to the out-of-plane coupling $J_\perp$, however, the $Eu^{2+}$ moments will flip from the ground-state configuration directly into the saturated state, skipping Eq. (6.10) entirely (Fig. 6.4a). This *spin-flip* transition occurs only if $E_a^{\mathrm{min}}(H_a^{\mathrm{sat}}) \geq E_a^{\mathrm{min}}(H_a^{\mathrm{flop}}) = E_0$, that is to say when $J_\perp \leq 8K$. The spin-flip field is given by

$$H_a^{\mathrm{flip}} = 2J_\perp/M. \tag{6.11}$$

### 2. Large fields

At high fields the Fe moments can also spin-flop (but not spin-flip, because $\tilde{J} \gg \tilde{D}$). However, the associated field is very large. Nonetheless, the effect can easily be incorporated for a full description of the detwinning effect by setting $\varphi = 0$ and $\tilde{\alpha} = \tilde{\varphi}$. Inserted into Eq. (6.4) this yields:

$$\begin{aligned}\tilde{E}_a =& -2\tilde{M}H\cos\tilde{\varphi} + 2\tilde{J}\cos 2\tilde{\varphi} - 2\tilde{D}\cos^2\tilde{\varphi} \\ & - 8K\cos^2\tilde{\varphi} - MH + J_\perp \\ =& -2\tilde{M}H\cdot\tilde{f} + 2(2\tilde{J} - \tilde{D} - 4K)\cdot\tilde{f}^2 \\ & - MH + 2J_\perp + 2\tilde{D} + 8K + E_0.\end{aligned} \tag{6.12}$$

with $\tilde{f} = \cos\tilde{\varphi}$. Minimizing Eq. (6.12) with respect to $\tilde{f}$ results in

$$\tilde{f}_a^{\mathrm{min}} = \frac{\tilde{M}H}{2(2\tilde{J} - \tilde{D} - 4K)},$$

and, consequently,

$$\tilde{E}_a^{\mathrm{min}} = -MH + 2J_\perp - \frac{(\tilde{M}H)^2}{2(2\tilde{J} - \tilde{D} - 4K)} + 2\tilde{D} + 8K + E_0. \tag{6.13}$$

The spin-flop field is calculated from the condition $\tilde{E}_a^{\mathrm{min}} - E_a^{\mathrm{sat}} = 0$, i. e. $\frac{(\tilde{M}H)^2}{4\tilde{J}-2\tilde{D}-8K} = 2\tilde{D} + 8K$, which yields

$$\tilde{H}_a^{\mathrm{flop}} = \frac{2}{\tilde{M}}\sqrt{(\tilde{D} + 4K)(2\tilde{J} - \tilde{D} - 4K)}.$$

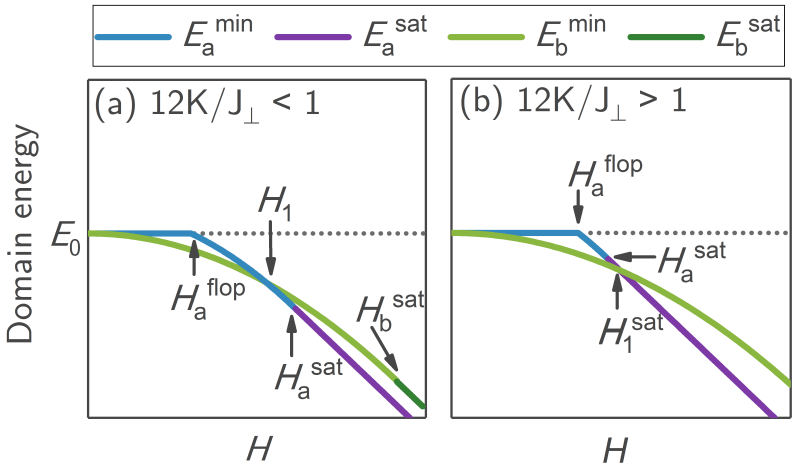


FIGURE 6.5: Generic field dependence of the energies of the a-twin and b-twin domain for characteristic ratios of $K/J_\perp$: (a) for $12K/J_\perp < 1$ and (b) $12K/J_\perp > 1$. The dashed line indicates the ground-state energy density $E_0$.

Upon saturation at $\tilde{H}_a^{\mathrm{sat}} = (4\tilde{J} - 2\tilde{D} - 8K)/\tilde{M}$ the energy changes to

$$\tilde{E}_a^{\mathrm{sat}} = -MH + 2J_\perp - 2\tilde{M}H + 4\tilde{J} + E_0.$$

Neglecting $K$ and higher orders of $\tilde{D}$ and using the above parameters $\tilde{J} \sim 30\,\mathrm{meV}$ and $\tilde{M} \approx 1\,\mu_\mathrm{B}$, we can estimate the spin-flop field of the Fe moments to $\tilde{H}_a^{\mathrm{flop}} \approx 2/\tilde{M}\sqrt{2\tilde{D}\tilde{J}} \approx 130\,\mathrm{T}$.

### 6.2.3 Full Detwinning Process

After deriving the energies of the individual twin domains, we can work out their combined equilibrium phase diagram. To this end, we assume that the system is always in the state (domain) with the lowest energy.

From the above deductions we can infer that the *b*-twin is energetically favored at small fields, where its energy is gradually reduced with increasing field, while the *a*-domain can, at least initially, not reduce its energy (Fig. 6.5). Consequently, the system will rearrange with $b \parallel H$.

Once the field energy exceeds the spin-flop field $H_a^{\mathrm{flop}}$ (or spin-flip field $H_a^{\mathrm{flip}}$, depending on the ratio $K/J_\perp$), the energy of the *a*-twin domain abruptly starts to decrease as well at a rate even higher than that of the *b*-twin, due to the sign change in the denominator of Eq. (6.10). This leads to a first crossing of the two energy curves, and, consequently, to another reorientation of domains from $b \parallel H$ to $a \parallel H$. Two cases need to be distinguished here: if $12K/J_\perp < 1$, $E_b$ will intersect with $E_a$ at $H_1$ (Fig. 6.5a), while for $12K/J_\perp > 1$, $E_a^{\mathrm{sat}}$ crosses $E_b$ at $H_1^{\mathrm{sat}} > H_a^{\mathrm{sat}}$ (Fig. 6.5b). Equating the corresponding

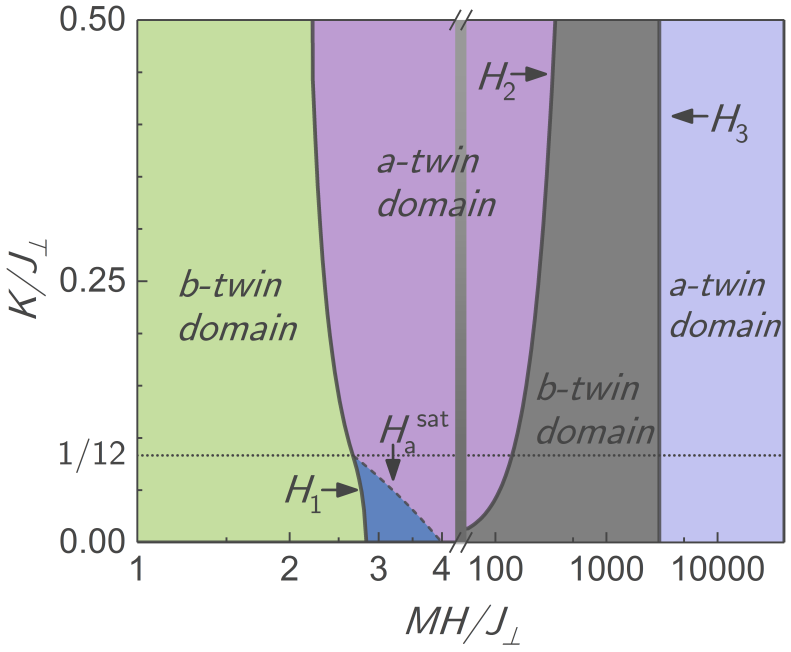


FIGURE 6.6: Phase diagram $K/J_\perp$ vs. $MH/J_\perp$ in thermodynamic equilibrium. Four phases emerge: The first (green) and third (gray) are characterized by canting of the Eu and Fe moments, while the second and fourth (light blue) are connected to metamagnetic transitions in the a-twin domains. In the second phase, saturated (violet) and unsaturated (blue) Eu moments are distinguished. The dotted line indicates the $12K/J_\perp = 1$ mark. The parameters $\tilde{J} \approx 300J_\perp$, $\tilde{D} \approx 2.5J_\perp$ and $\tilde{M}/M \approx 0.15$ are assumed.

energies, the first field can be expressed as

$$H_1 = \frac{2}{M}\sqrt{2(J_\perp^2 - 16K^2)}, \tag{6.14}$$

and the second one as

$$H_1^{\mathrm{sat}} = \frac{4}{M}(J_\perp + 4K) \cdot \left(1 - \sqrt{\frac{4K}{J_\perp + 4K}}\right). \tag{6.15}$$

Note that $H_1$ is always smaller than the saturation field $H_b^{\mathrm{sat}}$ of the $b$-twin.

At fields above $H_b^{\mathrm{sat}}$, where the energy difference is initially given by the biquadratic coupling $8K$, we enter the detwinning regime of the Fe moments. Once their energy gain due to canting ($\sim \tilde{M}H^2/4\tilde{J}$) becomes significant and exceeds $8K$ the domain energy curves intersect once again leading to a reversal of the domain orientation back to $b \parallel H$. The corresponding field is given by ($E_a^{\mathrm{sat}} \stackrel{!}{=} \tilde{E}_b$):

$$H_2 = \frac{4}{\tilde{M}}\sqrt{K(2\tilde{J} + \tilde{D} - 4K)} \approx \frac{4}{\tilde{M}}\sqrt{2K\tilde{J}}.$$

At the highest fields the Fe moments spin-flop and the energy of the $a$-twin starts to

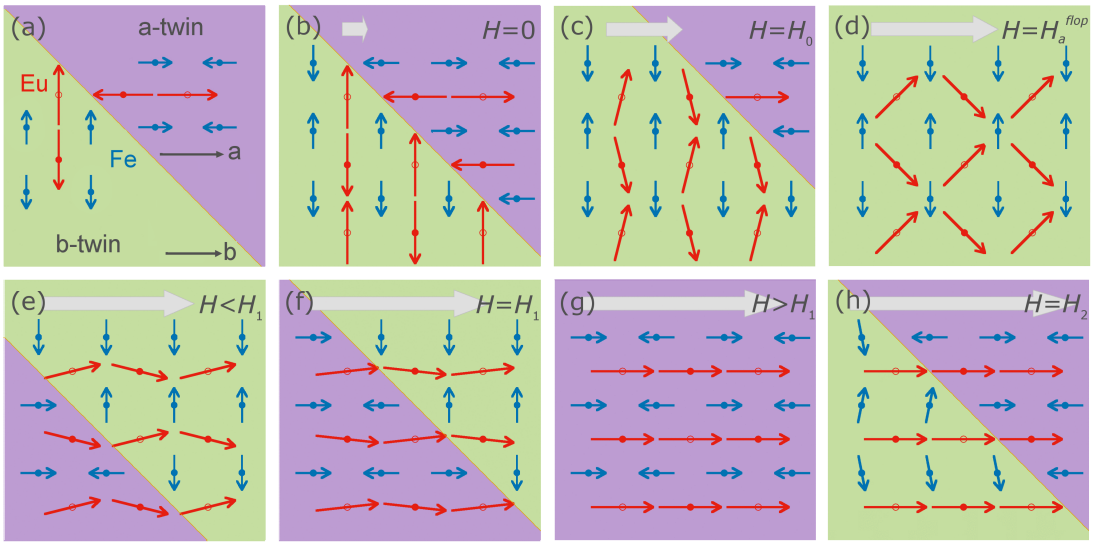


FIGURE 6.7: Illustration of the spin and domain dynamics of $EuFe_2As_2$ for an (from left to right, increasing) external magnetic field (gray arrow) $H \parallel [110]_T$. Fe atoms and spins are shown in blue, Eu in red. Open circles indicate Eu atoms and spins in the next layer. (a) Initial twin distribution with labels. (b) Initial twin distribution at $H = 0$. (c) The b-twins (green) grow with increasing field until (d) at $H_a^{\text{flop}}$ the system is completely detwinned with $b \parallel H$. (e) Above $H_a^{\text{flop}}$ the reorientation to a-twins (violet) sets in, (f) which is largest at $H_1$ and (g) completes above, with $a \parallel H$. (h) Around $H_2$ the second reorientation back to b-twin occurs. The final reorientation at $H_3$ back to a-twins is not shown.

significantly decrease again, similar to the situation in the Eu subsystem at lower fields. Above the third crossing of the energy regimes at $H_3$, the final detwinning with $a \parallel H$ sets in. The critical field is given by

$$H_3 = \frac{2}{\tilde{M}}\sqrt{2(\tilde{J}-2K)^2 - \frac{\tilde{D}^2}{2}} \approx \frac{2}{M}\sqrt{2}\tilde{J}.$$

The different phases in thermodynamic equilibrium are summarized in a $K/J_\perp$ vs. $MH/J_\perp$ phase diagram (Fig. 6.6). Four phases are theoretically predicted. The two b-twin ($b \parallel H$) phases correspond to the canting of Eu and Fe moments in the b-twin, while the two a-twin ($a \parallel H$) phases appear upon metamagnetic transitions of the respective moments.

The spin and domain dynamics are illustrated in Fig. 6.7. Furthermore, a movie clip accompanies this thesis. Initially (Fig. 6.7a+b) a-twin and b-twin domains are equally distributed. Upon increasing the field, $Eu^{2+}$ moments in the b-twin start canting, while the spin susceptibility of the a-twin is zero. The biquadratic exchange tries to minimize the angle between the Eu and Fe spins. Thus, if the angle of the $Eu^{2+}$ moments is $\pi/4 < \varphi < \pi/2$, the Fe spins orient perpendicular to the field ($\tilde{\varphi} = \pi/2$), i. e. $b \parallel H$, and the b-twins are lower in energy (Fig. 6.7c+d).

However, once[1] $\varphi < \pi/4$, it is more favorable for the Fe moments to align parallel to the field ($\tilde{\varphi} = 0$), and the first domain reorientation happens at $H_1$ (Fig. 6.7e-g). Finally, at $H_a^{\mathrm{sat}}$ (Fig. 6.7g) the differential spin susceptibility of the $Eu^{2+}$ moments becomes zero, as the Eu spins are aligned with the field ($\varphi = 0$), and further increase of the field does not change the total energy (aside from the Zeeman term $-MH$). Note that in this field regime only $\tilde{\varphi} = \pi/2$ or 0 is allowed, because any intermediate values are effectively forbidden by the strong Fe-Fe exchange and the Fe single-site anisotropy.

As long as the spin susceptibility of the Fe spins is zero, the Fe spins are parallel to the Eu spins and the biquadratic coupling is satisfied. However, at much higher fields the Fe moments can potentially gain energy by screening the field and around ($H \gtrsim H_2$) this energy gain outweighs the loss of the biquadratic coupling, leading to the second reorientation of domains back to the $b \parallel H$ configuration (Fig. 6.7h).

Theoretically, at even higher fields, it becomes favorable to reorient domains yet again to the $a \parallel H$ configuration, due to a spin-flop of the Fe moments and the energy gain from the biquadratic coupling (not shown in Fig. 6.7).

### 6.2.4 Domain Energy Difference

Now that the critical fields have been characterized and the domain dynamics are explained, the field-dependent domain energy difference $dE = E_{\text{a-twin}} - E_{\text{b-twin}}$ that drives the detwinning can be calculated quantitatively. It is a complicated piecewise function, and in the case of $12K/J_\perp < 1$ the segments up to $H_2$ read:

$$dE = \begin{cases} \frac{M^2H^2}{8(J_\perp+4K)}, & \{0, H_a^{\mathrm{flop}}\} \\ K(8 - \frac{M^2H^2}{J_\perp^2-8K^2}), & \{H_a^{\mathrm{flop}}, H_1\} \\ K(8 - \frac{M^2H^2}{J_\perp^2-8K^2}), & \{H_1, H_a^{\mathrm{sat}}\} \\ -MH + 2J_\perp + \frac{M^2H^2}{8(J_\perp+4K)}, & \{H_a^{\mathrm{sat}}, H_b^{\mathrm{sat}}\} \\ -8K + \frac{\tilde{M}^2H^2}{4(\tilde{J}+\frac{\tilde{D}}{2}-2K)}, & \{H_b^{\mathrm{sat}}, H_2\}. \end{cases} \tag{6.16}$$

The first two segments correspond to $dE > 0$, the last three to $dE < 0$. A full description, including the domain dynamics connected to the Fe moments at high magnetic fields above $H_2$, can be found in Tab. C.1 in Appendix C, which summarizes all cases and the corresponding fields.

Furthermore, Fig. 6.8 shows a full map of the energy difference $dE$, as a function of the effective variables $K/J_\perp$ and $MH/J_\perp$ on a semi-log plot and a representative cross

[1] The following $\varphi$-values are only given for the sake of clarity. Strictly speaking $\varphi(H_1) = \pi/4$, and the range of $\varphi$ in the above paragraph hold only for infinitesimally small $K$, because for finite $K$, e. g.: $\pi/4 < \varphi(H_1) \leq \pi/2$, as can be seen by inserting Eq. (6.14) into Eq. (6.6).

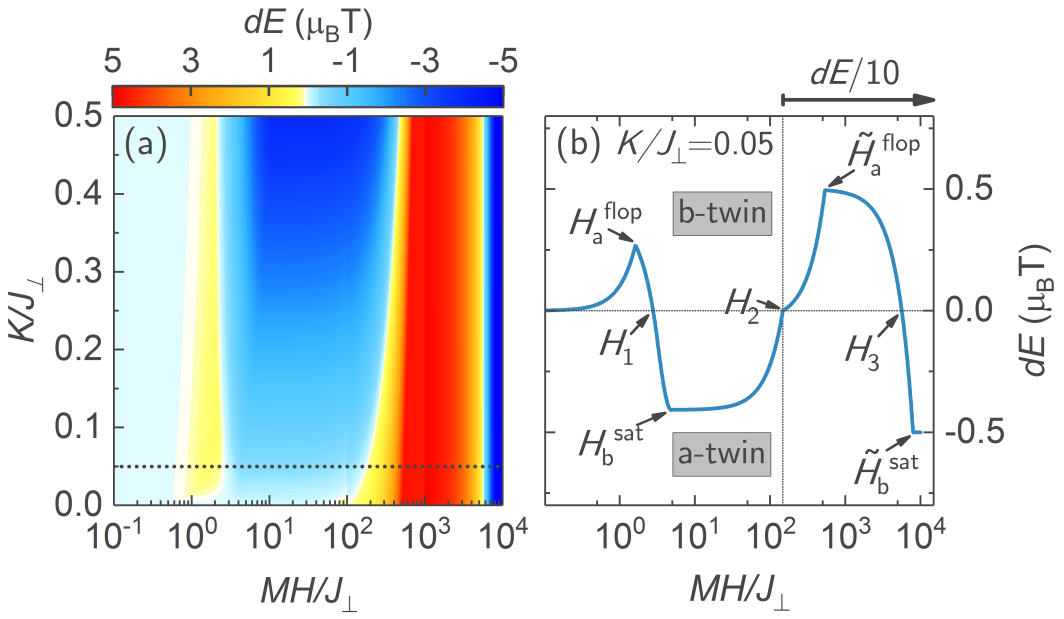


FIGURE 6.8: Theoretical domain energy difference $dE$ (a) as a function of $K/J_\perp$ and $MH/J_\perp$. The dotted line indicates the cross section shown in (b) as a function of $MH/J_\perp$ for $K/J_\perp = 0.05$. Above $H_2$ (vertical line) the $dE$ values are rescaled by a factor of 1/10 for clarity. The parameters $\tilde{J} \approx 300J_\perp$, $\tilde{D} \approx 2.5J_\perp$ ,and $\tilde{M}/M \approx 0.15$ were assumed above $H_b^{\mathrm{sat}}$.

section (dotted line) for $K/J_\perp = 0.05$. Positive values correspond to the $b$-twin, while negative values correspond to the $a$-twin. The energy difference first increases (Eu canting), stabilizing the b-twin domains. Above $H_a^{\mathrm{flop}}$, $dE$ decreases quickly, due to the spin-flop of the $Eu^{2+}$ moments in the a-twins, leading to the stabilization of the a-twin domain. For fields larger than $H_b^{\mathrm{sat}}$, the detwinning directly connected to the $Eu^{2+}$ moments is completed (with $dE = -8K$), and we enter the regime of the Fe moments, where the same behavior repeats qualitatively. Finally, above $\tilde{H}_b^{\mathrm{sat}}$ the energy difference saturates permanently at a value of $dE = -2\tilde{D}$, and the domain dynamics conclude.

### 6.2.5 Detwinning Barrier

Until now, we considered that the reorientation of domains is not associated with any energy cost and the system is always in the state with the lowest energy. In reality, however, there will be an unknown energy barrier $\Delta$ connected with a domain reorientation. Consequently, the energy difference $dE$ between the two twin domains has to exceed a certain threshold before reorientation occurs. It is useful to get an order of magnitude estimate of $\Delta$, i. e. an idea of its strength, before discussing this term in more detail. To this end, we will now briefly consider the case of $BaFe_2As_2$.

Detwinning in $BaFe_2As_2$ is reported to set in around 15 T and to nearly complete around 30 T [166, 167]. We know from Eq. (6.13) that an increasing magnetic field leads to an

energy gain of $\tilde{E}_b \sim (\tilde{M}H)^2/4\tilde{J}$ per f.u in the b-twin, due to canting of the Fe moments away from the easy-axis. As elaborated, the system has two options how to respond to this energy gain, even if the field is applied along the $a$-axis. The moments could rotate from the AF configuration into the spin-flop state, however, the associated field is of the order of 130 T and will not occur in typical lab environments. The other option is to switch an entire a-domain into a b-domain, i. e. detwin with $b \parallel H$, as just discussed. Therefore, it can be deduced that $\Delta \sim \tilde{E} = (\tilde{M}H)^2/4\tilde{J} \approx 25\,\mu\text{eV/f.u.}$

One can verify this deduction by considering the in-plane stress $\sigma$ exerted on average on a unit cell during mechanical detwinning and by calculating the energy associated with the displacement $\delta$ necessary to change from the $a \parallel \sigma$ to $b \parallel \sigma$ arrangement. The stress needed for mechanical detwinning of IBSCs is in the range 6-20 MPa [37, 38]. Assuming $\sigma \sim 10\,\text{MPa}$ and an area of $A = b \cdot c \approx a \cdot c \sim 70 \times 10^{-20}\,\text{m}^2$ the force needed per unit cell for detwinning is given by $F = \sigma \cdot A \sim 7 \times 10^{-12}\,\text{N}$. Using the displacement $s = |a - b| \sim 1 \times 10^{-12}\,\text{m}$ the detwinning energy per unit cell is given by $\Delta = F \cdot s \sim 0.04\,\text{meV}$, or $\Delta \sim 10\,\mu\text{eV/f.u}$, which is in excellent agreement with the previous estimate.

Yet another way to gauge the size of the detwinning barrier is the following: from the applied detwinning stress $\sigma$, the strain $\epsilon$ can be calculated using the elastic modulus $\Upsilon$ via $\sigma(\epsilon) = \Upsilon \cdot \epsilon^2$. A value of $\Upsilon = 6.8\,\text{GPa}$ has been estimated for $SrFe_2As_2$ [172]. Thus, assuming $\Upsilon \sim 10\,\text{GPa}$ and again $\sigma \sim 10\,\text{MPa}$, this yields $\epsilon^2 \sim 1 \times 10^{-3}$. Using the calculated energy as a function of the ratio $b/a$ for columnar magnetic order in $SrFe_2As_2$, by Jesche *et al.* [173] $E \sim 10\,\text{meV/f.u.} \cdot \epsilon^2$, this leads to $\Delta \sim 10\,\mu\text{eV/f.u}$, which again yields the same order of magnitude as the other estimates.

However, the actual energy barrier of a specific sample, will not be a single fixed value, but rather have a certain distribution over various domain walls throughout the sample. In the following, we will assume that the energy barrier for various domain walls has a log-normal distribution (see Chapter. 2). Such a distribution is typical, e. g. for the concentration of elements and their radioactivity in the earth's crust [39], or more appropriately, for grain sizes in polycrystalline matter [174]. A log-normal distribution, in our case, implies that $\log(\Delta)$ is normally distributed.

We have seen that $dE$ changes sign at the detwinning fields (Fig. 6.8) and consequently is not positive throughout the entire field range. This must be taken into account when choosing an appropriate function for the domain distribution. A piecewise fit function modeled from the cumulative distribution function of the log-normal distribution can successfully describe the domain distribution, as I will show in the last part of this

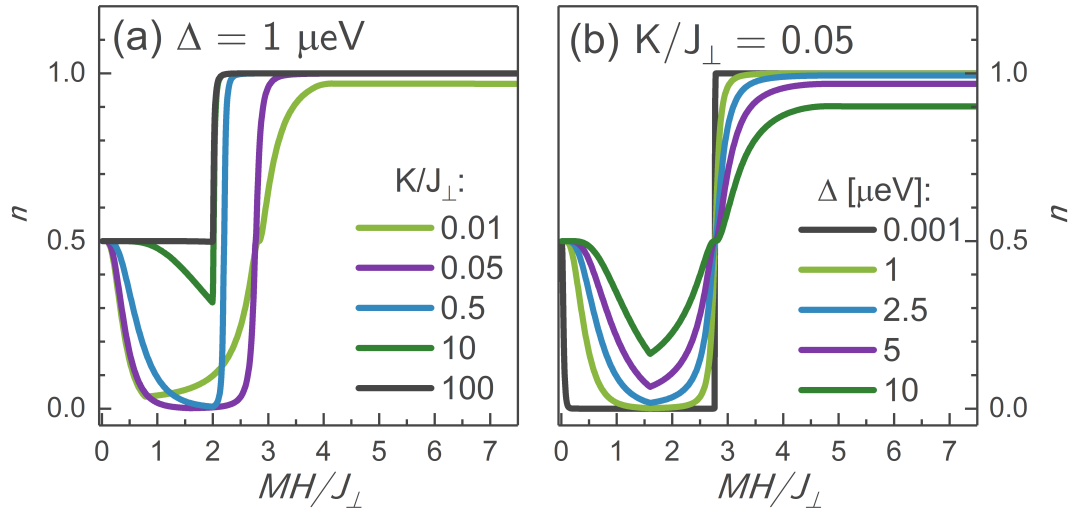


FIGURE 6.9: Evolution of the theoretical domain distribution as a function of (a) $K/J_\perp$ and (b) $\Delta$.

chapter. The following function describes the distribution of a-twin domains

$$n(dE) = \begin{cases} n_0 \cdot \frac{1}{2}\,\mathrm{erfc}\left(\frac{\log(dE/\Delta)}{\sqrt{2}}\right), & dE > 0 \\ dn \cdot \frac{1}{2}\,\mathrm{erfc}\left(-\frac{\log(-dE/\Delta)}{\sqrt{2}}\right) + n_0, & dE < 0, \end{cases} \tag{6.17}$$

with $n_0$ the fraction of a-twin domains at zero field, $dn = n_{\mathrm{sat}} - n_0$ the difference between the saturated region $n_{\mathrm{sat}}$ above $H_1$ and $n_0$, and erfc the complementary error function. The field dependence of $n$ is given by $dE$ (Eq. (6.16) and Tab. C.1) and the parameters $n_0$, $dn$ and $\Delta$ can be determined from experiment. The evolution of $n$ for various values of $\Delta$ and $K/J_\perp$ is depicted in Fig. 6.9.

## 6.3 Experimental Evidence

Experimental evidence for the theoretically discussed multistage magnetic detwinning effect in $EuFe_2As_2$ is presented in this section. It includes measurements of the electrical resistivity, thermal expansion, and magnetostriction, as well as neutron diffraction, magnetization, and thermoelectric power.

Before the individual measurements are discussed in detail, the effect on the resistivity and thermoelectric power of a magnetically detwinned sample is presented. Figure. 6.10 shows a direct comparison between a conventionally detwinned sample using a mechanical clamp at a constant pressure of about 6 MPa and a free-standing, unstrained sample that was treated only by a small in-plane magnetic field along the $[1\,1\,0]_{\mathrm{T}}$ direction *prior* to the depicted measurement. Even though the magnetic field is switched off and no

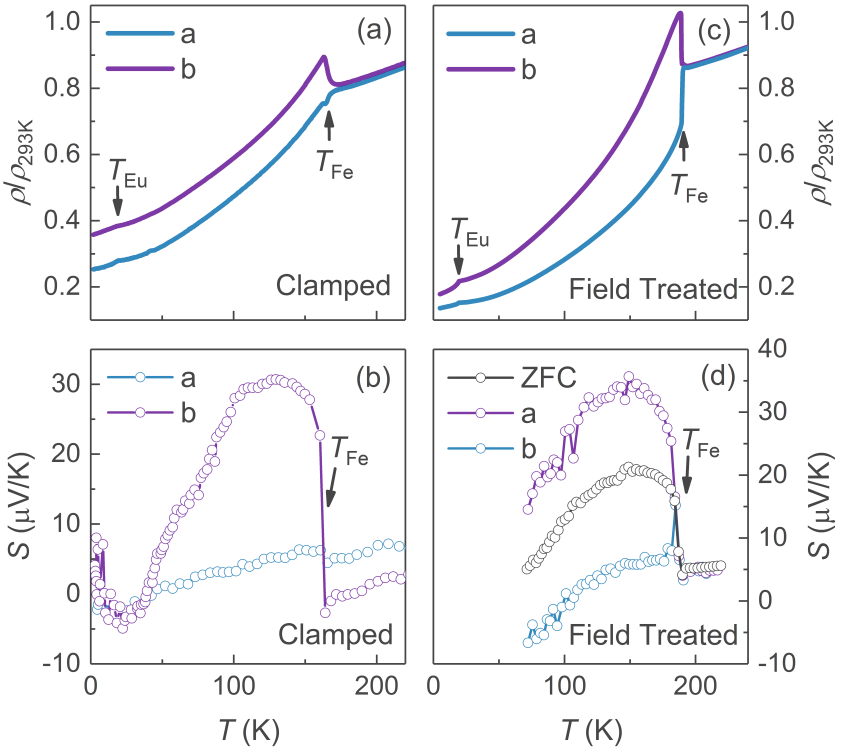


FIGURE 6.10: Normalized electrical resistivity and thermoelectric power of a (a,b) conventionally detwinned $EuFe_2(As_{1-x}P_x)_2$ sample with $x = 0.05$ at a pressure of about 6 MPa and (c,d) a magnetically detwinned, i. e. field-treated $EuFe_2As_2$ crystal measured along the orthorhombic $a$- and $b$-axes. The in-plane anisotropy can evidently be resolved in both cases. Arrows indicate the structural and magnetic phase transitions labeled $T_{Fe}$. Data in (a,b) are taken from Ref. [38].

symmetry breaking strain from a pressure clamp is present during measurement, the system exhibits a substantial detwinning effect comparable to the mechanically strained sample. Perhaps even more intriguing, the induced effect is persistent up to highest temperatures, i. e. the structural and magnetic transitions at $T_{Fe} \approx 190\,K$.

Due to the persistence of the observed detwinning, it is important to ensure that the twin distribution of the crystals is not affected by previous measurements, and that the samples are reproducibly prepared in the same structural state. Therefore, a well-defined measurement protocol was developed. Unless stated otherwise, the crystals were always cooled from above $T_{Fe}$ to below the Eu ordering temperature $T_{Eu} = 19\,K$ (typically down to $T = 5\,K$) in zero magnetic field, and the "zero-field cooled" (ZFC) data was recorded. Afterwards, an in-plane magnetic field $H = 4\,T$ was applied (typically along the $[1\,1\,0]_T$ direction) and immediately[2] removed again, prior to further measurements. This process will be called *field treatment* (FT), in the following.

[2]The duration of the applied field does not significantly affect the detwinning.

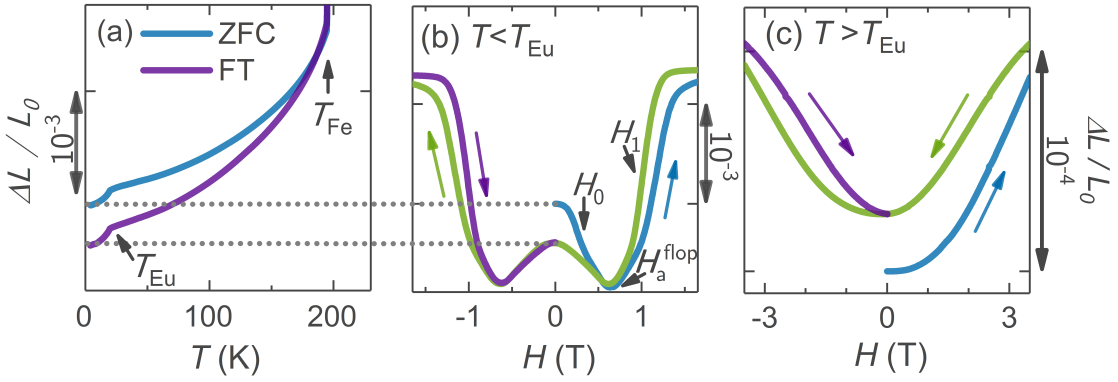


FIGURE 6.11: Relative length changes $\Delta L/L_0$ of $EuFe_2As_2$ for $\Delta L \parallel H$ and $H \parallel [1\,1\,0]_T$. (a) Thermal expansion $\Delta L(T)/L_0$ after ZFC (twinned) and FT (detwinned) at 5 K. (b) Magnetostriction $\Delta L(H)/L_0$ at 5 K and (c) 30 K. Colored arrows indicate increasing (blue, violet) and decreasing (green) $H$, while gray arrows indicate characteristic field values (see Sec. 6.2). Data taken from Ref. [156].

### 6.3.1 Thermal Expansion & Magnetostriction

Thermal expansion (TE) and magnetostriction (MS) directly probe the relative length change of the sample as a function of temperature and applied magnetic field, $\Delta L(T)/L$ and $\Delta L(H)/L$, respectively. Due to the small orthorhombic distortion of about $\delta = (a-b)/(a+b) \sim 10^{-3}$, calculated from the reported lattice parameters [106, 175] below the structural and SDW transition $T_{Fe}$, a reorientation of twin domains should be well detectable in those quantities.

The thermal expansion $\Delta L(T)/L_0$ of $EuFe_2As_2$ with $\Delta L \parallel [1\,1\,0]_T$ (Fig. 6.11a) decreases significantly at $T_{Fe}$ and again, only more subtle, below $T_{Eu}$. After FT with $H \parallel [1\,1\,0]_T$ below $T_{Eu}$ the sample is considerably shorter than after ZFC. While the TE only shows the effect of FT, the MS (Fig. 6.11b) reveals the process during FT. At $T < T_{Eu}$ the sample shrinks with increasing field until reaching a minimum around $H_a^{flop} = 650\,mT$. Higher fields lead to a dramatic increase and a subsequent saturation of the sample length above 1.5 T. After removal of the field, the initial length is not recovered and the sample remains shorter. The difference between ZFC and FT matches the difference observed in the thermal expansion, as indicated by the dotted gray lines. In the paramagnetic state of $Eu^{2+}$ at $T > T_{Eu}$, the sample length increases continuously with increasing field (Fig. 6.11c). No saturation is observed up to 4 T, but the initial sample length is again not recovered, after the field is removed. The magnitude of the MS—typically of the order of $10^{-6}$ to $10^{-5}$ in other Eu-based materials [156, 176, 177]—is with $10^{-3}$ extremely large and corresponds to the magnitude of $\delta$.

Additionally, the MS of a slightly Ru-doped sample (Fig. 6.12) starts to decrease again at high magnetic fields above 12 T, indicating another reorientation of domains. The feature

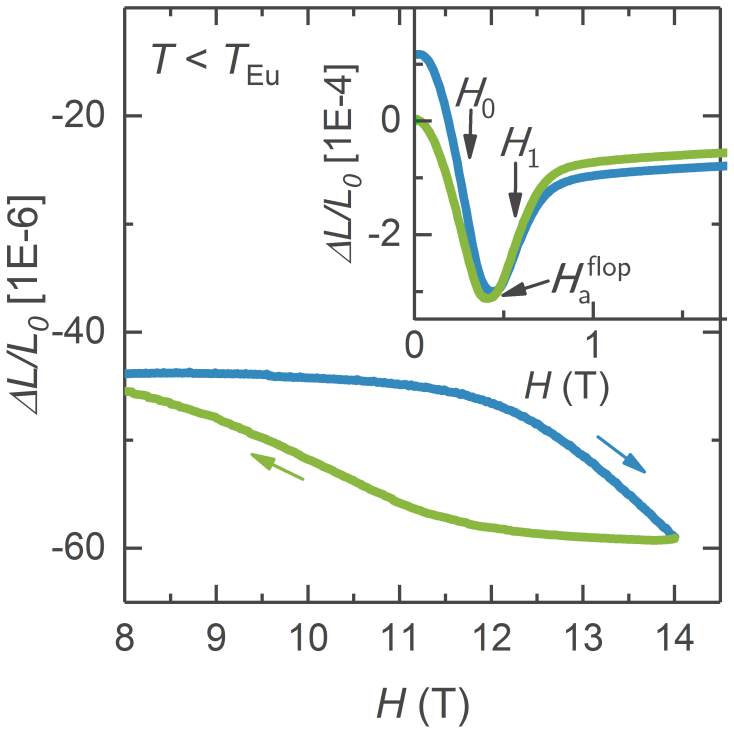


FIGURE 6.12: High-field magnetostriction of a $Eu(Fe_{1-x}Ru_x)_2As_2$ crystal with $x = 0.075$ at 5 K and with $H \parallel [1\,1\,0]_T$ after ZFC. Around 12 T a decrease is starting to occur. (Inset) The low-field behavior is qualitatively identical to the undoped $EuFe_2As_2$. Arrows/colors indicate increasing/decreasing magnetic field. Measurements recorded at a dilatometer pressure of about 1.7 MPa.

is likely to be observed in $EuFe_2As_2$ as well, because the sample with $x = 0.075$ shows no qualitative differences in the MS at small fields compared to the parent compound. The Ru-doped series will be discussed in more detail in the next chapter.

In order to assess whether the observed behavior is related to $Eu^{2+}$ moments a reference measurement on a $BaFe_2As_2$ single crystal in the same configuration ($H \parallel [1\,1\,0]_T$) was conducted (Fig. 6.13). The results show no comparable signature. Another reference measurement on $EuFe_2As_2$ in the $H \parallel [1\,0\,0]_T$ configuration, i. e. with the field at an angle of 45° to the easy axes in *both* twin variants, resulted in a similarly featureless behavior [156].

**Discussion**

These measurements indicate that a significant imbalance in the twin domains can be induced by a small magnetic field applied along the $[1\,1\,0]_T$-direction in $EuFe_2As_2$. The twin domains at $T < T_{Eu}$ initially orient with the shorter $b$-axis parallel to the field ($b \parallel H$, b-twin), leaving the sample shorter, and then abruptly re-orient with $a \parallel H$ (a-twin) at higher fields expanding the sample. Above 12 T another reduction of the sample length indicates yet another reorientation, which again favors b-twins. These

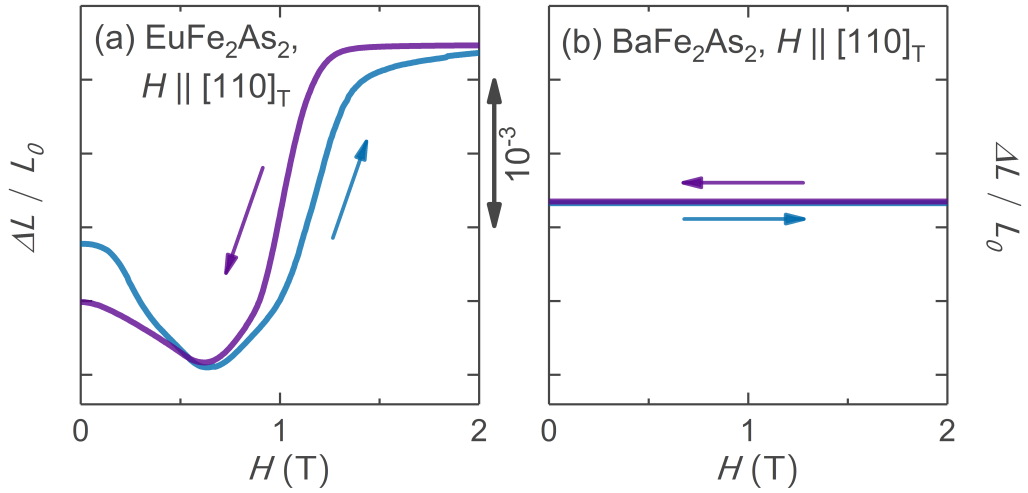


FIGURE 6.13: Reference measurement. (a) Magnified magnetostriction $\Delta L(H)/L_0$ of $EuFe_2As_2$ with $H \parallel [1\,1\,0]_T$, as shown in Fig. 6.11. (b) Magnetostriction of $BaFe_2As_2$ with $H \parallel [1\,1\,0]_T$. Data are plotted on the same scale and were recorded at 5 K. Colored arrows indicate increasing (blue) and decreasing (violet) $H$. Detwinning is only observed for $EuFe_2As_2$. Data are taken from Ref. [156].

observations are in agreement with our new detwinning theory presented above and the characteristic fields were labeled accordingly.

In contrast to this *multistage* detwinning process, the MS above $T_{Eu}$ exhibits only a one-step process, with a reorientation that directly aligns $a \parallel H$. Manifestations of this process are far less dramatic and require much higher fields compared to FT at $T < T_{Eu}$. However, persistent and irreversible domain reorientation is still observed.

This one-step process can be understood within the framework of our new model, by considering the following argument: The $Eu^{2+}$ moments are paramagnetic above $T_{Eu}$ and no spin-flop can occur. With increasing field, the $Eu^{2+}$ moments of both domains can, therefore, gradually align with the field direction. This eventually leads to a situation in which the moments of the a-twin are parallel to the magnetic easy a-axis, while they are perpendicular in the b-twin. The latter configuration is disfavored by the biquadratic coupling $K$, which tries to align the moments collinear to the Fe moments. Those, in turn, point along the easy axis, due to the single-site anisotropy $\tilde{D}$. Consequently, the energy of the a-twins must be lower than that of the b-twins, and the system detwins with the a-twin in field direction. This argument is also supported by magnetoresistance measurements presented below. Both sets of measurements were recorded at 30 K. At this temperature and for an in-plane field of 2 T, FM order is reported for the $Eu^{2+}$ moments [168, Fig. 3b], which is exactly where the MS (Fig. 6.11c) and the MR (Fig. 6.15b) show the largest changes, further supporting the argument.

The absence of the two-step detwinning in the case of $BaFe_2As_2$ proves that the effect is related to the $Eu^{2+}$ moments. Unfortunately, the absence of a similar signature in the $H \parallel [1\,0\,0]_T$ configuration does not conclusively prove that the effect in $EuFe_2As_2$ is related to domain distributions as claimed in Ref. [156]. Although the inference made is likely true, the dilatometer utilized for the measurement is conceptually not sensitive to length changes due to detwinning in this configuration, because the $[1\,0\,0]_T$ lattice vector is identical in both twin variants and thus no signal is expected.

In Ref. [156], Zapf *et al.* estimate the degree of detwinning by calculating the TE, using the temperature-dependent evolution of the $a, b$ lattice parameters from Tegel *et al.* [175] and assuming a temperature-independent fraction of twin domains. Values of the b-twin domain ($b \parallel H$) in measurement direction of 66 % after ZFC and 70 % after FT below $T_{Eu}$ are reported. Assuming ideal twinning during cooling, one would expect a 50:50 distribution for the ZFC case. Therefore, the TE (Fig. 6.11a) indicates that a significant imbalance of twin domains was generated prior to field treatment. This imbalance was attributed to the uniaxial pressure from the dilatometer (1.35 MPa for this particular sample) [156, Supplement]. Uniaxial pressure within the $ab$-plane is known to detwin IBSCs, with the shorter $b$-axis parallel to the applied pressure. A pressure of only 6 MPa reportedly detwins $EuFe_2As_2$ completely [38]. Therefore, a partial detwinning during TE and MS measurements in this setup can not be excluded.

Although the results in Ref. [156] are, therefore, reasonable, the calculated twin distributions can not be considered accurate for several reasons. The structural transition temperature $T_{Fe}$ determined from TE is about 5 K larger compared to findings from pressure-free measurements, like electrical transport. In accordance with the neutron diffraction measurements on $BaFe_2As_2$ [163], this increase can be attributed to the pressure of the dilatometer. According to Ref. [163, Fig. 2(b)], uniaxial pressure also alters the lattice parameters. However, the extracted lattice parameters from Tegel *et al.* used in Ref. [156] were measured without pressure. Furthermore, both data sets in Ref. [156] seem to have been analyzed after normalization to the structural transition $T_{Fe}$. The resulting relative change between the ZFC and FT thermal expansion influences the value obtained for the twin distribution. Furthermore, the assumption of a temperature-independent distribution of twin domains is only roughly applicable, as we will see when discussing the $T$-dependent neutron diffraction data later in this chapter.

### 6.3.2 Resistivity & Magnetoresistance

The magnetic detwinning is also observed in measurements of the in-plane electrical resistivity $\rho(T)$ along the $[1\,1\,0]_T$ direction, as already indicated at the beginning of

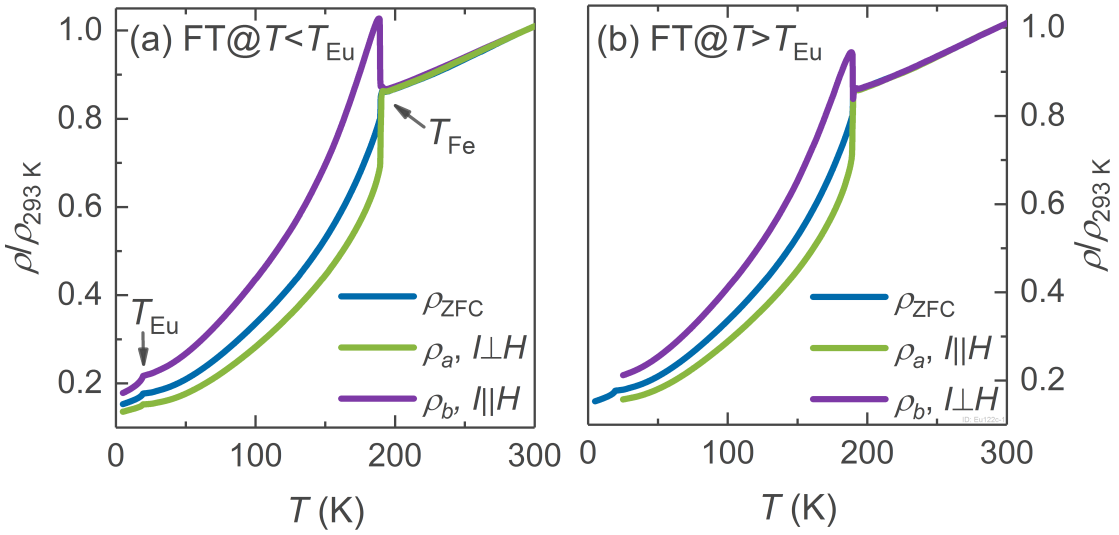


FIGURE 6.14: Normalized electrical resistivity of $EuFe_2As_2$ with the current $I$ flowing along the in-plane $[1\,1\,0]_T$ direction for ZFC (twinned) and (a) FT at $T < T_{Eu}$ and (b) FT at $T > T_{Eu}$. By changing between $I \parallel H$ and $I \perp H$ the resistivity predominantly along the $a$-axis ($\rho_a$) or $b$-axis ($\rho_b$) can be resolved. Note the reversed detwinning above $T_{Eu}$.

this section. The effect of FT with $H \parallel [1\,1\,0]_T$ on the $T$-dependence of $\rho$ (Fig. 6.14) is similar to mechanical straining. By comparing the results to the latter [38, 158, 178, and Fig. 6.10a] it becomes evident that the configurations with the current $I \parallel H$ and $I \perp H$ correspond to the resistivity along the $b$-axis ($\rho_b$) and along the $a$-axis ($\rho_a$), respectively for FT below $T_{Eu}$. Note that this relation reverses in the paramagnetic state of $Eu^{2+}$ above $T_{Eu}$, where now the $a$-axis is favored for $I \parallel H$. The high-$T$ part above $T_{Fe}$ shows no difference between FT and ZFC curves, as no twin domains exist in the tetragonal phase. The ZFC curve is not exactly located between the FT measurements, as expected for a fully twinned sample, i. e. equal domain distribution. It, therefore, indicates an excess of a-twins in agreement with the presumption made in the previous chapter during the discussion of the increase of $\rho(T)$ at $T_{Fe}$. Furthermore, the observed effect is virtually constant up to $T_{Fe}$, although no magnetic field is present during the measurements.

Insight into the domain dynamics during FT can again be gained by considering the field-dependent quantity (Fig. 6.15), i. e. the magnetoresistance (MR). As introduced in the last chapter, it is defined by $MR_{293\,K} = [R(H) - R(H = 0)]/R(T = 293\,K)$, where $R(H = 0)$ is the resistance after FT at $H = 0$. The magnetic field was applied parallel to the current. Below $T_{Eu}$, the MR reveals a two-step process in which the MR initially increases with increasing field around $H_0$ until it reaches a maximum at $H_a^{flop} \approx 400\,mT$ for this sample. This is followed by a rapid decrease around $H_1 \approx 690\,mT$ and eventual saturation above 1 T. Reversing the field direction also leads to a reversal in the MR. A

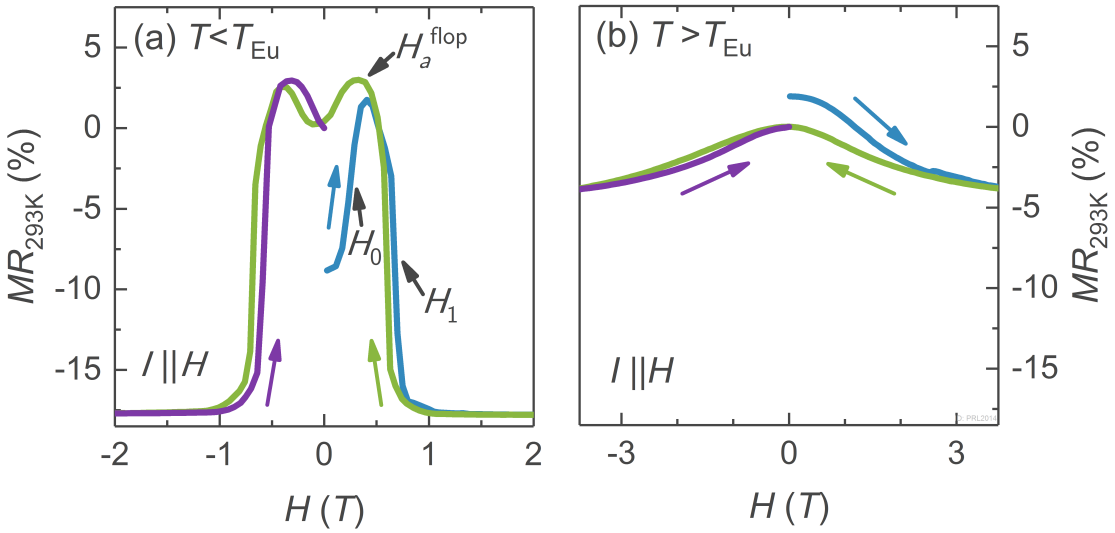


FIGURE 6.15: Magnetoresistance of $EuFe_2As_2$ normalized to the resistance after FT $R(H = 0)$ recorded at (a) 5 K and (b) 30 K. The magnetic field $H$ was applied parallel to the $[1\,1\,0]_T$ direction and the electrical current $I$. Colored arrows indicate increasing (blue, violet) and decreasing (green) $H$, while gray arrows indicate characteristic field values derived in Sec. 6.2.

hysteresis of about 100 mT is evident and, similar to the magnetization of a ferromagnet (Fig. 2.3), the initial $R(H)$ curve is not recovered. Above $T_{Eu}$, again only a single-step behavior is observed, in which the MR decreases monotonically until saturation above 4 T is reached. Nonetheless, hysteretic and irreversible behavior is still observed.

Upon rotating the sample around the $c$-axis towards a configuration where the field $H$ is applied along the $[1\,0\,0]_T$ direction (Fig. 6.16a, angles $\pi/4$ and $5\pi/4$) the magnitude of the MR reduces significantly. If $H$ is applied perpendicular to $I$ (angle $\pi/2$) the MR is qualitatively reflected across the $H$-axis. If FT in the $H \parallel [1\,1\,0]_T$ configuration is performed at increasingly higher temperatures (Fig. 6.16b), the observed detwinning signature disappear gradually, while a qualitative change is observed when transitioning from the AF to the PM state of Eu, as indicated above. The temperature and angle-dependent measurements were recorded on a slightly P-doped sample. However, the small doping concentration has little effect on the qualitative behavior of the MR. The observed behavior is, therefore, very likely to be seen in the pure $EuFe_2As_2$ system as well.

**Discussion**

The MR at 5 K measured along the $[1\,1\,0]_T$ direction has an overall magnitude of $\sim 60\,\%$, when it is normalized to $R(T = 5\,\mathrm{K}, H = 0)$, instead of the $R(T = 293\,\mathrm{K}, H = 0)$, which is typically used throughout this thesis. The MR is, therefore, comparable to other Eu-based systems. In compounds like EuTe, EuSe, EuPtP, $EuNiGe_3$, for instance, the

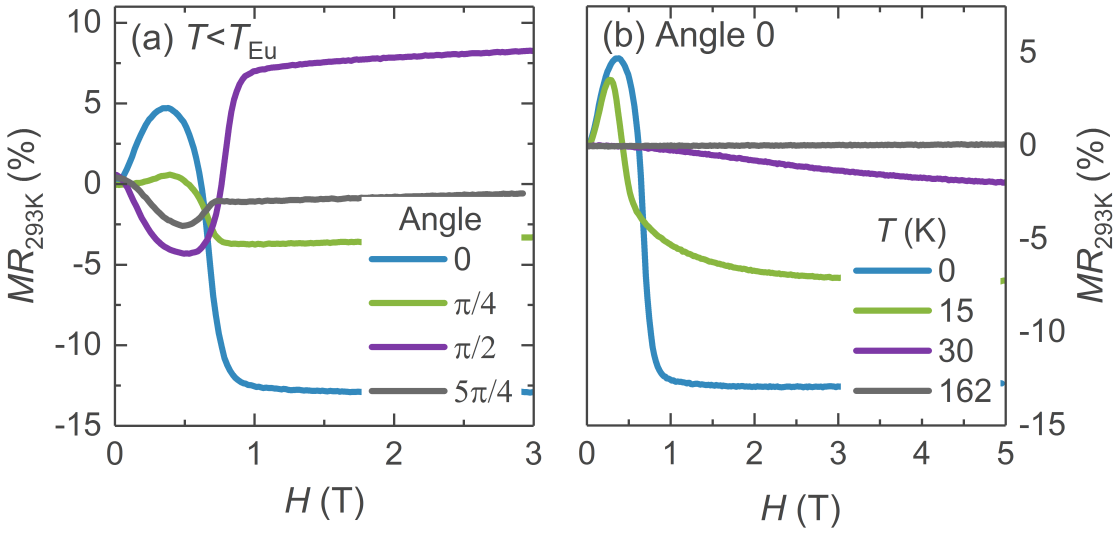


FIGURE 6.16: Magnetoresistance of $EuFe_2(As_{1-x}P_x)_2$ with $x = 0.05$ as a function of decreasing magnetic field (a) at $T = 5\,\mathrm{K} < T_{Eu}$ for various angels between the electrical current $I$ and the magnetic field $H$, and (b) for $I \parallel H$ for various temperatures.

MR ranges from $-70\,\%$ to $30\,\%$ [179–182]. Much larger magnetoresistance effects are only observed e. g. in $Eu_6C_{60}$ at low temperatures ($\approx 1\,\mathrm{K}$), where $\rho(9\,\mathrm{T})$ is three orders of magnitude smaller than $\rho(0\,\mathrm{T})$. This corresponds to a MR of $-99.9\,\%$, which is of similar magnitude as the CMR materials, such as the perovskite manganese oxides [183].

These signatures in the electrical transport mirror those in the MS and TE and are, therefore, consistent with the irreversible motion of twin domains. This becomes particularly evident, when we consider that the shorter $b$-axis has a larger resistivity than the longer $a$-axis, i. e. $\rho_b > \rho_a$ [38, 158]. The increasing field at $T < T_{Eu}$ initially generates b-twins ($b \parallel H$) corresponding to the increase in MR and then abruptly leads to a-twins ($a \parallel H$) around $H_1$, corresponding to a decrease in MR.

The MR above $T_{Eu}$ shows a one-step process, with $a \parallel H$ in accordance with the MS data. Despite being less pronounced and requiring higher fields, it still induces persistent and irreversible domain reorientation.

The changes in the MR have previously been attributed to electron-spin scattering [184]. However, due to the MS data and the neutron data presented in the next subsection, as well as the new detwinning theory, they must predominantly be attributed to the magnetically induced detwinning effect.

The observed reduction of the MR upon rotating the field by 45° around the $c$-axis can be taken as evidence that virtually no detwinning takes place in this configuration. The remaining signal of $(\pi/4,\ 5\pi/4)$ can easily be attributed to a slight misalignment of the sample in the magnetic field. Errors in the alignment are introduced during the

orientation and subsequent cutting of the sample, and due to the limited accuracy of the rotator platform.

Further evidence for the detwinning comes from the measurement with the field perpendicular to the current ($\pi/2$). At small fields, the b-twin phase is stabilized in field direction ($b \parallel H$). Consequently, the sample must be detwinned with $a \perp H$. Therefore, the observed reflection of the MR across the $H$-axis is expected, as the MR is now a measure of the amount of a-twin domains.

### 6.3.3 Neutron Diffraction

Although, the features in the above measurements strongly indicate the proposed detwinning process, they can not be considered conclusive proof, because theses measurements do not directly probe the distribution of twin domains. Neutron diffraction, however, directly probes structural and magnetic long-range properties of a material. The technique is ideally suited for the investigation of the detwinning mechanism, not only because it measures the bulk of the material, but also because no external stress or strain is exerted on the sample, as was the case in the dilatometric data. Furthermore, the peak intensities are directly related to the twin domain distribution.

Data were taken within the $(h\,0\,l)_\mathrm{O}$ scattering plane, such that the orthorhombic $a$-axis and $b$-axis of the twinned samples were measured. The in-plane magnetic field was applied perpendicular to the scattering plane, due to technical restrictions. In contrast to the previous measurements, where the measurement direction was mostly parallel to $H$, this configuration probes the response of the system perpendicular to the field, similar to MR measurements with $I \perp H$. Consequently, if b-twins are favored upon application of magnetic field, the intensities of the $(4\,0\,0)_\mathrm{O}$ nuclear reflection belonging to the $a$-axis will increase, while for a-twins the $(0\,4\,0)_\mathrm{O}$ reflection ($b$-axis) will increase.

$Q$ scans after ZFC at $T < T_\mathrm{Eu}$ (Fig. 6.17a) reveal a broad peak (violet symbols) that can be modeled by a mixture of two Gaussian distributions (blue symbols) with equal spectral weight, corresponding to the a-twin and b-twin domains. Upon increasing $H$ (Fig. 6.17b), spectral weight is initially shifted to the $(4\,0\,0)_\mathrm{O}$ reflection, indicating an alignment of the longer $a$-axis perpendicular to the field and thus an increase of the amount of b-twins in field direction. At higher fields (Fig. 6.17c) the situation reverses, favoring a-twins. After FT (Fig. 6.17d) the initial distribution of spectral weight is not recovered and the amount of b-twins outweighs that of the a-twins, leaving the sample partially detwinned as seen in the previous experiments. This behavior can also be seen

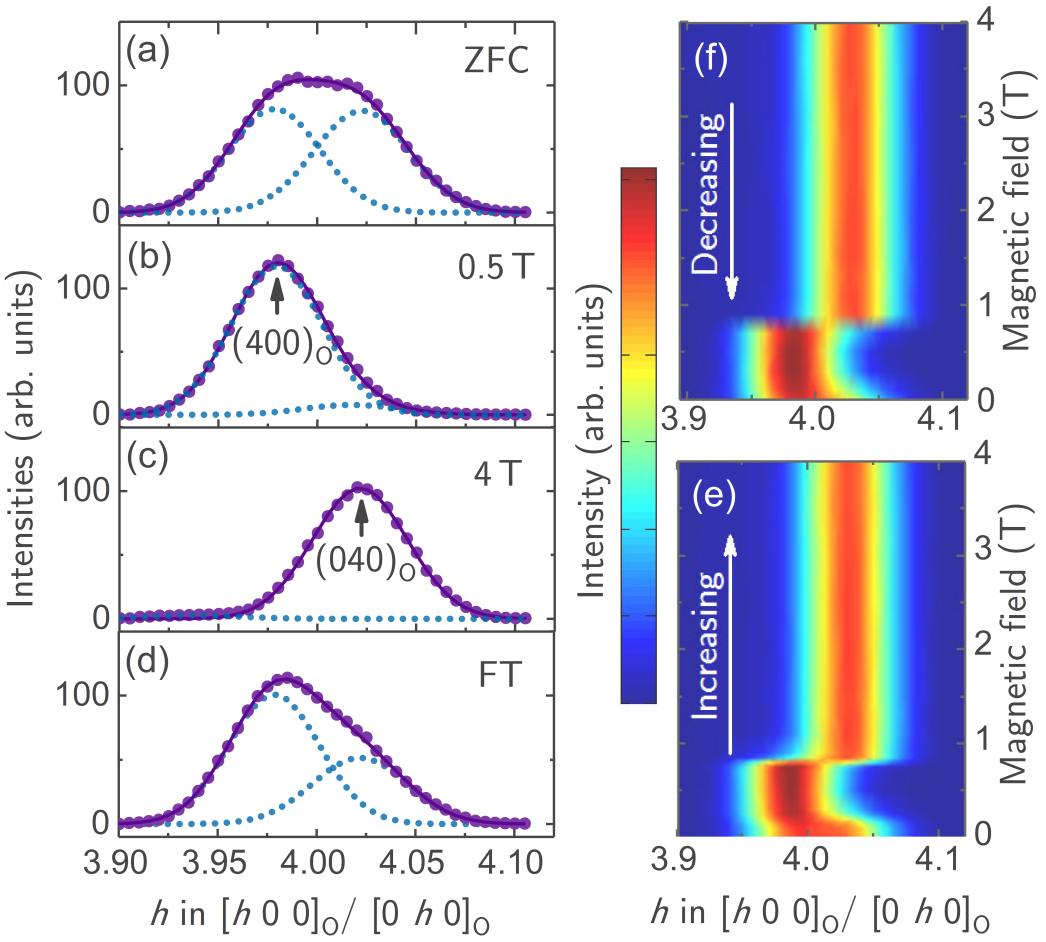


FIGURE 6.17: Selected nuclear reflections of $EuFe_2As_2$ at 2 K with $H \parallel [1\,1\,0]_T$. $Q$ scans of the $(4\,0\,0)_O$ and $(0\,4\,0)_O$ reflections are shown for (a) ZFC (b,c) during FT at two characteristic fields, and (d) after FT. Solid lines indicate the sum of two Gaussians (blue, dotted symbols) used to fit both peaks. The evolution of the distribution of the $(4\,0\,0)_O$ and $(0\,4\,0)_O$ reflections during FT are also shown for (e) increasing and (f) decreasing field. Measurements performed together with Y. Xiao and S. Nandi.

from the continuous field dependence of the integrated intensities for increasing and decreasing field (Fig. 6.17e,f).

The distribution of twin domains is given by the relative ratio of the integrated intensities $I_{(hkl)}$, i. e. for the a-twin $n = I_{(400)}/(I_{(400)} + I_{(040)})$. After ZFC the sample is in fact fully twinned (Fig. 6.18) with $n \approx 50\,\%$, while after FT below $T_{Eu}$ we find $n = 35\,\%$ (i. e. 65 % b-twins) and in a constant field above $H_1 \sim 1\,T$ $n \approx 98\,\%$. After FT and for increasing temperature, $n$ increases slowly and reaches 38 % at $T_{Eu}$. Above, the rate of change reduces significantly leading to $n = 42\,\%$ at 170 K, before the twin domains disappear in the tetragonal phase above $T_{Fe}$. In a constant field of 3 T the behavior is more pronounced but qualitatively almost identical. Merely, the reduction of the rate of change is shifted from $T_{Eu}$ to 47 K. The field dependence of $n$ (Fig. 6.18b) exhibits a virtually identical behavior to the MS data (Fig. 6.11b), again featuring a two-step

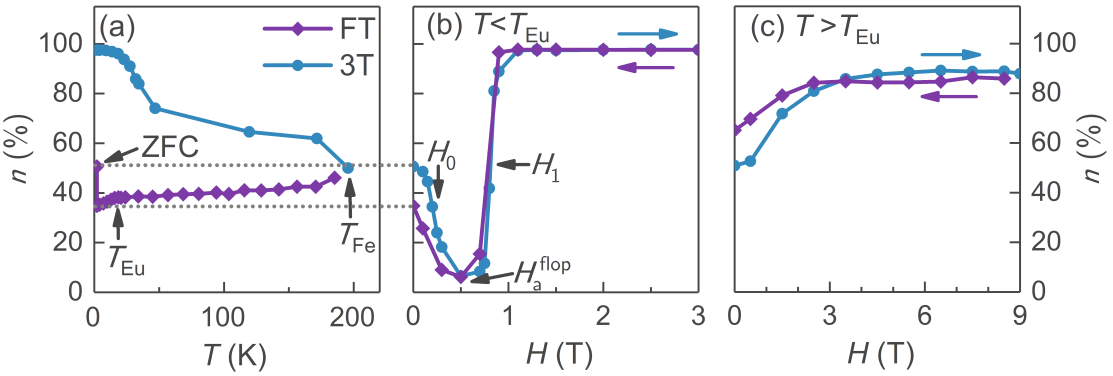


FIGURE 6.18: Distribution $n$ of the a-twin domains in $EuFe_2As_2$ (a) as a function of increasing temperature after ZFC, FT at $T < T_{Eu}$ and during $H = 3\,T$ as well as a function of $H \parallel [1\,1\,0]_T$ for FT at (b) $T < T_{Eu}$ and (c) $T > T_{Eu}$. Colored arrows indicate increasing (blue) and decreasing (violet) $H$, while gray arrows indicate characteristic field values (see Sec. 6.2). Measurements performed together with S. Nandi and Y. Xiao.

process for FT below $T_{Eu}$ and a less pronounced one-step process above, leading to $n = 89\,\%$ above 3 T (Fig. 6.18c).

**Discussion**

The presented neutron data prove the multistage detwinning processes as proposed by the detwinning theory and indicated above by transport and dilatometric measurements. Furthermore, the data prove virtually full detwinning at $H_a^{flop}$ ($n \approx 6.5\,\%$, i.e 93.5 % b-twins) and above $H_1$ ($\approx 97.5\,\%$ a-twins). These values and the almost ideal twinning after ZFC of this free-standing sample are in stark contrast to the previous MS data. Consequently, they confirm the considerable influence the dilatometer pressure has on the twin distribution, as contemplated above. The similarity between $n(T)$ and the thermal expansion, as well as between $n(H)$ and the MS and MR for $I \perp H$ is impressive (see Fig. 6.18). These results indicate that both the MS and MR are suitable measurements for the extraction of the twin-domain distribution, although the varying conditions (dilatometer pressure) have to be considered. This finding is important and will be used in the final part of this chapter.

At $H = 0$ and below $T_{Eu}$, the $Eu^{2+}$ moments are ordered antiferromagnetically, while for an in-plane magnetic field of 3 T and below $T \approx 35\,K$ the order is ferromagnetic [168]. Interestingly, this seems to indicate that the magnetically ordered states favor twinning upon increasing $T$, as evidenced by the steeper $T$-dependence in those states compared to the paramagnetic state of $Eu^{2+}$ [see changes in slope of $n$ in Fig. 6.18a around 19 K (FT) and 35 K (3T)]. Nevertheless, this observation will not be discussed in more detail here.

### 6.3.4 Magnetization

The magnetization of $EuFe_2As_2$ at low temperatures is dominated by the large $Eu^{2+}$ moments, which order in an A-type AF structure below $T_{Eu}$ (Sec. 4.7). The ordered $4f$-moments are close to a FM instability [103] and small magnetic fields are reported to induce a meta-magnetic transition to a FM state, which leads to a step-like increase of the magnetization $M$ for fields $H \parallel ab$ [42]. However, measurements at specific in-plane angles have not been reported so far.

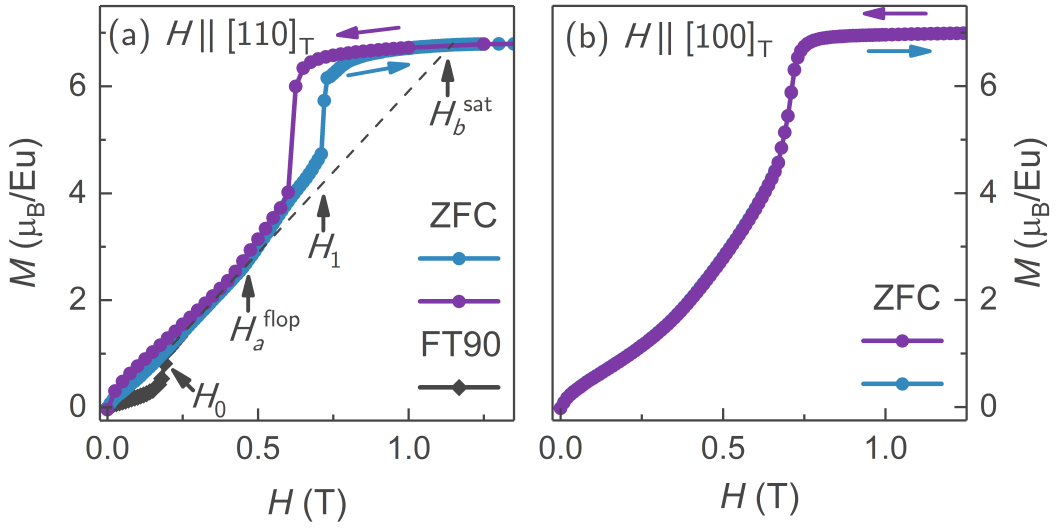


FIGURE 6.19: In-plane magnetization $M$ of $EuFe_2As_2$ in (a) $H \parallel [1\,1\,0]_T$ configuration reveals irreversible effects due to the domain dynamics. FT90 indicates a FT preparation with subsequent rotation by 90° around $[0\,0\,1]_T$ prior to measurement. (b) $M$ in $H \parallel [1\,0\,0]_T$ configuration, i.e 45° to (a) shows no irreversible effects. Colored arrows indicate increasing (blue) and decreasing (violet) $H$, while gray arrows indicate characteristic field values (see Sec. 6.2). The dashed line depicts the extrapolation of $H_b^{sat}$, as discussed in Sec. 6.4. All measurements were recorded at $T = 5\,K < T_{Eu}$.

The evolution of the low-$T$ ZFC magnetization of $EuFe_2As_2$ with $H \parallel [1\,1\,0]_T$ (Fig. 6.19) is roughly linear up to $H_1$. However, changes in slope are visible around $H_a^{flop}$ and barely noticeable also for $H_0$. If the sample is rotated by 90° around the $c$-axis after FT and then measured again (FT90) the signature at $H_0$ becomes much more pronounced. However, with further increasing field the FT90 measurement is identical to the ZFC curve. At $H_1$ the magnetization increases step-like as reported previously. Above 0.9 T, a saturation magnetization of 6.82 $\mu_B$ per $Eu^{2+}$ is reached for this sample. Upon decreasing the field, the behavior reverses. A sizable hysteresis of about 100 mT is evident not only in the step-like change, but also around $H_a^{flop}$, albeit less noticeable. Additionally, less pronounced irreversible behavior is observed in the low-field region between increasing and decreasing field.

Measured along $[1\,0\,0]_T$, the overall behavior is similar to the $H \parallel [1\,1\,0]_T$ configuration. However, most notably no hysteresis and no irreversible behavior are seen. Furthermore, the jump at $H_1$ is less dramatic and the low-field part seems more curved.

**Discussion**

The saturation magnetization is in good agreement with previous estimates and with the theoretical value of $7\,\mu_B$ [42]. All three features at $H_0$, $H_a^{flop}$ and $H_1$ can be associated with the reorientation of twin domains as discussed during the presentation of the detwinning theory. The connection between the domain reorientations and the feature at $H_0$ can be seen, when considering the FT90 measurement. After FT and subsequent rotation the sample exhibits predominantly a-twins in measurement direction. If the field increases, more a-twins change to b-twins than after ZFC. Consequently, the observed feature becomes more pronounced.

The measurement along $[1\,0\,0]_T$ indicates that no imbalance of twin domains is induced by the field, as no hysteresis and no irreversible behavior is observed. These findings are in good agreement with the previous measurements.

## 6.4 Data Analysis

In this section, the coupling constants $J_\perp$ and $K$ will be determined from experiment by using analytical expressions that can be obtained from the above detwinning theory. Furthermore, the twin domain distribution will be derived from magnetostriction and even magneto-transport data. Together with the distribution derived from neutron diffraction data this allows not only to confirm the values obtained for $J_\perp$ and $K$, but also to determine the energy barrier for detwinning $\Delta$, using the model function Eq. (6.17) to fit the data. Finally, this section concludes with a consistency check of the detwinning theory: Using the derived parameters, the field-dependent magnetization of $EuFe_2As_2$ will be computed and subsequently compared to the experimental observations.

### 6.4.1 Coupling Constants

The presented field-dependent experiments, like magnetization, magnetostriction, neutron and magneto-transport measurements, exhibit characteristic features that are sufficient for a determination of $J_\perp$ and $K$. From the detwinning theory we can find, e. g.

the following relations:

$$J_\perp = \frac{M}{8} H_b^{\mathrm{sat}} \left[ 1 + 2 \left( \frac{H_1}{H_b^{\mathrm{sat}}} \right)^2 \right]$$
$$K = \frac{M}{32} H_b^{\mathrm{sat}} \left[ 1 - 2 \left( \frac{H_1}{H_b^{\mathrm{sat}}} \right)^2 \right]. \tag{6.18}$$

$H_1$ and $H_b^{\mathrm{sat}}$ can be extracted from magnetization data (Fig. 6.19). The step-like increase of $M(H)$ at 0.65 T for this sample can be identified with the detwinning field $H_1$, while $H_b^{\mathrm{sat}} = 1.14\,\mathrm{T}$ can be determined by extrapolating the slope of the low-field region between 0.2 T and 0.5 T (see dashed line in Fig. 6.19). This leads to $J_\perp = 0.096\,\mathrm{meV}$ and $K = 0.0065\,\mathrm{meV}$, with the experimental saturation magnetization of $M = 6.82\,\mu_\mathrm{B}$. These results indicate that $12K < J_\perp$ and, therefore, that the spin-flop, rather than the spin-flip case is realized in $EuFe_2As_2$.

From the calculated energy difference $dE$ in Eq. (6.16) and the domain distribution the minimum (maximum) in MS (MR) or field-dependent neutron data between 0.4 T to 0.6 T can be associated with $H_a^{\mathrm{flop}}$. The field, at which $|dE|$ reaches its first maximum, is close to the field $H_a^{\mathrm{flop}}$, where the amount of a-twins has a minimum (Fig. 6.20a). Thus, we can identify $H_a^{\mathrm{flop}}$ with this minimum and have another means of determining $J_\perp$ and $K$:

$$J_\perp = \frac{M}{4} \frac{2H_1^2 - \left(H_a^{\mathrm{flop}}\right)^2}{\sqrt{2\left[H_1^2 - \left(H_a^{\mathrm{flop}}\right)^2\right]}}$$
$$K = \frac{M}{16} \frac{\left(H_a^{\mathrm{flop}}\right)^2}{\sqrt{2\left[H_1^2 - \left(H_a^{\mathrm{flop}}\right)^2\right]}}. \tag{6.19}$$

The MR data by Zapf *et al.* [156] show $H_a^{\mathrm{flop}} = 0.37\,\mathrm{T}$ and $H_1 = 0.64\,\mathrm{T}$ (both corrected for the observed hysteresis). This yields $J_\perp = 0.091\,\mathrm{meV}$ and $K = 0.0093\,\mathrm{meV}$, which is in agreement with the previous estimate. The results from various samples and measurement techniques are summarized in Tab. 6.1. While the results differ between different preparation methods and batches, $J_\perp$ appears to be consistent between measurements and within the same sample batch. The biquadratic coupling term is statistically more dispersed, because the analytical expressions for $K$ are more sensitive to the input fields than the expressions for $J_\perp$ and hence small but unavoidable reading errors affect the results more severely. The averaged results are $J_\perp = 0.122(23)\,\mathrm{meV}$, $K = 0.0077(33)\,\mathrm{meV}$

and $J_\perp/K \approx 18(6)$, which supports the claim that the spin-flop scenario generally seems to apply to $EuFe_2As_2$.

### 6.4.2 Twin Population and Detwinning Barrier

In order to determine the energy barrier $\Delta$ associated with detwinning, the twin population $n$ needs to be extracted from experiment first. It can most directly be calculated from the neutron diffraction data, as we have seen above (Fig. 6.18). Figure 6.20(a) shows $n$ as determined from the neutron data for increasing field together with the calculated $dE$ [Eq. (6.16)]. The red solid line shows the result of the fit [Eq. (6.17)] to the data. The fit describes the data well and a value of $\Delta = 6.7\,\mu\text{eV/f.u.}$ is in very good agreement with the estimates at the beginning of this chapter. The initial twin distribution of $n_0 = 0.506$ reflects the fact that this sample was fully twinned after ZFC.

Another way to determine $n$ is from the MS data. The MS is defined by $\Delta L/L_0 = (L(H) - L_0)/L_0$, with length change $\Delta L$ and initial length $L_0$. We can express the average length of a unit cell using $n$ by $L(H) = n(H) \cdot a + [1 - n(H)] \cdot b$ and hence:

$$n(H) = \frac{\Delta L}{L_0}\left(\frac{b}{a-b} + n_0\right). \tag{6.20}$$

Consequently we find:

$$n_0 = \frac{a \cdot n - b(n + \Delta L/L_0)}{(a-b)(1 + \Delta L/L_0)}.$$

From the neutron data we know that $n(H_a^{\text{flop}}) < 0.07$. However, due to the pressure from the dilatometer, which is parallel to the field direction, the degree of detwinning will likely be even higher in this case. By assuming $n(H_a^{\text{flop}}) = 0$, we fix $n_0$, and the MS data is now easily converted into the twin domain population. The result for decreasing

TABLE 6.1: Coupling constants determined from various samples and experiments, including magnetization $M(H)$, magnetoresistance MR, magnetostriction MS, and neutron diffraction. Equal index numbers in the Flux Method column indicate samples from the same batch. The Ratio column refers to $J_\perp/K$.

| Sample | Measurement Technique | Synthesis Method | Constants [meV] | | |
|---|---|---|---|---|---|
| | | | $J_\perp$ | $8K$ | Ratio |
| 1 | $M(H)$ | Fe-As[1] | 0.096 | 0.052 | 14.8 |
| 1 | $MR$ | Fe-As[1] | 0.091 | 0.036 | 20.0 |
| 2 | $MS$ | Fe-As[4] | 0.157 | 0.06 | 20.4 |
| 3 | $M(H)$ | Sn-flux[2] | 0.113 | 0.032 | 28.0 |
| 4 | neutron | Sn-flux[2] | 0.115 | 0.056 | 16.4 |
| 5 | $MR$ | congruent | 0.130 | 0.092 | 11.2 |
| 6 | $MR$ | Fe-As[3] | 0.142 | 0.052 | 21.6 |
| 7 | $MR$ | Fe-As[3] | 0.135 | 0.108 | 9.8 |

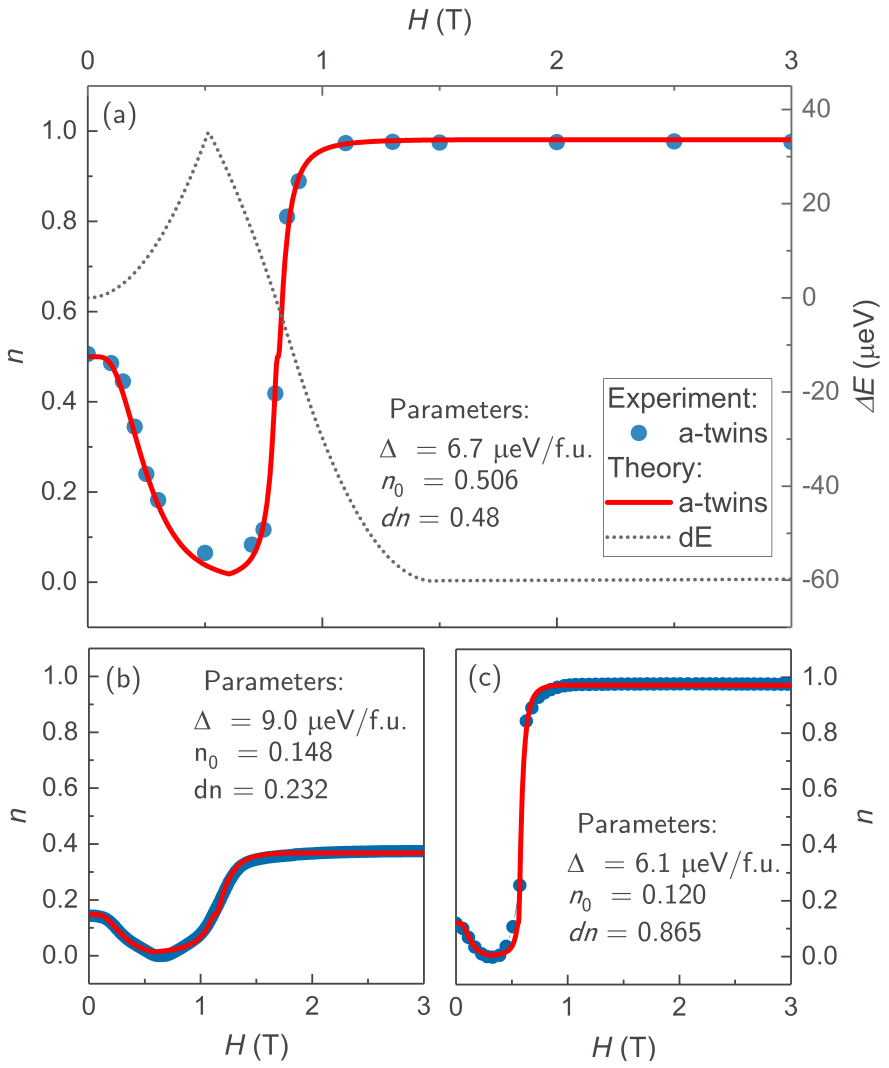


FIGURE 6.20: Fit (solid line) to the experimentally extracted a-twin domain distribution $n$ (solid symbols) as a function of applied magnetic field of the (a) neutron diffraction data shown together with the calculated domain energy difference $dE$ (dotted line) and (b) magnetostriction and (c) magneto-transport data.

field is depicted in Fig. 6.20(b). The effect of the dilatometer pressure is clearly seen by the small values in the saturated regime, where $n$ barely reaches 40 %. After the field is removed again, the sample stays partially detwinned with $n_0 \approx 0.15$. The obtained value for $\Delta$ is 9.0 μeV/f.u. in this case.

The domain distribution can even be extracted from the MR data, because the intrinsic resistivity of the individual twin domains is anisotropic. In general, the relation between the MR and the twin distribution is nonlinear and requires solving the percolation problem. However, since the intrinsic anisotropy is relatively small, this relation can be linearized as if individual domains were connected in series. With this in mind, the MR can be converted to $n(H)$, by using $n_{\mathrm{sat}} = n(H > H_1) = 0.976$ from our neutron data. The MR data in Fig. 6.15(a) was recorded with the current perpendicular to the field

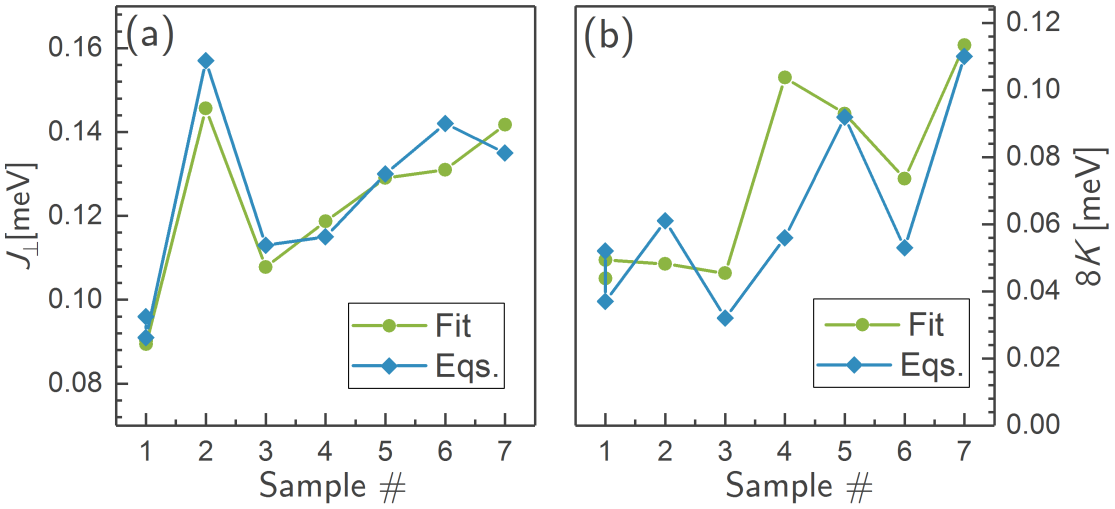


FIGURE 6.21: Comparison of the coupling constants $J_\perp$ and $K$ as determined from Eqs. (6.18-6.19) and from the fit to the domain distribution for various $EuFe_2As_2$ single crystals.

direction, such that it predominantly depicts the distribution of b-twins. In this case, $n$ can be calculated by shifting and rescaling the MR data according to

$$n(H) = \left(1 - \frac{R(H) - R(H_b^{\mathrm{sat}})}{R(H_a^{\mathrm{flop}}) - R(H_b^{\mathrm{sat}})}\right) \cdot n_{\mathrm{sat}}.$$

A value of $\Delta = 6.1\,\mu\mathrm{eV/f.u.}$ is obtained from the data for decreasing field shown in Fig. 6.20(c).

One feature, which is not found in the experiments, is the s-shaped irregularity at the inflection point of $n$ around 1 T ($H_1$), as seen in Fig. 6.20(a+b). This feature can be traced back to the distribution function that models $\Delta$. It occurs when $\Delta$ is large compared to $K/J_\perp$ (see Fig. 6.9a+b). This indicates that the log-normal distribution does not seem to accurately model the distribution $\Delta$ in this parameter range. One reason for this might be the fact that the log-normal distribution is only defined for positive $x$, while the ratio $\Delta/dE$ changes sign due to the field-dependent evolution of $dE$. This problem was circumvented by defining the fit function in a piecewise manner. However, strictly speaking, this approach is hard to justify physically for the log-normal distribution. Therefore, a distribution function that is symmetric around zero might be more suitable to describe the twin distribution of $EuFe_2As_2$. One such function is the Laplace distribution:

$$f_X(x) = \frac{1}{2b} \exp\left(-\frac{|x-\mu|}{b}\right),$$

which has the following CDF

$$F_X(x) = \frac{1}{2} + \frac{1}{2}\,\mathrm{sgn}(x-\mu)\left[1 - \exp\left(-\frac{|x-\mu|}{b}\right)\right].$$

Here, $\mu$ and $b$ are real valued location and scaling parameters. Preliminary testing indicates that this function seems to describe $\Delta$ better, particularly at large $\Delta/(K/J_\perp)$. However, a more detailed investigation, which goes beyond the scope of this thesis, is necessary to clarify this point conclusively.

The values of $J_\perp$ and $K$ obtained from the fit and from Eqs. (6.18-6.19) agree well with each other (Fig. 6.21), indicating that both methods can be used to extract the coupling constants.

### 6.4.3 Consistency Check

The derived averaged constants allow us to calculate the detwinning fields using the respective expressions obtained theoretically (Tab. C.1). The results are with $H_1 = 0.85\,\mathrm{T}$ and $H_2 = 35\,\mathrm{T}$ in excellent agreement with the experimental observations.

Furthermore, we can also calculate the first (kinetic) detwinning field from the condition $dE = \Delta$ through

$$H_0 = \frac{2}{M}\sqrt{2\Delta(J_\perp + 4K)}.$$

The determined energy barrier ranges roughly from $1\,\mu\mathrm{eV}$ and $10\,\mu\mathrm{eV}$, which yields values between $H_0 = 0.01\,\mathrm{T}$ and $H_0 = 0.28\,\mathrm{T}$. These values also fit the experimental observations very well.

Another means of checking the theory for consistency would be to calculate a field-dependent physical property, such as the magnetization along the $[1\,1\,0]_\mathrm{T}$ direction and compare the result to the experiment. The magnetization is composed of the sublattice magnetization of the twin domains weighed by the domain distribution, i. e.

$$M(H) = n(H)\cdot M_a + [1 - n(H)]\cdot M_b,$$

where $M_a$ and $M_b$ are each given by $M\cos\varphi$. This yields

$$M_a = \begin{cases} 0, & \{0, H_a^{\mathrm{flop}}\} \\ \frac{M^2 H}{4(J_\perp - 4K)}, & \{H_a^{\mathrm{flop}}, H_a^{\mathrm{sat}}\} \\ M, & \{H_a^{\mathrm{sat}}, \infty\} \end{cases}$$

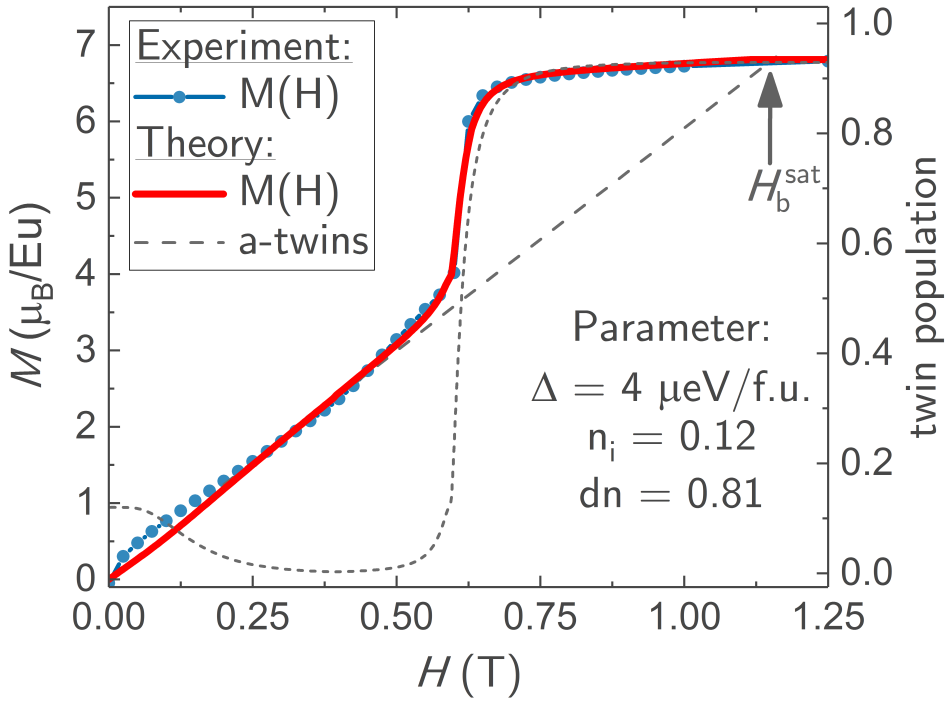


FIGURE 6.22: Magnetization at $T = 5K$ as a function of decreasing magnetic field applied along the $[110]_T$ direction (blue symbols) measured on the same sample as used by Zapf *et al.* [156]. The solid line (red) represents our theoretical prediction using previously determined coupling constants. The dashed line depicts the a-twin domain distribution (right $y$-axis) derived from the fit to the corresponding magneto-resistance data, similar to Fig. 6.15. The dotted line indicates the extrapolation of $H_b^{\mathrm{sat}}$.

and

$$M_b = \begin{cases} \frac{M^2 H}{4(J_\perp + 4K)}, & \{0, H_b^{\mathrm{sat}}\} \\ M, & \{H_b^{\mathrm{sat}}, \infty\}, \end{cases}$$

corresponding to a continuous magnetization for the b-twin and a discontinuous for the a-twin, in agreement with the textbook description of a metamagnetic spin-flop transition. Using $\Delta = 4\,\mu\mathrm{eV/f.u.}$, $n_i = 0.22$, and $dn = 0.71$ for the sample from Fig. 6.19, the twin distribution $n(H)$ can be calculated. The corresponding terms were then combined numerically to get the total magnetization. The result is depicted together with the experiment in Fig. 6.22.

The calculated magnetization reproduces the experiment well over the entire field range, except perhaps at very small fields. In particular, the evolution around the $H_1 = 0.62\,\mathrm{T}$ is captured accurately. The derived twin distribution is shown by the dashed line for reference. This proves that the jump in $M(H)$ is in fact due to domain reorientation and not an intrinsic spin-flip as proposed earlier [156].

## 6.5 Summary

In this chapter I have, discussed the multistage magnetic detwinning of $EuFe_2As_2$. After motivating the Hamiltonian [Eq. (6.3)], in the first part of this chapter, we have calculated the domain energies of the b-twin and a-twin upon application of an in-plane magnetic field along the principal axes. While the b-twin shows a linear spin susceptibility, the a-twin exhibits a highly non-linear magnetization, due to the occurrence of meta-magnetic transitions for Eu and Fe spins.

Combining the findings for the individual twin domains revealed rather complicated domain dynamics, considering the physical simplicity of our model. Over the entire field range four phases could be identified (Fig. 6.6). Two b-twin phases occur, one at small and one at higher fields, due to spin canting of the Eu and Fe spins, respectively. Two other phases favor the a-twin domains, due to the meta-magnetic transitions. The first one occurs at intermediate fields between $H_1$ (or $H_1^{\mathrm{sat}}$, depending on $K/J_\perp$) and $H_2$, while the second one, not experimentally confirmed phase at this point, occurs above $H_3$.

After discussing the domain dynamics in detail (Fig. 6.7), a full map of the domain energy difference $dE = E_{\text{a-twin}} - E_{\text{b-twin}}$, the driving force behind the detwinning, was presented.

Based on the assumption that the energy barrier for domain conversion $\Delta$ is distributed in a log-normal fashion, a fit function for the domain distribution $n$ was introduced and its theoretical evolution derived (Fig. 6.9). Furthermore, three different estimates for $\Delta$ are given, which suggest that $\Delta$ is of the order of 10 µeV/f.u in the 122-type iron pnictides.

Experimental evidence for the multistage magnetic detwinning effect (MMDE) was presented in the second part of this chapter. Distinct signatures of the MMDE were observed in various measurements, such as measurements of the electrical transport, thermal expansion, magnetostriction, neutron diffraction and magnetization. While the "static" measurements, like TE and $\rho(T)$ revealed the effect of FT and its temperature dependence, the field-dependent data of the MR, MS and neutron diffraction uncovered the detwinning dynamics during FT. Signatures of three of the four predicted phases ($H_0$, $H_1$ and $H_2$) were observed in experiment. However, the fourth phase connected to $H_3$ was not expected to be observed, due to the very large predicted field of $\sim 130$ T.

Depending on the angle between electrical current $I$ and the applied magnetic field $H$ in the MR, the dynamics of either the b-twin domains ($I \parallel H$) or the a-twin domains ($I \perp H$) were observed. Furthermore, measurements under an angle of 45°, i. e. along

the $\langle 1\,0\,0\rangle_T$ equivalent directions, revealed that virtually no MMDE occurs, due to the fact that both twin types are energetically equivalent. This was corroborated by the absence of any irreversible behavior in the magnetization in the same configuration.

Upon increasing temperature, the MMDE changed qualitatively. Above $T_{Eu}$, it was replaced by a one-step process that favored the a-twin phase. The PM state of the $Eu^{2+}$ moments could be identified as the cause for this behavior, because no spin-flop occurs in the PM state. At even higher temperature, the one-step process eventually vanishes, as thermal energy becomes the dominating energy scale, effectively reducing the applied field.

In the last section of this chapter theory and experiment were quantitatively combined to determine the coupling constants $J_\perp$ and $K$ as well as the detwinning barrier $\Delta$. The former two were first calculated from theory-based analytical expressions and from characteristic field values observed in field-dependent experiments. Afterwards, the a-twin domain distribution $n$ was derived from neutron, MS, and MR data. Subsequently a fit to the twin distribution could successfully deliver $\Delta$ and also independently confirm the previously determined values of $J_\perp$ and $K$. The values varied to a certain extend, due to the observed sample dependence and varying measurement techniques, but were overall in good agreement with each other. In particular, the values of $\Delta$ agree well with the estimates given in the first section of this chapter.

The section concluded with a consistency check of the detwinning theory. Using the extracted parameters, the theory could accurately reproduce the observed detwinning fields, not only for $EuFe_2As_2$, but also for $BaFe_2As_2$ ($H_2$). Furthermore, and perhaps most convincingly, the theory could closely model the recorded magnetization with $H \parallel [1\,1\,0]_T$, supporting not only the microscopic aspects of the theory, but also the modeling of $\Delta$. However, even though the modeling of $\Delta$, using the log-normal distribution, described the experimental data generally well, the Laplace distribution was proposed as a possible alternative, because it does not feature the unphysical s-shaped irregularity at $H_1$ that develops for large values of $\Delta/(K/J_\perp)$.

Chapter 7

# Magnetic Detwinning in Doped $EuFe_2As_2$

In this chapter, I will briefly discuss the evolution of the multistage magnetic detwinning in doped $EuFe_2As_2$, as it can be traced by electrical transport, and in the case of $Eu(Fe_{1-x}Ru_x)_2As_2$, also by magnetostriction and magnetization measurements. I will focus on diluting the $EuFe_2As_2$ magnetism, first via replacing Eu with Ba and then by substituting Fe with Ru. Furthermore, the $EuFe_2(As_{1-x}P_x)_2$ systems will also be presented. Replacing As with the smaller P induces a significant chemical pressure effect, while leaving the magnetic subsystems intact.

## 7.1 Dilution of Eu-Moments: $Eu_{1-x}Ba_xFe_2As_2$

Upon Ba-doping on the Eu site, the ordering temperatures $T_{Fe}$ and $T_{Eu}$ reduce. For a nominal doping concentration of $x = 0.1$, the reduction is about 5 % in both transitions, as evidenced by measurements of the electrical resistivity (Fig. 7.1a). After zero-field cooling (ZFC) the sample exhibits a substantial increase of $\rho$ at $T_{Fe}$. Field treatment (FT) at 5 K once with the electrical current $I$ parallel and perpendicular to the applied field $H$, appears to result in a significant detwinning effect, as the resistivities predominantly along the $b$-axis ($\rho_b$) and $a$-axis ($\rho_a$) are resolved. However, a sharp (but diminished) increase of $\rho_a(T_{Fe})$ is still visible, which might indicate that the sample remains partially twinned (see also the discussion in Chapter 5).

FT still reveals a significant detwinning effect even when half the $Eu^{2+}$ moments are nominally replaced with Ba (Fig. 7.1b), even though no clear signatures of the $Eu^{2+}$ ordering are observed at low temperatures. At this concentration, the $Eu^{2+}$ moments are likely in a spin-glassy state, as discussed above in Chapter. 5. The overall magnitude of the detwinning effect is slightly reduced compared to smaller doping concentrations,

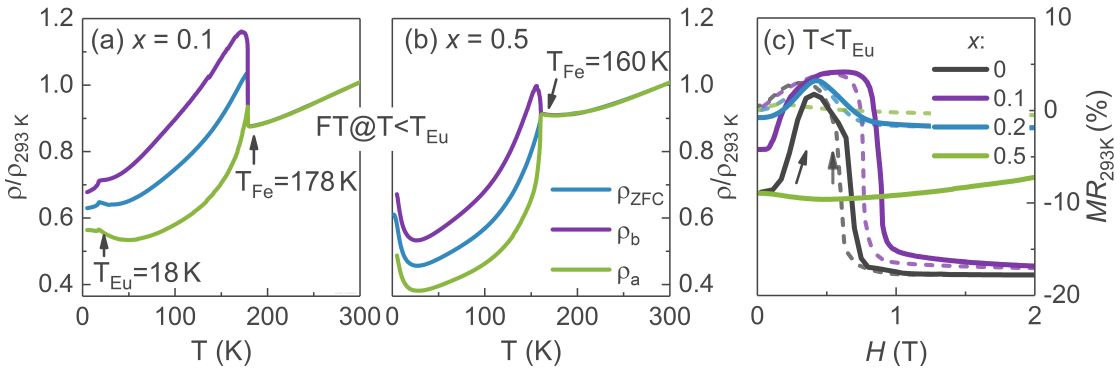


FIGURE 7.1: Transport data for $Eu_{1-x}Ba_xFe_2As_2$ with the current $I$ flowing along the in-plane $[1\,1\,0]_T$ direction. (a) Normalized resistivity for $x = 0.1$ and (b) $x = 0.5$ after ZFC (twinned) and FT at $T = 5\,K < T_{Eu}$. The configurations $I \parallel H$ and $I \perp H$ correspond to the resistivities predominantly along the $b$-axis ($\rho_b$) and $a$-axis ($\rho_a$). (c) Magnetoresistance $MR_{293\,K}$ at $T = 5\,K < T_{Eu}$ for various $x$ after ZFC for increasing (solid lines) and decreasing (dashed lines) field.

but the qualitative behavior stays the same. Only the behavior of the sharp increase in $\rho_a$ at $T_{Eu}$ differs. While this increase is still clearly visible in the sample with $x = 0.1$, it is absent in the resistivity curve $\rho_a$ of the sample with $x = 0.5$, indicating that this sample shows a higher degree of detwinning than the sample with $x = 0.1$. This is an unexpected observation.

The magnetoresistance (MR) can again give insight into the dynamics during FT. The general trend is a reduction of the MR and, in particular, the two-step detwinning process with increasing doping concentration (Fig. 7.1c). However, the sample with $x = 0.1$ exhibits an increase of the characteristic fields, i. e. the maximum and the transition at $H_1$ by roughly 0.2 T. The maximum, which was earlier connected to $H_a^{flop}$, broadens significantly, while the jump at $H_1$ does not change much in magnitude. The sample with $x = 0.2$ exhibits a MR with values of $H_a^{flop}$ and $H_1$ comparable to $EuFe_2As_2$, but with significantly reduced magnitude. Increasing $x$ to 0.5 virtually removes these features from the MR.

Nonetheless, the initial curve after ZFC (solid line) still exhibits a distinct irreversible one-step detwinning process. In this sense the dilution of Eu with Ba has a similar effect on detwinning as FT of $EuFe_2As_2$ above $T_{Eu}$, likely because both disturb the ordering of the $Eu^{2+}$ moments. Interestingly, the one-step process for highly Ba-doped $EuFe_2As_2$ does still favor b-twins and not a-twins, as was the case for FT of $EuFe_2As_2$ above $T_{Eu}$ (Fig. 6.14b).

Furthermore, a large difference $\Delta R_0 = |R_i(H = 0) - R_f(H = 0)|$ between the initial resistance after ZFC, $R_i$ and the final resistance after FT, $R_f$ at $H = 0$ is observed. While the samples with $x = 0.1$ and $x = 0.2$ exhibit diminished values of $\Delta R_0$ (4,% and

1 %, respectively), $\Delta R_0 = 9\,\%$ in the sample with $x = 0.5$ is as large as in the undoped sample.

In the case of Ba-doping, we can assume that the intrinsic resistivity anisotropy $\rho_b/\rho_a$ does not change much, since the FeAs planes—which account for most of the electrical transport in the IBSCs—are not directly altered by this substitution. Thus, we should be able to take $\Delta R$ as a rough measure for the persistent degree of detwinning, at least for relative changes. Therefore, we must conclude that the degree of persistent detwinning does in fact first decrease and then unexpectedly increases with Ba-concentration. This behavior is also consistent with the observed anisotropy in the resistivity (Fig. 7.1a+b).

## 7.2 Dilution of Fe-Moments: $Eu(Fe_{1-x}Ru_x)_2As_2$

Ru-doping on the Fe site is an effective dilution of the Fe-subsystem. Despite the slightly larger size of Ru, a significant reduction of the $c$-axis was found, as discussed in Chapter. 5.

The electrical resistivity reveals that a small substitution of about 7.5 % has not only a large effect on $T_{Fe}$, which is significantly suppressed, but also on the magnetic detwinning effect after FT (Fig. 7.2). If performed below $T_{Eu}$, the temperature which is less affected by the small substitution than $T_{Fe}$, some anisotropy can still be uncovered, albeit it is

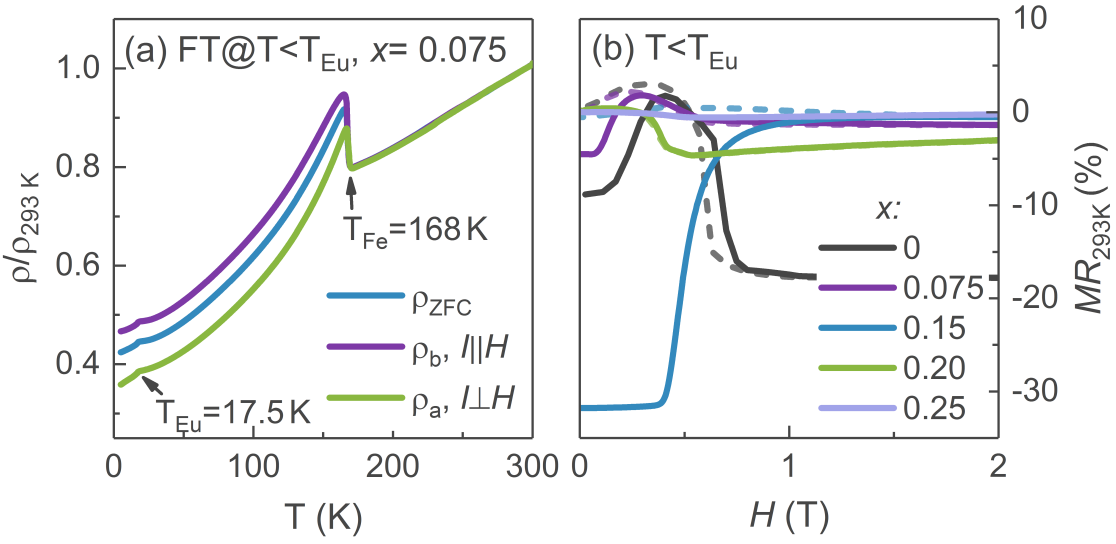


FIGURE 7.2: Transport data for $Eu(Fe_{1-x}Ru_x)_2As_2$, with current $I$ flowing along the in-plane $[1\,1\,0]_T$ direction. (a) Normalized electrical resistivity for $x = 0.075$ after ZFC (twinned) and FT at $T = 5\,K < T_{Eu}$. The configurations $I \parallel H$ and $I \perp H$ correspond to the resistivities predominantly along the $b$-axis ($\rho_b$) and $a$-axis ($\rho_a$). (b) Magnetoresistance $MR_{293\,K}$ at $T = 5\,K < T_{Eu}$ for various $x$ after ZFC for increasing (solid lines) and decreasing (dashed line) field.

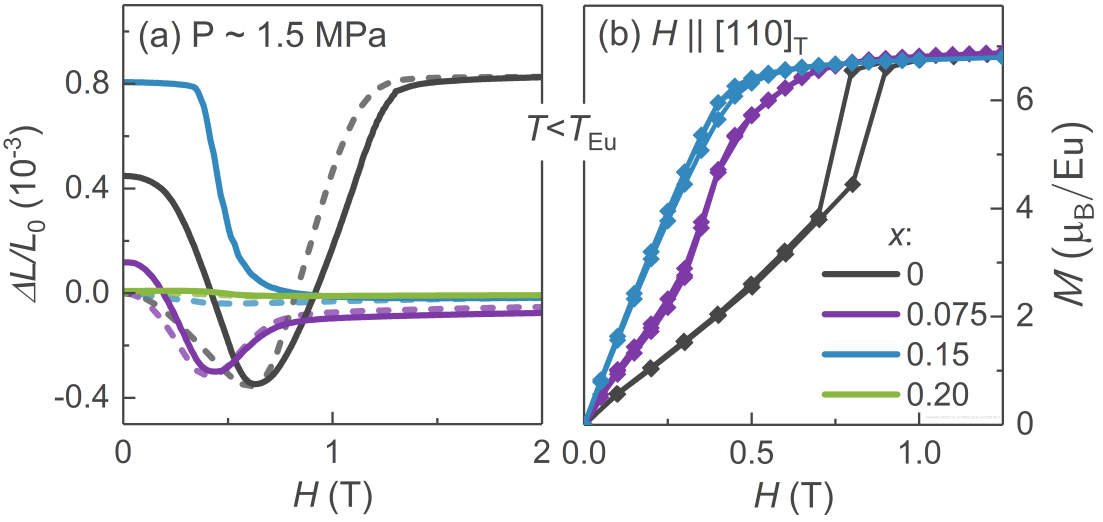


FIGURE 7.3: Additional measurements on $Eu(Fe_{1-x}Ru_x)_2As_2$ for various $x$ after ZFC and at $T = 5\,\mathrm{K} < T_{\mathrm{Eu}}$. (a) Magnetostriction $\Delta L/L_0$ for increasing (solid lines) and decreasing (dashed line) field. Pressure $P$ and field $H$ were along $[1\,1\,0]_{\mathrm{T}}$. (b) Magnetization as a function of applied magnetic field $H \parallel [1\,1\,0]_{\mathrm{T}}$.

much less pronounced than in the case of $EuFe_2As_2$. The ZFC measurements is not located exactly in the middle between the two FT curves, but is slightly closer to the $\rho_b$ curve. Above $T_{\mathrm{Eu}}$, FT has virtually no effect on the in-plane resistivity (not shown).

Ru substitution results in a fast reduction of the MR signal with increasing doping. Generally, the irreversible behavior ($\Delta R_0$) induced after FT decreases compared to the undoped reference sample, as was the case in the previous doping series. The two-step process is almost gone for the sample with $x = 0.15$. Yet, this sample exhibits an exceptionally large $\Delta R_0$, not following the trend of its predecessors. The change in the MR is roughly three times as large as in the undoped sample. With further increase of the Ru-concentration the signature of the MR changes, once the system starts to become superconducting (see also Fig. 5.10). No irreversible behavior is observed anymore and the MR is initially zero for the samples with $x = 0.2$ and $x = 0.25$. The sudden step to negative values in the $x = 0.2$ sample could be due to a magnetically induced suppression of the SC state. However, this seems not very likely, because the sample does not show zero resistance at 5 K. Also a similar step in the sample with $x = 0.25$ is virtually absent.

Measurements of the thermal expansion (TE; Fig. 7.3a) generally confirm the above considerations. The two-step detwinning process reduces with doping and so does the irreversible behavior induced after FT. The sample with $x = 0.15$ is again the exception to this trend. However, in the case of the MS the effect is less pronounced, as the difference between the initial ZFC value and the value after FT is only about twice as large as the MS of the undoped sample, which is again shown for reference. This reduction

can be attributed to the pressure from the dilatometer (see also Fig. A.5). Additionally, measurements of the in-plane magnetization (Fig. 7.3b) confirm the suppression of the multistage detwinning as $H_1$ reduces with doping until the signature is gone in the sample with $x = 0.15$.

## 7.3 Chemical Pressure: $EuFe_2(As_{1-x}P_x)_2$

Phosphorous doping on the As site does not dilute any of the magnetic sub-systems in $EuFe_2As_2$, but has a strong chemical pressure effect. As a consequence, the $c$-axis shrinks with doping as well, while, in particular, the Fe-subsystem is not influenced directly. Therefore, it is a suitable system to investigate whether the reduction of the multistage detwinning effect results mainly from the dilution of the Fe-moments or also as a function of the $c$-parameter.

The electrical resistivity of the sample with $x = 0.05$ after ZFC (Fig. 7.4a) is very similar to the Ru-doped sample with $x = 0.075$ introduced in the last section. All transitions are similarly reduced in temperature, only the residual resistivity is slightly smaller than in the case of Ru-doping. FT, in the typical manner with $I \parallel H$ and $I \perp H$ below $T_{Eu}$, can induce some anisotropy, again with a similar magnitude as in the Ru-doped sample with $x = 0.075$. FT above $T_{Eu}$ has also no effect on the resistivity, neither in the $I \parallel H$ nor in the $I \perp H$ configuration (not shown). Therefore, we can conclude that the sample with

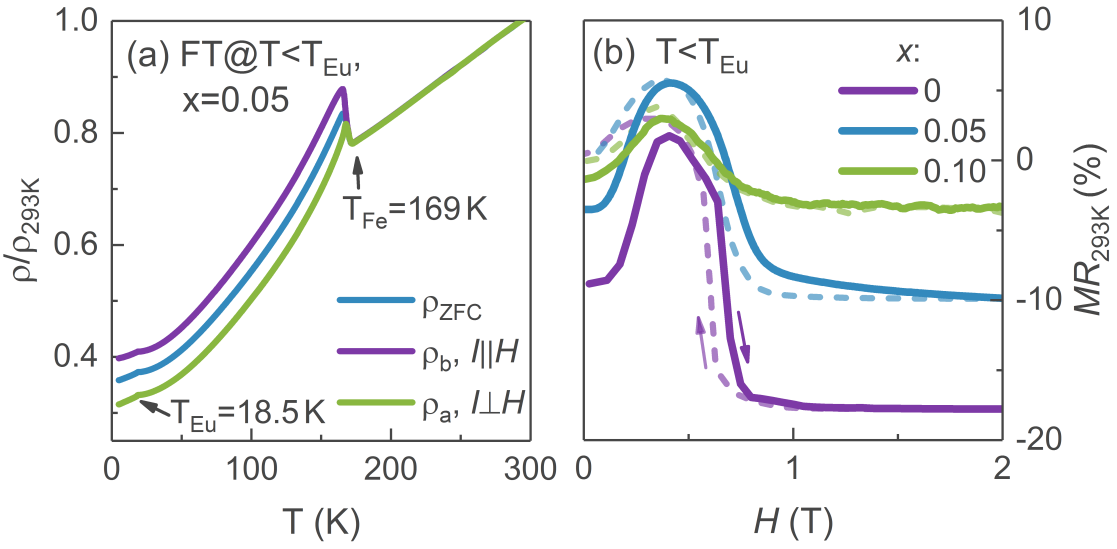


FIGURE 7.4: Transport data for $EuFe_2(As_{1-x}P_x)_2$, with the current $I$ flowing along the in-plane $[1\,1\,0]_T$ direction. (a) Normalized electrical resistivity for $x = 0.05$ after ZFC (twinned) and FT at $T = 5\,K < T_{Eu}$. The configurations $I \parallel H$ and $I \perp H$ correspond to the resistivities predominantly along the $b$-axis ($\rho_b$) and $a$-axis ($\rho_a$). (b) Magnetoresistance $MR_{293\,K}$ at $T = 5\,K$ for various $x$ after ZFC for increasing (solid lines) and decreasing (dashed lines) field.

$x = 0.05$ exhibits virtually the same detwinning behavior in the electrical resistivity as the Ru-doped sample with $x = 0.075$.

The situation in the MR (Fig. 7.4b) is somewhat different than in the case of Ru-doping. Below $T_{\mathrm{Eu}}$, the overall magnitude decreases slower with doping than in the Ru-doped case. The initial curve after ZFC $\Delta R_0$ decreases continuously. It changes from 9 % over 3.5 % to roughly 1 % in the sample with $x = 0.1$. However, as P doping does indirectly affects the FeAs layers and, in particular, the electronic structure (see Chapter 4), we must assume that $\Delta R_0$ might not be a reliable way to measure the persistent detwinning effect in this system. Interestingly, in contrast to Ba-doping and Ru-doping the characteristic fields $H_a^{\mathrm{flop}}$ and $H_1$ are not much affected by P-doping.

A similar trend was also observed in measurements of the MS on samples with $x = 0.07$ and $x = 0.14$ in Ref. [185, Fig. 4.34].

## 7.4 Conclusion & Summary

We have seen that diluting the magnetic subsystems by Ba and Ru is detrimental to the magnetic detwinning effect. In the case of Ba doping this underscores the importance of Eu spins in the detwinning process. The magnetic detwinning signatures also diminish with dilution of the Fe-subsystem. Both effects can be expected from our detwinning theory. However, the interpretation of the effects of Ru-doping are not as straightforward as in the case of Ba-doping. This becomes evident when considering P-doping on the As site. Although none of the magnetic subsystems are diluted, the multistage detwinning effect still diminishes significantly.

While the multistage detwinning process visible in MR data diminishes in all presented doping series with increasing $x$, the initial detwinning at $H_0$ exhibits exceptions to this trend. In particular, the samples with $x = 0.15$ in the Ru-series and $x = 0.5$ in the Ba-series reveal unexpectedly large detwinning signatures, which cannot be explained withing the presented paradigm. A more in-depth investigation, including more samples in the vicinity of the respective concentrations, is necessary to determine, whether this is in fact intrinsic behavior of the system or not.

The above observations are backed by the evolution of the coupling constants $J_\perp$ and $K$ (Fig. 7.5). The overall trend is a reduction of both parameters with doping. Ba substitution shows the most gradual reduction and leads to a biquadratic coupling, which is virtually zero for the sample with $x = 0.5$. Although $J_\perp$ decreases also for Ru-doping initially, the AF coupling of the $Eu^{2+}$ moments seems to be stabilized for larger doping concentrations.

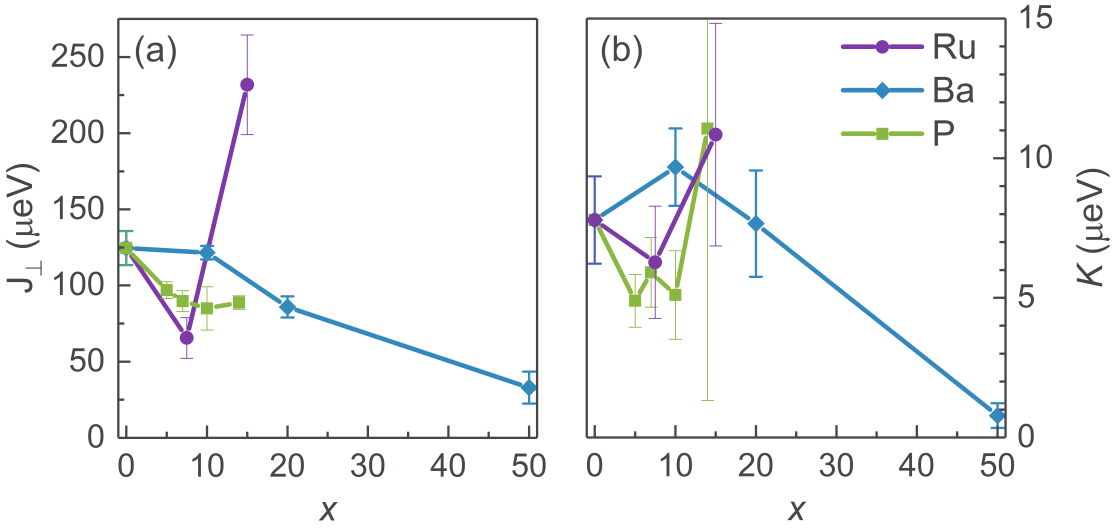


FIGURE 7.5: Evolution of the coupling constants (a) $J_\perp$ and (b) $K$ with doping concentrations $x$ for all discussed substitutions. Values for $EuFe_2(As_{1-x}P_x)_2$ with $x = 0.07$ and $x = 0.14$ determined from data extracted from Ref. [185].

It is rather difficult to make more robust statements from the observed experiments. The coupling constants depend on the overlap of the respective orbitals. In particular, the biquadratic coupling $K$ is sensitive to this and the overlap of the Eu and Fe orbitals is generally small. The presented dilutions of the magnetic subsystems also lead to a change in the lattice parameters, in particular in the $c$-parameter and, therefore, have an impact on the overlap of these orbitals. This impact is most prominently seen in the P-doping series, which shows significant electronic changes (see Chapter 4.7), although no dilution of magnetic moments occur. It is, therefore, difficult to separate the two effects on the magnetic detwinning.

Although the presented data give clear indications for a reduction of the multistage magnetic detwinning effect, a more detailed investigation, including additional first-principles calculations, is necessary to gain a better microscopic understanding of the evolution of the magnetic detwinning effect in doped Eu-based iron pnictides.

Chapter 8

# Summary

In order to understand the physics of the iron-based superconductors (IBSCs), it is important to investigate the unusual symmetry-breaking antiferromagnetic (AF) ground state of the parent compounds of the IBSCs that develops at low temperatures. In particular, the investigation of the resulting in-plane anisotropy and the related electronic nematic state is deemed crucial, as superconductivity arises out of this state. However, access to the anisotropy is obstructed by the formation of structural twin domains in the same state. These domains are typically removed by the application of uniaxial pressure of the order of 20 MPa within the orthorhombic basal plane. Unfortunately, besides being technically challenging to implement in a cryogenic environment, uniaxial pressure acts as an external symmetry-breaking force, which has to be carefully considered when interpreting data, thus further complicating the investigation. Detwinning by application of magnetic field does not have the aforementioned disadvantages, but is reported to work only in very high fields of the order of 30 T. Therefore, our discovery of a persistent multistage magnetic detwinning effect in $EuFe_2As_2$, which sets in at minuscule magnetic fields of the order of 0.1 T, was highly unexpected.

For the investigation of the Eu-based iron pnictides single crystals of the parent compound $EuFe_2As_2$ and two doped variants, i. e. Ru-doped and Ba-doped, were synthesized, while the P-doped samples were already available. In particular, the growth of the undoped and Ru-doped crystals using the UltraLow self-flux method, yielded samples of exceptional size. This is most notably demonstrated by the Ru-doped sample presented in Fig. 3.5(c-d) that has virtually cm-sized dimensions and a mass of almost 1 g. The high quality of the crystals was confirmed using the Laue backscattering technique, x-ray powder diffraction, x-ray spectroscopy, and transport measurements. It is perhaps best represented by the RRR $> 7$ of the magnetically detwinned *as grown* $EuFe_2As_2$ sample (Fig. 6.14a), which is large compared to other as-grown 122 systems.

While the $Eu_{1-x}Ba_xFe_2As_2$ seems to behave like a simple solid solution with indications of spin-glassy behavior of the $Eu^{2+}$ moments at low temperatures and large $x$, the $Eu(Fe_{1-x}Ru_x)_2As_2$ system shows a more complex behavior upon doping in the form of a deviation from Vegard's law above $x = 0.3$ and the emergence of several phases, including a superconducting one (Fig. 5.10).

The main *experimental* result of this work, however, is the observation of the persistent multistage magnetic detwinning effect in $EuFe_2As_2$. Evidenced by both indirect measurements, such as magnetostriction and magnetoresistance, and reinforced by a probe with neutron scattering, this effect is characterized by multiple reorientations of the structural twin domains upon application of an in-plane magnetic field at low temperatures. Depending on the temperature, the material exhibits either a single ($T > T_{\mathrm{Eu}}$) or multiple reorientations ($T < T_{\mathrm{Eu}}$). In the latter case, the system initially favors b-twins above $H_0 \approx 0.1\,\mathrm{T}$, followed by a reorientation to the a-twin phase at $H_1 \approx 0.7\,\mathrm{T}$, before it starts to change back to the b-twin configuration above $H_2^{\mathrm{onset}} \approx 12\,\mathrm{T}$, while the former favors only a-twins in the investigated field range. After removing the field at ($T < T_{\mathrm{Eu}}$), we found that $EuFe_2As_2$ stays partially detwinned with $b \parallel H$ and that the detwinning persists up to the highest temperatures, where the structural phase transition to the tetragonal crystal structure occurs at $T_{\mathrm{Fe}} = 190\,\mathrm{K}$.

This observation is complemented by the main *theoretical* result, namely, the development of a novel microscopic theory that fully and quantitatively describes the observed multistage magnetic detwinning effect. The effect occurs due to the presence of the two magnetic subsystems in $EuFe_2As_2$, i. e. the Eu and Fe moments, and due to their intricate interplay. Through this interplay the Eu moments ($L = 0$) can couple indirectly to the lattice via the Fe moments, which leads to the observed detwinning effect. I have argued that the interaction between Eu and Fe moments can not be described in a simple Heisenberg picture, as any bilinear exchange between Eu and Fe sublattices cancels by symmetry. Therefore, the presented theory was based on a biquadratic exchange. Supported by first-principles numerical calculations, this theory can fully describe the system's detwinning behavior.

Combining the newly developed theory with the experimental data allowed me to extract not only the strength of the biquadratic coupling $K$ and the out-of-plane AF coupling between Eu layers $J_\perp$, but also to estimate the strength of the detwinning barrier $\Delta$. The averaged results for the former are $J_\perp = 0.122(2)\,\mathrm{meV}$ and $K = 0.0077(33)\,\mathrm{meV}$, while the latter is roughly of the order of $0.01\,\mathrm{meV}$, assuming a distribution over many domain walls according to the log-normal law. With these parameters, the theory yielded the detwinning fields $H_0 \approx 0.1\,\mathrm{T}$, $H_1 = 0.85\,\mathrm{T}$ and $H_2 = 35\,\mathrm{T}$, which are in excellent agreement with the experiment. Furthermore, in a final consistency check, I was able to

accurately calculate the in-plane magnetization of $EuFe_2As_2$ along $[1\,1\,0]_T$ below $T_{Eu}$, which supports not only the microscopic aspects of the theory, but also the modeling of the energy barrier $\Delta$. Nonetheless, I raised the question, whether the log-normal distribution is appropriate in this case, because for large values of $\Delta/(K/J_\perp)$ the current description results in an unphysical irregularity at $H_1$. I, therefore, proposed an alternative model function based on the Laplace distribution. Preliminary results indicate that this distribution, in fact, seems to model the data even better. However, the analysis needs to be completed before any conclusive statements can be drawn.

In Chapter 7, I briefly discussed the evolution of the multistage detwinning effect and, in particular, the biquadratic coupling, upon various chemical substitutions. In all three doping series, the reversible part of the effect reduces with increasing doping. Although this trend is also visible in the irreversible part, two unexpected exceptions were observed, the $Eu(Fe_{1-x}Ru_x)_2As_2$ sample with $x = 0.15$ and the $Eu_{1-x}Ba_xFe_2As_2$ sample with $x = 0.5$. The general trend of a diminishing magnitude was also, within the estimated error, observed for the extracted coupling constants. While the reduction can be intuitively understood in the case of the magnetically diluted Ru-doped and Ba-doped systems, it is not obvious for the chemically pressurized P-doped system. However, in order to draw more elaborate conclusions further investigation is needed, including not only more data points, but also additional theoretical calculations to gauge, e. g. the doping evolution of the orbital overlap between the localized Eu $4f$ and the more itinerant Fe $3d$ orbitals, as our DFT calculations indicate that the biquadratic coupling is very sensitive to this overlap.

This research project covers a wide range of activities, ranging from single crystal synthesis, over sample characterization, physical measurements to theoretical work and even numerical calculations. I have presented evidence for the highly unexpected physical phenomenon of *persistent multistage magnetic detwinning* in $EuFe_2As_2$, which we discovered during this project. This evidence is not limited to experimental data, but was significantly solidified by the presentation of the novel microscopic theory (and first-principles numerical calculations), which fully and quantitatively explains the entire phase diagram in all its richness and complexity. Therefore, this thesis combines the three major approaches in solid state physics: theoretical, experimental, and computational. With the rigorous framework established here, it provides a solid foundation for future investigations.

Appendix A

# Additional Data & Measurements

## Lattice Parameters

Refined lattice parameters and calculated doping concentrations of Ru-doped (Tab. A.1) and Ba-doped (Tab. A.2) $EuFe_2As_2$ samples as presented in Chapter 5.

TABLE A.1: Refined lattice parameters, unit cell volume $V$, and extracted Ru concentration derived from XRD ($x_{\text{calc}}^{\text{a/c-axis}}$) and EDX ($x_{\text{EDX}}$) data of the $Eu(Fe_{1-x}Ru_x)_2As_2$ series. Data for $x = 1$ are taken from Ref. [150].

| $x$ | $a$-axis [Å] | $c$-axis [Å] | $V$ [Å$^3$] | $x_{\text{calc}}^{\text{a-axis}}$ | $x_{\text{calc}}^{\text{c-axis}}$ | $x_{\text{EDX}}$ |
|---|---|---|---|---|---|---|
| 0 | 3.912(4) | 12.175(12) | 186.3(4) | 0 | 0 | 0 |
| 0.075 | 3.925(4) | 12.106(12) | 186.5(4) | 0.052(21) | 0.049(12) | 0.049(3) |
| 0.15 | 3.945(4) | 11.968(12) | 186.3(4) | 0.132(20) | 0.148(11) | 0.132(9) |
| 0.2 | 3.967(4) | 11.854(12) | 186.5(4) | 0.216(20) | 0.230(11) | 0.203(1) |
| 0.225 | 3.959(4) | 11.895(12) | 186.4(4) | 0.183(20) | 0.200(11) | n/a |
| 0.25 | 3.976(4) | 11.804(12) | 186.6(4) | 0.251(20) | 0.266(11) | 0.307(21) |
| 0.3 | 4.002(4) | 11.67(1) | 186.9(4) | 0.353(19) | 0.361(10) | 0.455(16) |
| 0.35 | 4.041(4) | 11.463(11) | 187.2(4) | 0.506(19) | 0.510(10) | n/a |
| 0.4 | 4.038(4) | 11.487(11) | 187.3(4) | 0.494(19) | 0.492(10) | n/a |
| 0.45 | 4.058(4) | 11.368(11) | 187.2(4) | 0.572(20) | 0.578(10) | n/a |
| 1 | 4.167(4) | 10.778(11) | 187.1(4) | 1 | 1 | 1 |

## Atomic Force Microscopy

Initially, the contacts on the Ru-doped samples were not stable and tended to come loose during transport measurements, as mentioned in Sec. 3.4.2. A possible explanation was

TABLE A.2: Refined lattice parameters, unit cell volume $V$, and extracted Ba concentration extracted from XRD ($x_{\mathrm{calc}}$) and EDX ($x_{\mathrm{EDX}}$) data of the $Eu_{1-x}Ba_xFe_2As_2$ series. Data for $x = 1$ are taken from Ref. [146].

| $x$ | $a$-axis [Å] | $c$-axis [Å] | $V$ [Å$^3$] | $x_{\mathrm{calc}}$ | $x_{\mathrm{EDX}}$ |
|---|---|---|---|---|---|
| 0 | 3.912(4) | 12.175(12) | 186.3(4) | 0 | |
| 0.1 | 3.919(4) | 12.202(12) | 187.4(4) | 0.058(31) | 0.044(7) |
| 0.2 | 3.921(4) | 12.381(12) | 190.3(4) | 0.221(29) | |
| 0.5 | 3.939(4) | 12.659(13) | 196.4(4) | 0.552(26) | |
| 1 | 3.9648(5) | 13.018(2) | 204.64(4) | 1 | |

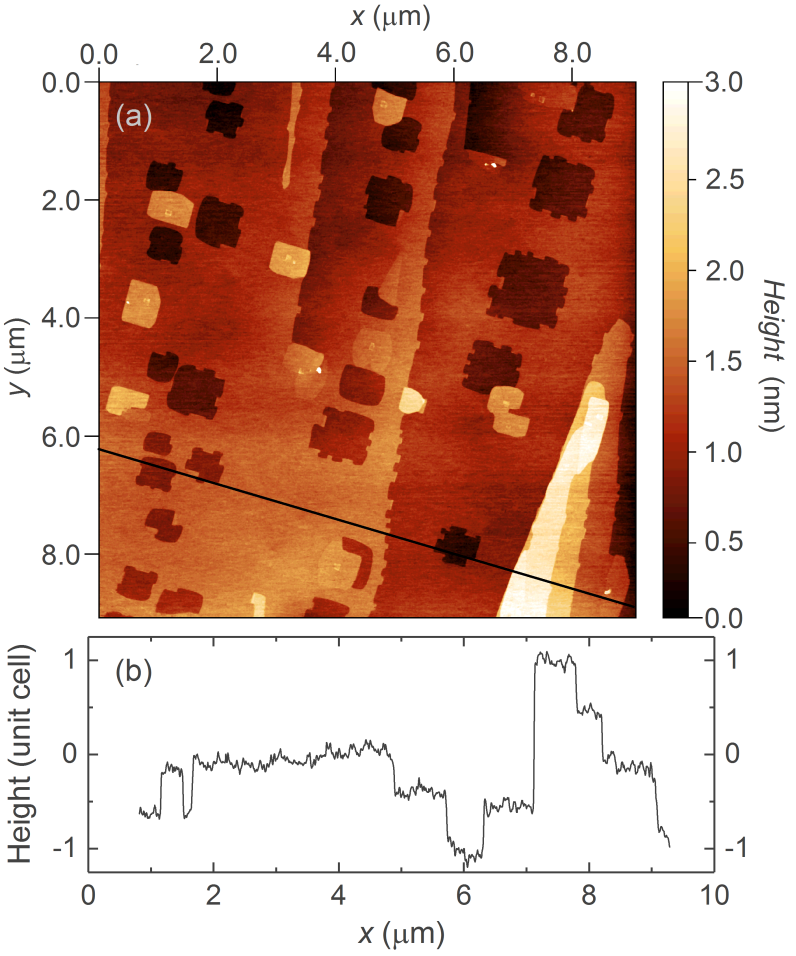


FIGURE A.1: AFM scan. (a) Surface topology of a $Eu(Fe_{1-x}Ru_x)_2As_2$ single crystal with $x = 0.2$. The $c$-axis is perpendicular to the plane of view. (b) Line scan along the black line in (a). The height of the line scan is normalized to the refined $c$-axis parameter of this particular crystal. Jumps of the order of half a unit cell can be resolved. The measurement was conducted by S. Esser.

that the smooth surface together with thermal stresses during temperature sweeps would cause the problem.

Therefore, and in order to quantify the surface roughness, one $Eu(Fe_{1-x}Ru_x)_2As_2$ crystal with $x = 0.2$ was investigated using atomic force microscopy (AFM). Figure A.1 shows the recorded AFM picture. The black line indicates the direction of the line scan shown in Fig. A.1(b). The measurement indeed reveals a very smooth sample surface. With a root mean square (RMS) value of 0.444 nm, the surface roughness is comparable to high-quality substrates, like STO, with a typical RMS value of less than 1 nm [186]. Remarkably, the line scan uncovers that the microscopic surface roughness seems to be entirely determined by the crystallographic c-axis, as only integer "jumps" of half a unit cell height are observed.

## Annealing

In order to study the effect of annealing on the Ru-doped system, two samples were chosen and exposed to a series of heat treatments. Sample 1, with a nominal Ru content of $x_{nom} = 0.15$, was exposed to varying temperatures of 810 °C, 860 °C, and 910 °C, respectively, while the duration was fixed to 3 d. Sample 2, with a nominal Ru composition of $x_{nom} = 0.225$, was exposed to a fixed temperature of 810 °C for 3 d, 10 d, and 34 d. The samples were sealed under an inert atmosphere of roughly 200 mbar argon pressure in a silica tube. The heat treatment was conducted in a commercial tube furnace.

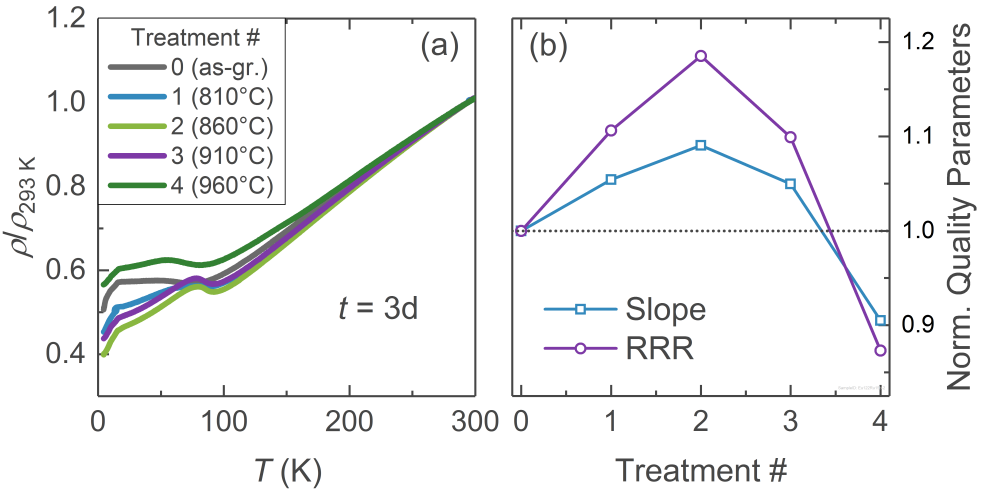


FIGURE A.2: Annealing results of $Eu(Fe_{1-x}Ru_x)_2As_2$ with $x_{nom} = 0.15$. The sample was subjected to 4 heat treatments with a duration of 3d and varying temperatures. (a) Normalized in-plane resistivity $\rho/\rho_{293\,K}$ and (b) extracted quality parameters: slope and RRR normalized to the value of the as-grown crystal.

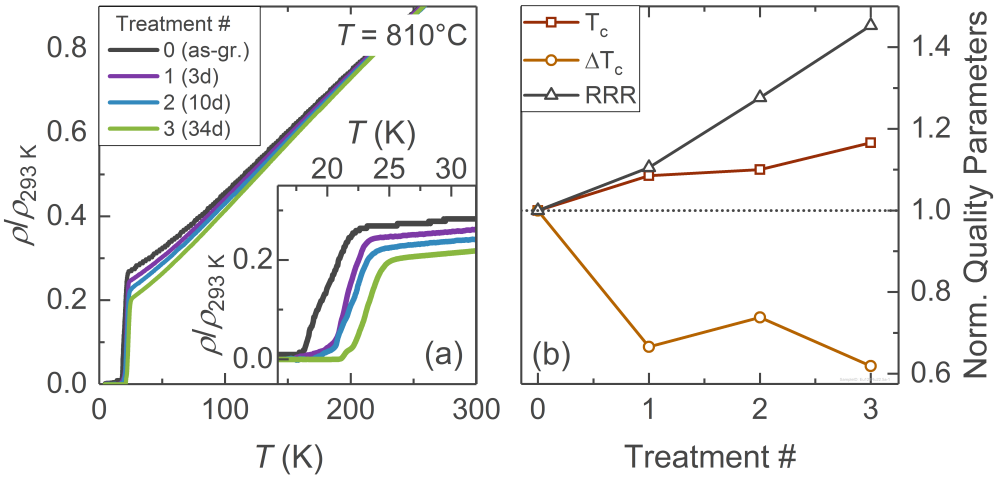


FIGURE A.3: Annealing results of $Eu(Fe_{1-x}Ru_x)_2As_2$ with $x_{nom} = 0.225$. The sample was subjected to 3 heat treatments at 810 K with varying duration. (a) Normalized in-plabe resistivity $\rho/\rho_{293\,K}$. (inset) Enlarged view around the SC transition $T_{SC}$. (b) Extracted quality parameters: $T_{SC}$, $\Delta T_{SC}$, and RRR normalized to the value of the as-grown crystal.

Figure A.2 shows the normalized in-plane electrical resistivity and extracted quality parameters normalized to the values of the as-grown crystal, namely, the residual resistivity ratio (RRR) and the slope of $\rho(T)$. Treatments of up to 860 °C improve the sample quality, as evidenced by the increase in the quality parameters and a much more pronounced signature at $T_{Fe}$, which is suppressed to about 90 K for this particular doping concentration. Higher temperatures seem to lead to additional disorder in the crystal, and quality parameters decrease accordingly, eventually leading to values even below those of the as-grown sample. These measurements, therefore, indicate that the optimal temperature for annealing is around 860 °C.

The results of the second series of heat treatments are depicted in Fig. A.3. The RRR, the superconducting transition temperature $T_c$, and the width of the superconducting transition $\Delta T_c$ are used as quality parameters. With increasing exposure time, the in-plane resistivity decreases faster as a function of temperature. Furthermore, the RRR and $T_c$ increase by roughly 40 % and 20 %, respectively. At the same time, the width of the SC transition decreases by almost 40 % after the third heat treatment. These results suggest that the longer the heat treatment at 810 °C, the better the sample quality. Combining these results with the results of the first series of heat treatments indicates that the exposure time could be further reduced by using a set point of 860 °C instead of 810 °C.

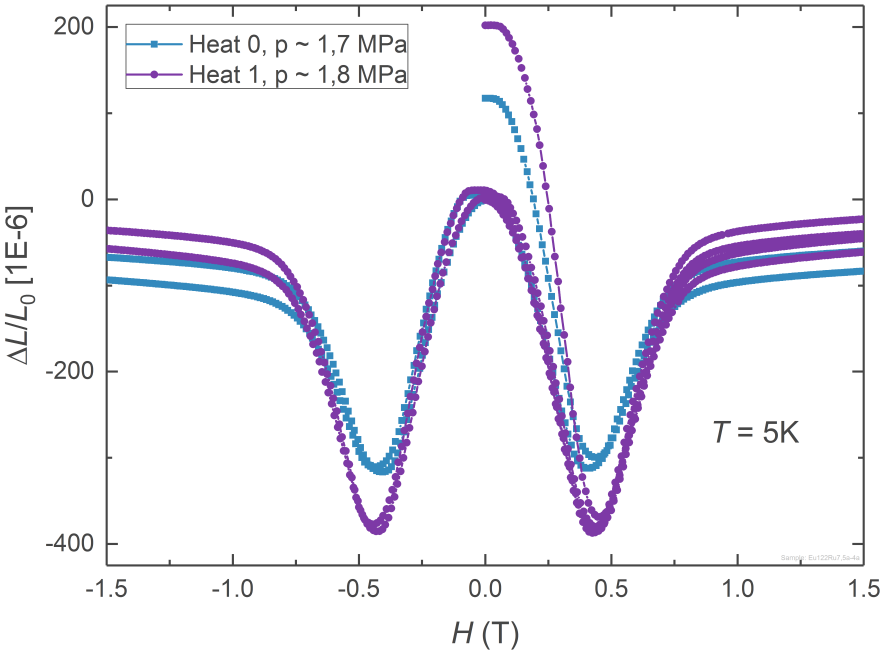


FIGURE A.4: Magnetostriction of an $Eu(Fe_{1-x}Ru_x)_2As_2$ (x=0.075) single crystal at 5 K before (Heat 0) and after (Heat 1) annealing at 860 K for 4 days. The absolute signal increased by 37.3 % after the heat treatment. The pressure from the dilatometer was kept virtually constant for both measurements for better comparability.

## Magnetostriction

### Effect of Annealing

The effect of annealing on the magnetostriction (MS) can be seen in Fig. A.4. The overall signature does not change qualitatively after exposing the sample to a temperature of 860 K for 4 days. However, the magnitude of the MS increases moderately, while the characteristic fields such as the minimum, or the inflection points stay virtually constant. This behavior can be explained by and increased mobility of the domain walls due to the annealing process, which likely results in a diminished crystal defect density throughout the sample.

### Effect of Pressure

The diminishing effect of pressure from the dilatometer on the magnetic detwinning was already discussed in the main text. Here Fig. A.5 presents more quantitative data, confirming the earlier statement. Due to the large initial (irreversible) detwinning effect,

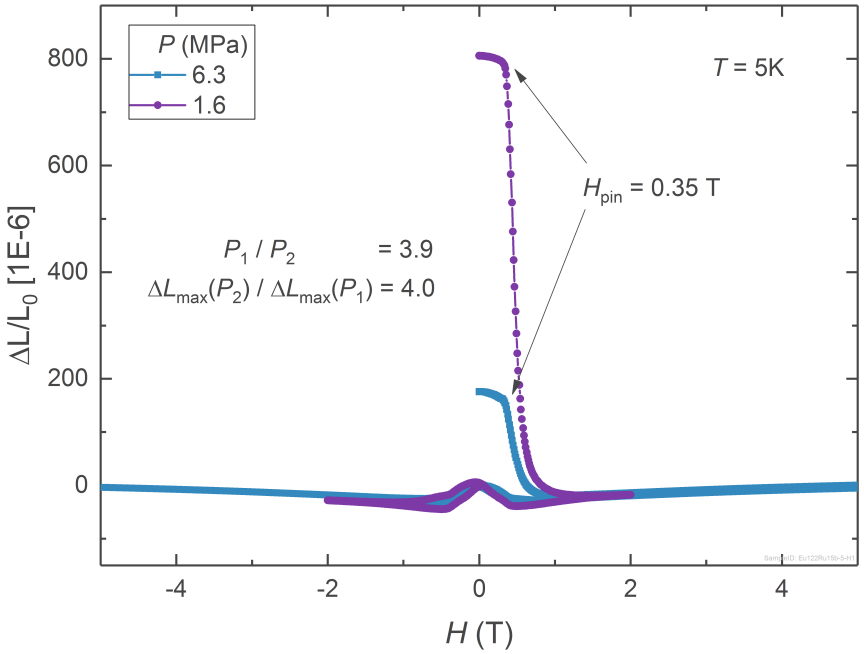


FIGURE A.5: Magnetostriction of a $Eu(Fe_{1-x}Ru_x)_2As_2$ sample with $x = 0.15$ at $T < T_{Eu}$ and different dilatometer pressure.

the Ru-doped sample with $x = 0.15$ was chosen. While the reversible detwinning is virtually unaffected by the pressure increase, the relationship between pressure and initial detwinning is directly proportional at the investigated pressure values, i. e. a roughly fourfold increase in pressure leads to a fourfold reduction in $\Delta L/L_0$, while the characteristic downturn at $H_{pin}$ is unaffected by the pressure.

## Angular-dependent Magnetoresistance

Figure A.6 depicts the magnetoresistance (MR) of a slightly P-doped $EuFe_2As_2$ sample as a function of magnetic field $H$ and sample position. The sample position denotes the angle between $H$ and the in-plane electrical current. The data should qualitatively correspond to the MR of the undoped system. Corresponding "field slices" at constant sample positions were depicted in Fig. 6.16(a). At fixed and small magnetic field values, the $C_4$ symmetry of the system in the AF ordered state of the $Eu^{2+}$ moments is clearly visible, while the transition to FM order is also evident above $H_1 \approx 0.6\,\mathrm{T}$.

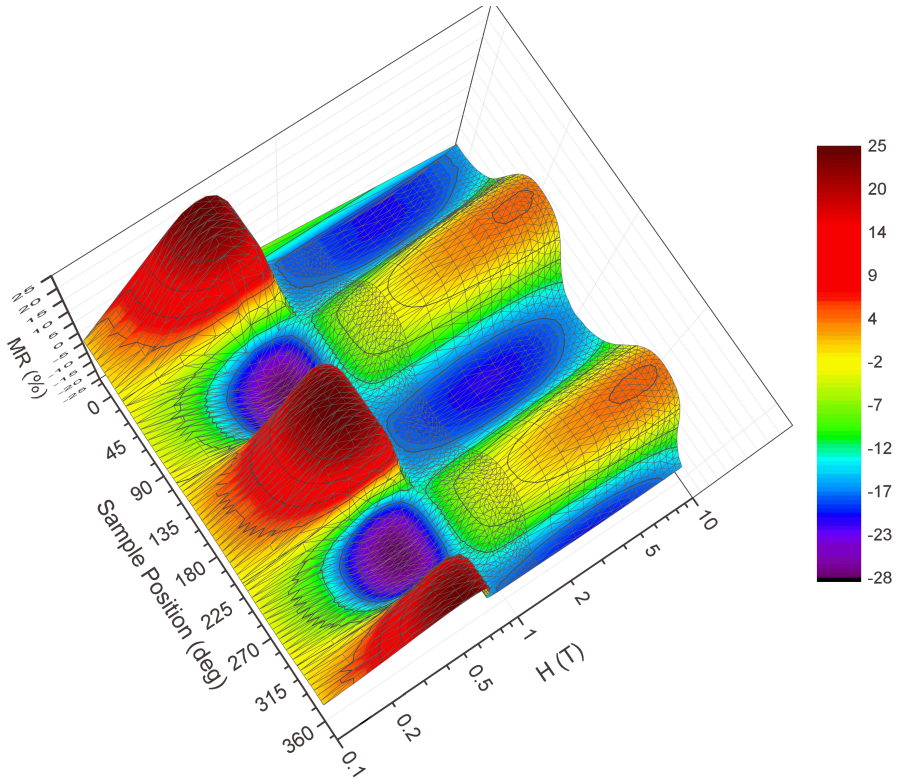


FIGURE A.6: Magnetoresistance MR(%) of $EuFe_2(As_{1-x}P_x)_2$ with $x = 0.05$ as a function of sample position and magnetic field at $T < T_{Eu}$. The sample position denotes the angle between the applied magnetic field and the current direction. Note how the system changes from AF to FM Eu order around 1 T.

Appendix B

# First-Principles Calculations

The key parameters of the theory were estimated computationally by I. I. Mazin from the Materials Science and Technology Division of the Naval Research Laboratory in Washington. The calculations were performed using the plane-wave code VASP [187], as described in Ref. [188], and the Generalized Gradient Approximation (GGA) to the Density Functional Theory (DFT). Two sets of calculations were performed, using the structural parameters of $EuFe_2As_2$ given in Ref. [189]. In the first one the energy difference between the following configurations were calculated: the Fe spins point along the magnetic easy axis $a$, while the Eu spins were either parallel or perpendicular (along $b$) to the Fe spins. In the second one, the energy difference between configurations with the Fe spins along the hard $b$-axis and Eu spins again either parallel or perpendicular (along $b$) to the former, were determined.

The results depend on the Hubbard $U$ (applied on the Eu 4f orbital), but are consistent between two sets , when $U$ is fixed to the same value. The biquadratic coupling constant $K$ was, in particular, found to be $\approx 0.4\,\mathrm{meV}$ for $U - J = 7\,\mathrm{eV}$. For $U = 0$, a larger value of $K \approx 0.8\,\mathrm{meV}$ was obtained. These values are larger than the ones obtained from experiment. The biquadratic term depends on the small overlap of the Eu $4f$ and the Fe $3d$ orbitals, which in turn is very sensitive to localization. Therefore, one reason for this discrepancy between theory and experiment might be that the GGA underestimates the localization of the wave function.

The out-of-plane coupling constant $J_\perp$ was estimated similarly, by comparing the total energies of ferromagnetic Eu layers, which were stacked either ferromagnetically or antiferromagnetically along the $c$-axis. The in-plane coupling constant $J_\parallel$ was calculated by considering ferromagnetic and checkerboard-antiferromagnetic in-plane arrangements of the Eu spins. For all these configurations the Fe spins were fixed to stripe

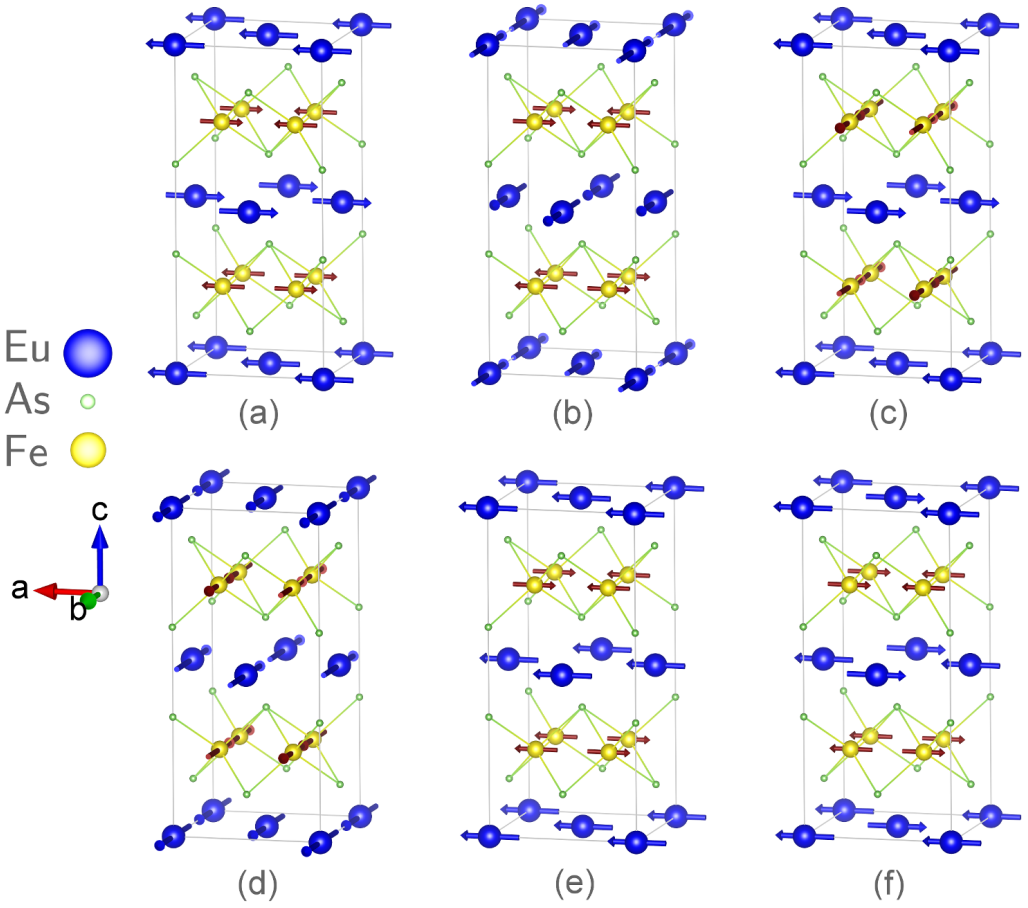


FIGURE B.1: Low-temperature magnetic configurations of $EuFe_2As_2$ used for estimating the parameters of the new theory from DFT calculations. The pattern pairs (a,b) and (c,d) were used for the estimation of $K$, while the pair (a,e) was used for $J_\perp$ and (a,f) for $J_\parallel$.

antiferromagnetism. The respective arrangements are depicted in Fig. B.1. We find $J_\perp = 0.14\,\text{meV/Eu}$ (1.6 K) for $U - J = 0$ and $J_\perp = 0.26\,\text{meV/Eu}$ (3 K) for $U - J = 5\,\text{eV}$, while $J_\parallel = -2\,\text{meV}$ (23 K) and -0.8 meV (9 K), respectively.

Appendix C

# Details on the Microscopic Theory

Table C.1 lists the domain energy difference $dE$ and respective stability ranges of all the cases calculated for the microscopic detwinning theory within this thesis. Additionally, the respective critical field expressions and domain types are stated for convenience.

TABLE C.1: Domain energy difference $dE$ for all field regimes for $12K/J_\perp < 1$. For $12K/J_\perp > 1$ and $8K/J_\perp < 1$, $H_1$ changes to $H_1^{\mathrm{sat}}$ [see Eq. (6.15)], which is between $\{H_a^{\mathrm{sat}}, H_b^{\mathrm{sat}}\}$ (Fig. 6.5). If $8K/J_\perp > 1$, the spin-flop at $H_a^{\mathrm{flop}}$ is replaced by a spin-flip at $H_a^{\mathrm{flip}}$ [see Eq. (6.11)].

| $dE$ | | Stability range | Critical field | Domain type |
|---|---|---|---|---|
| $E_0 - E_b^{\mathrm{min}}$ | $= \frac{M^2H^2}{8(J_\perp+4K)}$ | $0 \le H \le H_a^{\mathrm{flop}}$ | $H_a^{\mathrm{flop}} = 8/M\sqrt{K(J_\perp - 4K)}$ | b-twin |
| $E_a^{\mathrm{min}} - E_b^{\mathrm{min}}$ | $= K\left(8 - \frac{M^2H^2}{J_\perp^2 - 16K^2}\right)$ | $H_a^{\mathrm{flop}} \le H \le H_1$ | $H_1 = 4/M\sqrt{(J_\perp^2 - 16K^2)/2}$ | $(dE > 0)$ |
| | | $H_1 \le H \le H_a^{\mathrm{sat}}$ | $H_a^{\mathrm{sat}} = 4/M(J_\perp - 4K)$ | a-twin |
| $E_a^{\mathrm{sat}} - E_b^{\mathrm{min}}$ | $= -MH + 2J_\perp + \frac{M^2H^2}{8(J_\perp+4K)}$ | $H_a^{\mathrm{sat}} \le H \le H_b^{\mathrm{sat}}$ | $H_b^{\mathrm{sat}} = 4/M(J_\perp + 4K)$ | $(dE < 0)$ |
| $E_a^{\mathrm{sat}} - \tilde{E}_b^{\mathrm{min}}$ | $= -8K + \frac{\tilde{M}^2H^2}{2(2\tilde{J}+\tilde{D}-4K)}$ | $H_b^{\mathrm{sat}} \le H \le H_2$ | $H_2 = 4/\tilde{M}\sqrt{K(2\tilde{J} + \tilde{D} - 4K)}$ | |
| | | $H_2 \le H \le \tilde{H}_a^{\mathrm{flop}}$ | $\tilde{H}_a^{\mathrm{flop}} = 2/\tilde{M}\sqrt{(\tilde{D}+4K)(2\tilde{J} - \tilde{D} - 4K)}$ | b-twin |
| $\tilde{E}_a^{\mathrm{min}} - \tilde{E}_b^{\mathrm{min}}$ | $= \frac{\tilde{M}^2H^2}{2(2\tilde{J}+\tilde{D}-4K)} - \frac{\tilde{M}^2H^2}{2(2\tilde{J}-\tilde{D}-4K)} + 2\tilde{D}$ | $\tilde{H}_a^{\mathrm{flop}} \le H \le H_3$ | $H_3 = 2/\tilde{M}\sqrt{2(\tilde{J} - 2K)^2 - \tilde{D}^2/2}$ | $(dE > 0)$ |
| | | $H_3 \le H \le \tilde{H}_a^{\mathrm{sat}}$ | $\tilde{H}_a^{\mathrm{sat}} = 2/\tilde{M}(2\tilde{J} - \tilde{D} - 4K)$ | a-twin |
| $\tilde{E}_a^{\mathrm{sat}} - \tilde{E}_b^{\mathrm{min}}$ | $= -2\tilde{M}H + \frac{\tilde{M}^2H^2}{2(2\tilde{J}+\tilde{D}-4K)} - 8K + 4\tilde{J}$ | $\tilde{H}_a^{\mathrm{sat}} \le H \le \tilde{H}_b^{\mathrm{sat}}$ | $\tilde{H}_b^{\mathrm{sat}} = 2/\tilde{M}(2\tilde{J} + \tilde{D} - 4K)$ | $(dE < 0)$ |
| $\tilde{E}_a^{\mathrm{sat}} - \tilde{E}_b^{\mathrm{sat}}$ | $-2\tilde{D}$ | $\tilde{H}_b^{\mathrm{sat}} \le H$ | - | |

# Bibliography


1. H. Kamerlingh Onnes: The Superconductivity of Mercury. *Comm. Phys. Lab. Univ. Leiden* 122&124 (1911).
2. J. Bardeen, L. N. Cooper, and J. R. Schrieffer: Microscopic Theory of Superconductivity. *Phys. Rev.* 106(1) (1957), 162. DOI: 10.1103/PhysRev.106.162.
3. V. L. Ginzburg: Once again about high-temperature superconductivity. *Contemp. Phys.* 33(1) (1992), 15. DOI: 10.1080/00107519208219137.
4. A. P. Drozdov, M. I. Eremets, I. A. Troyan, V. Ksenofontov, and S. I. Shylin: Conventional superconductivity at 203 kelvin at high pressures in the sulfur hydride system. *Nature* 525(7567) (2015), 73. DOI: 10.1038/nature14964.
5. J. G. Bednorz and K. A. Müller: Possible high $T_c$ superconductivity in the Ba-La-Cu-O system. *Zeitschrift für Physik B Condensed Matter* 64(2) (1986), 189. DOI: 10.1007/BF01303701.
6. Y. Kamihara et al.: Iron-Based Layered Superconductor: LaOFeP. *J. Am. Chem. Soc.* 37(45) (2006), 10012. DOI: 10.1002/chin.200645012.
7. Y. Kamihara, T. Watanabe, M. Hirano, and H. Hosono: Iron-Based Layered Superconductor $La[O_{1-x}F_x]FeAs$ ($x = 0.05 - 0.12$) with $T_c = 26\,K$. *J. Am. Chem. Soc.* 130(11) (2008), 3296. DOI: 10.1021/ja800073m.
8. E. Cartlidge: Superconductivity record sparks wave of follow-up physics. *Nature* 524(7565) (2015), 277. DOI: 10.1038/nature.2015.18191.
9. S. Blundell: *Magnetism in Condensed Matter*. Oxford University Press Inc., 2001.
10. S. Zapf: Optical and Magnetization Studies on Europium Based Iron Pnictides. PhD thesis. University of Stuttgart, 2015.
11. M. Getzlaff: *Fundamentals of magnetism*. Springer Science & Business Media, 2007.
12. A. W. Overhauser: Giant Spin Density Waves. *Phys. Rev. Lett.* 4(9) (1960), 462. DOI: 10.1103/PhysRevLett.4.462.
13. A. W. Overhauser: Spin Density Waves in an Electron Gas. *Phys. Rev.* 128(3) (1962), 1437. DOI: 10.1103/PhysRev.128.1437.

14. S. Brown and G. Grüner: Charge and spin density waves. *Sci. Amer.* 270(4) (1994), 50. DOI: 10.1038/scientificamerican0494-50.

15. G. Grüner: The dynamics of spin-density waves. *Rev. Mod. Phys.* 66 (1994), 1. DOI: 10.1103/RevModPhys.66.1.

16. E. Fawcett: Spin-density-wave antiferromagnetism in chromium. *Rev. Mod. Phys.* 60(1) (1988), 209. DOI: 10.1103/RevModPhys.60.209.

17. P. Fazekas: *Lecture Notes on Electron Correlation and Magnetism*. Vol. 5. Series in Modern Condensed Matter Physics. World Scientific, 1999. DOI: 10.1142/2945.

18. D. S. Rodbell, I. S. Jacobs, J. Owen, and E. A. Harris: Biquadratic Exchange and the Behavior of Some Antiferromagnetic Substances. *Phys. Rev. Lett.* 11(1) (1963), 10. DOI: 10.1103/PhysRevLett.11.10.

19. E. A. Harris and J. Owen: Biquadratic Exchange Between $Mn^{2+}$ Ions in MgO. *Phys. Rev. Lett.* 11(1) (1963), 9. DOI: 10.1103/PhysRevLett.11.9.

20. A. N. Yaresko, G.-Q. Liu, V. N. Antonov, and O. K. Andersen: Interplay between magnetic properties and Fermi surface nesting in iron pnictides. *Phys. Rev. B* 79(14) (2009), 144421. DOI: 10.1103/PhysRevB.79.144421.

21. M. J. Han, Q. Yin, W. E. Pickett, and S. Y. Savrasov: Anisotropy, Itineracy, and Magnetic Frustration in High-$T_C$ Iron Pnictides. *Phys. Rev. Lett.* 102(10) (2009), 107003. DOI: 10.1103/PhysRevLett.102.107003.

22. D. Stanek, O. P. Sushkov, and G. S. Uhrig: Self-consistent spin-wave theory for a frustrated Heisenberg model with biquadratic exchange in the columnar phase and its application to iron pnictides. *Phys. Rev. B* 84(6) (2011), 064505. DOI: 10.1103/PhysRevB.84.064505.

23. P. B. Ergueta and A. H. Nevidomskyy: Ising-nematic order in the bilinear-biquadratic model for the iron pnictides. *Phys. Rev. B* 92(16) (2015), 165102. DOI: 10.1103/PhysRevB.92.165102.

24. J. K. Glasbrenner et al.: Effect of magnetic frustration on nematicity and superconductivity in iron chalcogenides. *Nat. Phys.* 11(11) (2015). Article, 953. DOI: 10.1038/nphys3434.

25. M. E. Peskin and D. V. Schroeder: *An Introduction To Quantum Field Theory*. Westview Press, 1995.

26. M. R. Norman: The Challenge of Unconventional Superconductivity. *Science* 332(6026) (2011), 196. DOI: 10.1126/science.1200181.

27. Wikimedia-Commons: *Gips (Schwalbenschwanz-Zwilling) - Nordhausen, Harz*. 2009. URL: https://de.wikipedia.org/wiki/Datei:Gips_(Schwalbenschwanz-Zwilling)_-_Nordhausen,_Harz.jpg (visited on 02/17/2017).

28. Wikimedia-Commons: *Pyrite 60608*. 2008. URL: https://commons.wikimedia.org/wiki/File:Pyrite_60608.jpg (visited on 02/17/2017).

29. Wikimedia-Commons: *Chrysoberyl-282796*. 2010. URL: https://commons.wikimedia.org/wiki/File:Chrysoberyl-282796.jpg (visited on 02/17/2017).

30. M. Nespolo and G. Ferraris: The oriented attachment mechanism in the formation of twins – a survey. *Eur. J. Mineral.* 16(3) (2004), 401. DOI: 10.1127/0935-1221/2004/0016-0401.

31. H. Grimmer and M. Nespolo: Geminography: the crystallography of twins. *Z. Kristallogr. - Crystalline Materials* 221(1) (2006), 28. DOI: 10.1524/zkri.2006.221.1.28.

32. T. Hahn and H. Klapper: Twinning of crystals. *International Tables for Crystallography.* Vol. D, Chapter 3.3. International Union of Crystallography (IUCr), 2013, 413. DOI: 10.1107/97809553602060000917.

33. M. A. Tanatar et al.: Direct imaging of the structural domains in the iron pnictides $AFe_2As_2$ ($A = Ca, Sr, Ba$). *Phys. Rev. B* 79(18) (2009), 180508. DOI: 10.1103/PhysRevB.79.180508.

34. H. Schmid et al.: Polarized light and X-ray precession study of the ferroelastic domains of $YBa_2Cu_3O_{7-\delta}$. *Z. Phys. B: Condens. Matter* 72(3) (1988), 305. DOI: 10.1007/bf01312817.

35. G. J. McIntyre, A. Renault, and G. Collin: Domain and crystal structure of superconducting $Ba_2YCu_3O_{8-\delta}$ at 40 and 100 K by single-crystal neutron diffraction. *Phys. Rev. B* 37(10) (1988), 5148. DOI: 10.1103/PhysRevB.37.5148.

36. J. Giapintzakis, D. M. Ginsberg, and P.-D. Han: A Method for Obtaining Single Domain Superconducting $YBa_2Cu_3O_{7-x}$ Single Crystals. *J. Low Temp. Phys.* 77(1) (1989), 155. DOI: 10.1007/BF00681884.

37. E. C. Blomberg et al.: Effect of tensile stress on the in-plane resistivity anisotropy in $BaFe_2As_2$. *Phys. Rev. B* 85(14) (2012), 144509. DOI: 10.1103/physrevb.85.144509.

38. S. Jiang, H. S. Jeevan, J. Dong, and P. Gegenwart: Thermopower as a Sensitive Probe of Electronic Nematicity in Iron Pnictides. *Phys. Rev. Lett.* 110(6) (2013), 067001. DOI: 10.1103/physrevlett.110.067001.

39. E. Limpert, W. A. Stahel, and M. Abbt: Log-normal Distributions across the Sciences: Keys and Clues. *BioScience* 51(5) (2001), 341. DOI: 10.1641/0006-3568(2001)051[0341:lndats]2.0.co;2.

40. R. E. Honig: Vapor pressure data for the solid and liquid elements. *Rad. Corp. Amer. Review* 23 (1962), 567.

41. B. Saparov, J. E. Mitchell, and A. S. Sefat: Properties of binary transition-metal arsenides ( T As). *Supercond. Sci. Technol.* 25(8) (2012), 084016. DOI: 10.1088/0953-2048/25/8/084016.

42. S. Jiang et al.: Metamagnetic transition in $EuFe_2As_2$ single crystals. *New J. Phys.* 11(2) (2009), 025007. DOI: 10.1088/1367-2630/11/2/025007.

43. W.-H. Jiao et al.: Anisotropic superconductivity in Eu(Fe 0.75 Ru 0.25 ) 2 As 2 ferromagnetic superconductor. *EPL (Europhysics Letters)* 95(6) (2011), 67007. DOI: 10.1209/0295-5075/95/67007.

44. Quantum Design: *MPMS-XL Hardware Reference Manual.* 1st. 2000.

45. Quantum Design: *Thermal Transport Option User's Manual.* 3rd. 2002.

46. Quantum Design: *Application Note: Thermal Transport.* Rev 7.06. 2010.

47. H. Hosono and K. Kuroki: Iron-based superconductors: Current status of materials and pairing mechanism. *Physica C* 514 (2015), 399. DOI: 10.1016/j.physc.2015.02.020.

48. P. D. Johnson, G. Xu, and W.-G. Yin: *Iron-Based Superconductivity*. Springer International Publishing, 2015. DOI: 10.1007/978-3-319-11254-1.

49. A. S. Sefat: Bulk synthesis of iron-based superconductors. *Curr. Opin. Solid State Mater. Sci.* 17(2) (2013). Fe-based Superconductors, 59. DOI: 10.1016/j.cossms.2013.04.001.

50. A. Charnukha: *Charge Dynamics in 122 Iron-Based Superconductors*. 1st ed. Springer International Publishing, 2014. DOI: 10.1007/978-3-319-01192-9.

51. D. C. Johnston: The puzzle of high temperature superconductivity in layered iron pnictides and chalcogenides. *Adv. Phys.* 59(6) (2010), 803. DOI: 10.1080/00018732.2010.513480.

52. I. I. Mazin: Superconductivity gets an iron boost. *Nature* 464(7286) (2010), 183. DOI: 10.1038/nature08914.

53. J. Paglione and R. L. Greene: High-temperature superconductivity in iron-based materials. *Nat. Phys.* 6(9) (2010), 645. DOI: 10.1038/nphys1759.

54. P. Dai, J. Hu, and E. Dagotto: Magnetism and its microscopic origin in iron-based high-temperature superconductors. *Nat. Phys.* 8(10) (2012), 709. DOI: 10.1038/nphys2438.

55. R. M. Fernandes, A. V. Chubukov, and J. Schmalian: What drives nematic order in iron-based superconductors? *Nat. Phys.* 10(2) (2014), 97. DOI: 10.1038/nphys2877.

56. A. Chubukov and P. J. Hirschfeld: Iron-based superconductors, seven years later. *Phys. Today* 68(6) (2015), 46. DOI: 10.1063/pt.3.2818.

57. H. Hosono: Recent progress in transparent oxide semiconductors: Materials and device application. *Thin Solid Films* 515(15) (2007), 6000. DOI: 10.1016/j.tsf.2006.12.125.

58. H. Hosono: Two classes of superconductors discovered in our material research: Iron-based high temperature superconductor and electride superconductor. *Physica C* 469(9-12) (2009). Superconductivity in Iron-Pnictides, 314. DOI: 10.1016/j.physc.2009.03.014.

59. M. Fujioka et al.: Phase diagram and superconductivity at 58.1 K in $\alpha$-FeAs-free $SmFeAsO_{1-x}F_x$. *Supercond. Sci. Technol.* 26(8) (2013), 085023. DOI: 10.1088/0953-2048/26/8/085023.

60. Z.-A. Ren et al.: Superconductivity and phase diagram in iron-based arsenic-oxides $ReFeAsO_{1-\delta}$ (Re = rare-earth metal) without fluorine doping. *Europhys. Lett.* 83(1) (2008), 17002. DOI: 10.1209/0295-5075/83/17002.

61. T. Hanna et al.: Hydrogen in layered iron arsenides: Indirect electron doping to induce superconductivity. *Phys. Rev. B* 84(2) (2011), 024521. DOI: 10.1103/PhysRevB.84.024521.

62. J.-F. Ge et al.: Superconductivity above 100 K in single-layer FeSe films on doped $SrTiO_3$. *Nat. Mater.* 14(3) (2015), 285. DOI: 10.1038/nmat4153.

63. H. Gretarsson et al.: Revealing the dual nature of magnetism in iron pnictides and iron chalcogenides using x-ray emission spectroscopy. *Physical Review B* 84(10) (2011), 100509. DOI: 10.1103/physrevb.84.100509.

64. S. Nandi et al.: Coexistence of superconductivity and ferromagnetism in P-doped $EuFe_2As_2$. *Phys. Rev. B* 89(1) (2014), 014512. DOI: 10.1103/physrevb.89.014512.

65. J. Maiwald, H. S. Jeevan, and P. Gegenwart: Signatures of quantum criticality in hole-doped and chemically pressurized $EuFe_2As_2$ single crystals. *Phys. Rev. B* 85(2) (2012), 024511. DOI: 10.1103/physrevb.85.024511.

66. R. M. Fernandes and J. Schmalian: Manifestations of nematic degrees of freedom in the magnetic, elastic, and superconducting properties of the iron pnictides. *Supercond. Sci. Technol.* 25(8) (2012), 084005. DOI: 10.1088/0953-2048/25/8/084005.

67. P. G. de Gennes and J. Prost: *The Physics of Liquid Crystals*. Clarendon Press, Oxford, 1993.

68. Q. Si, R. Yu, and E. Abrahams: High-temperature superconductivity in iron pnictides and chalcogenides. *Nature Rev. Mater.* 1(4) (2016), 16017. DOI: 10.1038/natrevmats.2016.17.

69. A. J. Achkar et al.: Nematicity in stripe-ordered cuprates probed via resonant x-ray scattering. *Science* 351(6273) (2016), 576. DOI: 10.1126/science.aad1824.

70. Y. Zhang et al.: Orbital characters of bands in the iron-based superconductor $BaFe_{1.85}Co_{0.15}As_2$. *Phys. Rev. B* 83(5) (2011), 054510. DOI: 10.1103/PhysRevB.83.054510.

71. S. Graser, T. A. Maier, P. J. Hirschfeld, and D. J. Scalapino: Near-degeneracy of several pairing channels in multiorbital models for the Fe pnictides. *New Journal of Physics* 11(2) (2009), 025016. DOI: 10.1088/1367-2630/11/2/025016.

72. D. H. Lu et al.: Electronic structure of the iron-based superconductor LaOFeP. *Nature* 455(7209) (2008), 81. DOI: 10.1038/nature07263.

73. D. Lu et al.: ARPES studies of the electronic structure of LaOFe(P,As). *Physica C: Superconductivity* 469(9-12) (2009), 452. DOI: 10.1016/j.physc.2009.03.044.

74. M. Yi et al.: Electronic structure of the $BaFe_2As_2$ family of iron-pnictide superconductors. *Phys. Rev. B* 80(2) (2009), 024515. DOI: 10.1103/PhysRevB.80.024515.

75. Z. P. Yin, K. Haule, and G. Kotliar: Kinetic frustration and the nature of the magnetic and paramagnetic states in iron pnictides and iron chalcogenides. *Nat. Mater.* 10(12) (2011), 932. DOI: 10.1038/nmat3120.

76. Y.-Z. You, F. Yang, S.-P. Kou, and Z.-Y. Weng: Magnetic and superconducting instabilities in a hybrid model of itinerant/localized electrons for iron pnictides. *Phys. Rev. B* 84(5) (2011), 054527. DOI: 10.1103/physrevb.84.054527.

77. E. Abrahams and Q. Si: Quantum criticality in the iron pnictides and chalcogenides. *J. Phys.: Condens. Matter* 23(22) (2011), 223201. DOI: 10.1088/0953-8984/23/22/223201.

78. M. M. Qazilbash et al.: Electronic correlations in the iron pnictides. *Nat. Phys.* 5(9) (2009), 647. DOI: 10.1038/nphys1343.

79. M. Yi et al.: Electronic reconstruction through the structural and magnetic transitions in detwinned NaFeAs. *New Journal of Physics* 14(7) (2012), 073019. DOI: 10.1088/1367-2630/14/7/073019.

80. A. Tamai et al.: Strong Electron Correlations in the Normal State of the Iron-Based $FeSe_{0.42}Te_{0.58}$ Superconductor Observed by Angle-Resolved Photoemission Spectroscopy. *Phys. Rev. Lett.* 104(9) (2010), 097002. DOI: 10.1103/PhysRevLett.104.097002.

81. M. Yi et al.: Observation of Temperature-Induced Crossover to an Orbital-Selective Mott Phase in $A_xFe_{2-y}Se_2$ ($A$=K, Rb) Superconductors. *Phys. Rev. Lett.* 110(6) (2013), 067003. DOI: 10.1103/PhysRevLett.110.067003.

82. M. Yi et al.: Observation of universal strong orbital-dependent correlation effects in iron chalcogenides. *Nat. Commun.* 6 (2015), 7777. DOI: 10.1038/ncomms8777.

83. D. S. Inosov et al.: Normal-state spin dynamics and temperature-dependent spin-resonance energy in optimally doped $BaFe_{1.85}Co_{0.15}As_2$. *Nat. Phys.* 6(3) (2010), 178. DOI: 10.1038/nphys1483.

84. P. J. Hirschfeld, M. M. Korshunov, and I. I. Mazin: Gap symmetry and structure of Fe-based superconductors. *Rep. Prog. Phys.* 74(12) (2011), 124508. DOI: 10.1088/0034-4885/74/12/124508.

85. F.-C. Hsu et al.: Superconductivity in the PbO-type structure $\alpha$-FeSe. *PNAS* 105(38) (2008), 14262. DOI: 10.1073/pnas.0807325105.

86. M. Rotter, M. Tegel, and D. Johrendt: Superconductivity at 38 K in the Iron Arsenide $(Ba_{1-x}K_x)Fe_2As_2$. *Phys. Rev. Lett.* 101(10) (2008), 107006. DOI: 10.1103/PhysRevLett.101.107006.

87. S. Jiang et al.: Superconductivity up to 30 K in the vicinity of the quantum critical point in $BaFe_2(As_{1-x}P_x)_2$. *J. Phys.: Condens. Matter* 21(38) (2009), 382203. DOI: 10.1088/0953-8984/21/38/382203.

88. T. P. Ying et al.: Observation of superconductivity at 30 K$\sim$46 K in $A_xFe_2Se_2$ (A = Li, Na, Ba, Sr, Ca, Yb, and Eu). *Sci. Rep.* 2 (2012). DOI: 10.1038/srep00426.

89. R. A. LAUDISE: Hydrothermal Synthesis of Crystals. *Chem. Eng. News* 65(39) (1987), 30. DOI: 10.1021/cen-v065n039.p030.

90. X. F. Lu et al.: Superconductivity in $LiFeO_2Fe_2Se_2$ with anti-PbO-type spacer layers. *Phys. Rev. B* 89(2) (2014), 020507. DOI: 10.1103/PhysRevB.89.020507.

91. S. Matsuishi et al.: Structural analysis and superconductivity of $CeFeAsO_{1-x}H_x$. *Phys. Rev. B* 85(1) (2012), 014514. DOI: 10.1103/PhysRevB.85.014514.

92. Z. A. Ren et al.: Superconductivity at 52 K in iron based F doped layered quaternary compound Pr $[O_{1-x}F_x]$ FeAs. *Mater. Res. Innovations* 12(3) (2013), 105. DOI: 10.1179/143307508x333686.

93. P. C. Canfield and Z. Fisk: Growth of single crystals from metallic fluxes. *Philos. Mag. B* 65(6) (1992), 1117. DOI: 10.1080/13642819208215073.

94. M. G. Kanatzidis, R. Pöttgen, and W. Jeitschko: The Metal Flux: A Preparative Tool for the Exploration of Intermetallic Compounds. *Angew. Chem., Int. Ed.* 44(43) (2005), 6996. DOI: 10.1002/anie.200462170.

95. D. Mandrus, A. S. Sefat, M. A. McGuire, and B. C. Sales: Materials Chemistry of $BaFe_2As_2$: A Model Platform for Unconventional Superconductivity. *Chem. Mater.* 22(3) (2010), 715. DOI: 10.1021/cm9027397.

96. J. S. Kim, E. G. Kim, and G. R. Stewart: Specific heat anomalies for $T \ll T_c$ in superconducting single crystal doped $BaFe_2As_2$ : comparison of different flux growth methods. *J. Phys.: Condens. Matter* 21(25) (2009), 252201. DOI: 10.1088/0953-8984/21/25/252201.

97. A. S. Sefat et al.: Superconductivity at 22 K in Co-Doped $BaFe_2As_2$ Crystals. *Phys. Rev. Lett.* 101(11) (2008), 117004. DOI: 10.1103/PhysRevLett.101.117004.

98. J. Guo et al.: Superconductivity in the iron selenide $K_xFe_2Se_2$ ($0 \leq x \leq 1.0$). *Phys. Rev. B* 82(18) (2010), 180520. DOI: 10.1103/PhysRevB.82.180520.

99. A. Krzton-Maziopa et al.: Synthesis and crystal growth of $Cs_{0.8}(FeSe_{0.98})_2$ : a new iron-based superconductor with $T_c = 27$ K. *J. Phys.: Condens. Matter* 23(5) (2011), 052203. DOI: 10.1088/0953-8984/23/5/052203.

100. A. F. Wang et al.: Superconductivity at 32 K in single-crystalline $Rb_xFe_{2-y}Se_2$. *Phys. Rev. B* 83(6) (2011), 060512. DOI: 10.1103/PhysRevB.83.060512.

101. B. C. Sales et al.: Bulk superconductivity at 14 K in single crystals of $Fe_{1+y}Te_xSe_{1-x}$. *Phys. Rev. B* 79(9) (2009), 094521. DOI: 10.1103/PhysRevB.79.094521.

102. V. Tsurkan et al.: Physical properties of $FeSe_{0.5}Te_{0.5}$ single crystals grown under different conditions. *Eur. Phys. J. B* 79(3) (2011), 289. DOI: 10.1140/epjb/e2010-10473-5.

103. H. S. Jeevan, D. Kasinathan, H. Rosner, and P. Gegenwart: Interplay of antiferromagnetism, ferromagnetisim and superconductivity in $EuFe_2(As_{1-y}P_y)_2$ single crystals. *Phys. Rev. B* 83(5) (2011), 054511. DOI: 10.1103/physrevb.83.054511.

104. S. Aswartham et al.: Single crystal growth and physical properties of superconducting ferro-pnictides Ba(Fe, Co)$_2$As$_2$ grown using self-flux and Bridgman techniques. *J. Cryst. Growth* 314(1) (2011), 341. DOI: 10.1016/j.jcrysgro.2010.11.149.

105. J. Maiwald and P. Gegenwart: Interplay of $4f$ and $3d$ moments in $EuFe_2As_2$ iron pnictides. *Phys. Status Solidi B* 254(1) (2016), 1600150. DOI: 10.1002/pssb.201600150.

106. Y. Xiao et al.: Magnetic structure of $EuFe_2As_2$ determined by single-crystal neutron diffraction. *Phys. Rev. B* 80(17) (2009), 174424. DOI: 10.1103/PhysRevB.80.174424.

107. H. Raffius et al.: Magnetic properties of ternary lanthanoid transition metal arsenides studied by Mössbauer and susceptibility measurements. *Journal of Physics and Chemistry of Solids* 54(2) (1993), 135. DOI: 10.1016/0022-3697(93)90301-7.

108. S. Jiang et al.: Superconductivity and local-moment magnetism in $Eu(Fe_{0.89}Co_{0.11})_2As_2$. *Phys. Rev. B* 80(18) (2009), 184514. DOI: 10.1103/PhysRevB.80.184514.

109. H. S. Jeevan et al.: Electrical resistivity and specific heat of single-crystalline $EuFe_2As_2$: A magnetic homologue of $SrFe_2As_2$. *Phys. Rev. B* 78(5) (2008), 052502. DOI: 10.1103/physrevb.78.052502.

110. D. Wu et al.: Effects of magnetic ordering on dynamical conductivity: Optical investigations of $EuFe_2As_2$ single crystals. *Phys. Rev. B* 79(15) (2009), 155103. DOI: 10.1103/PhysRevB.79.155103.

111. H. S. Jeevan et al.: High-temperature superconductivity in $Eu_{0.5}K_{0.5}Fe_2As_2$. *Phys. Rev. B* 78(9) (2008), 092406. DOI: 10.1103/PhysRevB.78.092406.

112. C. F. Miclea et al.: Evidence for a reentrant superconducting state in $EuFe_2As_2$ under pressure. *Phys. Rev. B* 79(21) (2009), 212509. DOI: 10.1103/PhysRevB.79.212509.

113. T. Terashima et al.: Resistivity and Upper Critical Field in $KFe_2As_2$ Single Crystals. *J. Phys. Soc. Jpn.* 78(6) (2009), 3702. DOI: 10.1143/jpsj.78.063702.

114. S. de Jong et al.: Droplet-like Fermi surfaces in the anti-ferromagnetic phase of $EuFe_2As_2$ , an Fe-pnictide superconductor parent compound. *Europhys. Lett.* 89(2) (2010), 27007. DOI: 10.1209/0295-5075/89/27007.

115. S. Thirupathaiah et al.: Dissimilarities between the electronic structure of chemically doped and chemically pressurized iron pnictides from an angle-resolved photoemission spectroscopy study. *Phys. Rev. B* 84(1) (2011), 014531. DOI: 10.1103/PhysRevB.84.014531.

116. Anupam, P. L. Paulose, H. S. Jeevan, C. Geibel, and Z. Hossain: Superconductivity and magnetism in K-doped $EuFe_2As_2$. *J. Phys.: Condens. Matter* 21(26) (2009), 265701. DOI: 10.1088/0953-8984/21/26/265701.

117. H. S. Jeevan and P. Gegenwart: Superconductivity and magnetism in $Eu_{1-x}K_xFe_2As_2$. *J. Phys. Conf. Ser.* 200(1) (2010), 012060. DOI: 10.1088/1742-6596/200/1/012060.

118. D. Wu, G. Chanda, H. S. Jeevan, P. Gegenwart, and M. Dressel: Optical investigations of chemical pressurized $EuFe_2(As_{1-x}P_x)_2$: An s-wave superconductor with strong interband interaction. *Phys. Rev. B* 83(10) (2011), 100503. DOI: 10.1103/PhysRevB.83.100503.

119. N. Pascher et al.: Magnetic fluctuations and superconductivity in iron pnictides as probed by electron spin resonance. *Phys. Rev. B* 82(5) (2010), 054525. DOI: 10.1103/physrevb.82.054525.

120. V. A. Gasparov, H. S. Jeevan, and P. Gegenwart: Normal-state electrical resistivity and superconducting magnetic penetration depth in $Eu_{0.5}K_{0.5}Fe_2As_2$ polycrystals. *J. Exp. Theor. Phys.* 89(6) (2009), 294. DOI: 10.1134/s0021364009060071.

121. M. Gooch, B. Lv, B. Lorenz, A. M. Guloy, and C.-W. Chu: Evidence of quantum criticality in the phase diagram of $K_xSr_{1-x}Fe_2As_2$ from measurements of transport and thermoelectricity. *Phys. Rev. B* 79(10) (2009), 104504. DOI: 10.1103/PhysRevB.79.104504.

122. I. M. Lifshitz: Anomalies of Electron Characteristics of a Metal in the High Pressure Region. *Zhur. Eksptl'. i Teoret. Fiz.* 38(5) (1960), 1569.

123. T. Terashima et al.: $EuFe_2As_2$ under High Pressure: An Antiferromagnetic Bulk Superconductor. *J. Phys. Soc. Jpn.* 78(8) (2009), 083701. DOI: 10.1143/JPSJ.78.083701.

124. Y. Tokiwa, S.-H. Hübner, O. Beck, H. S. Jeevan, and P. Gegenwart: Unique phase diagram with narrow superconducting dome in $EuFe_2(As_{1-x}P_x)_2$ due to $Eu^{2+}$ local magnetic moments. *Phys. Rev. B* 86(22) (2012), 220505. DOI: 10.1103/PhysRevB.86.220505.

125. S. Kasahara et al.: Evolution from non-Fermi- to Fermi-liquid transport via isovalent doping in $BaFe_2(As_{1-x}P_x)_2$ superconductors. *Phys. Rev. B* 81(18) (2010), 184519. DOI: 10.1103/PhysRevB.81.184519.

126. Y. Nakai et al.: Unconventional Superconductivity and Antiferromagnetic Quantum Critical Behavior in the Isovalent-Doped $BaFe_2(As_{1-x}P_x)_2$. *Phys. Rev. Lett.* 105(10) (2010), 107003. DOI: 10.1103/PhysRevLett.105.107003.

127. Z. Ren et al.: Superconductivity induced by phosphorus doping and its coexistence with ferromagnetism in $EuFe_2(As_{0.7}P_{0.3})_2$. *Phys. Rev. Lett.* 102(13) (2009), 137002. DOI: 10.1103/PhysRevLett.102.137002.

128. S. Nandi et al.: Magnetic structure of the $Eu^{2+}$ moments in superconducting $EuFe_2(As_{1-x}P_x)_2$ with $x = 0.19$. *Phys. Rev. B* 90(9) (2014), 094407. DOI: 10.1103/PhysRevB.90.094407.

129. S. Zapf et al.: Varying $Eu^{2+}$ magnetic order by chemical pressure in $EuFe_2(As_{1-x}P_x)_2$. *Phys. Rev. B* 84(14) (2011), 140503. DOI: 10.1103/PhysRevB.84.140503.

130. J. Fink et al.: Non-Fermi-liquid scattering rates and anomalous band dispersion in ferropnictides. *Phys. Rev. B* 92(20) (2015), 201106. DOI: 10.1103/PhysRevB.92.201106.

131. W.-H. Jiao et al.: Evolution of superconductivity and ferromagnetism in $Eu(Fe_{1-x}Ru_x)_2As_2$. *J. Phys. Conf. Ser.* 400(2) (2012), 022038. DOI: 10.1088/1742-6596/400/2/022038.

132. Y. He et al.: Evidence for competing magnetic and superconducting phases in superconducting $Eu_{1-x}Sr_xFe_{2-y}Co_yAs_2$ single crystals. *J. Phys.: Condens. Matter* 22(23) (2010), 235701. DOI: 10.1088/0953-8984/22/23/235701.

133. R. Hu, S. L. Bud'ko, W. E. Straszheim, and P. C. Canfield: Phase diagram of superconductivity and antiferromagnetism in single crystals of $Sr(Fe_{1-x}Co_x)_2As_2$ and $Sr_{1-y}Eu_y(Fe_{0.88}Co_{0.12})_2As_2$. *Phys. Rev. B* 83(9) (2011), 094520. DOI: 10.1103/PhysRevB.83.094520.

134. R. Sarkar et al.: Magnetism and superconductivity in $Eu_{0.2}Sr_{0.8}(Fe_{0.86}Co_{0.14})_2As_2$ probed by $^{75}As$ NMR. *J. Phys. Condens. Matter* 24(4) (2012), 045702. DOI: 10.1088/0953-8984/24/4/045702.

135. S. Zapf and M. Dressel: Europium-based iron pnictides: a unique laboratory for magnetism, superconductivity and structural effects. *Reports on Progress in Physics* 80(1) (2017), 016501. DOI: 10.1088/0034-4885/80/1/016501.

136. Anupam, P. L. Paulose, S. Ramakrishnan, and Z. Hossain: Doping dependent evolution of magnetism and superconductivity in $Eu_{1-x}K_xFe_2As_2$ ($x = 0$–$1$) and temperature dependence of the lower critical field $H_{c1}$. *J. Phys.: Condens. Matter* 23(45) (2011), 455702. DOI: 10.1088/0953-8984/23/45/455702.

137. Z. Ren et al.: Antiferromagnetic transition in $EuFe_2As_2$: A possible parent compound for superconductors. *Phys. Rev. B* 78(5) (2008), 052501. DOI: 10.1103/physrevb.78.052501.

138. Ö. Rapp, G. Benediktsson, H. U. Åström, S. Arajs, and K. V. Rao: Electrical resistivity of antiferromagnetic chromium near the Néel temperature. *Phys. Rev. B* 18(7) (1978), 3665. DOI: 10.1103/PhysRevB.18.3665.

139. T. T. M. Palstra, A. A. Menovsky, and J. A. Mydosh: Anisotropic electrical resistivity of the magnetic heavy-fermion superconductor $URu_2Si_2$. *Phys. Rev. B* 33(9) (1986), 6527. DOI: 10.1103/PhysRevB.33.6527.

140. W. Schlabitz et al.: Superconductivity and magnetic order in a strongly interacting fermi-system: $URu_2Si_2$. *Z. Phys. B: Condens. Matter* 62(2) (1986), 171. DOI: 10.1007/BF01323427.

141. A. Krimmel et al.: The evolution from long-range magnetic order to spin-glass behaviour in $PrAu_2(Si_{1-x}Ge_x)_2$. *J. Phys.: Condens. Matter* 11(36) (1999), 6991.

142. D. A. Joshi, A. Nigam, S. Dhar, and A. Thamizhavel: Magnetocrystalline anisotropy in $\{RAu_2Ge_2\}$ (R = La, Ce and Pr) single crystals. *J. Magn. Magn. Mater.* 322(21) (2010), 3363. DOI: 10.1016/j.jmmm.2010.06.028.

143. P. Gegenwart et al.: Breakup of Heavy Fermions on the Brink of "Phase $A$" in $CeCu_2Si_2$. *Phys. Rev. Lett.* 81 (1998), 1501. DOI: 10.1103/PhysRevLett.81.1501.

144. C.-C. Chen et al.: Orbital order and spontaneous orthorhombicity in iron pnictides. *Phys. Rev. B* 82(10) (2010), 100504. DOI: 10.1103/PhysRevB.82.100504.

145. W. Lv, J. Wu, and P. Phillips: Orbital ordering induces structural phase transition and the resistivity anomaly in iron pnictides. *Phys. Rev. B* 80(22) (2009), 224506. DOI: 10.1103/PhysRevB.80.224506.

146. N. Eguchi et al.: Powder x-ray diffraction of $BaFe_2As_2$ under hydrostatic pressure. *J. Phys. Conf. Ser.* 400(2) (2012), 022017.

147. K. Jacob, S. Raj, and L. Rannesh: Vegard's law: a fundamental relation or an approximation? *Int. J. Mater. Res.* 98(9) (2007), 776. DOI: 10.3139/146.101545.

148. S. R. Saha et al.: Superconductivity at 23 K in Pt doped $BaFe_2As_2$ single crystals. *J. Phys.: Condens. Matter* 22(7) (2010), 072204. DOI: 10.1088/0953-8984/22/7/072204.

149. P. C. Canfield and S. L. Bud'ko: FeAs-Based Superconductivity: A Case Study of the Effects of Transition Metal Doping on $BaFe_2As_2$. *Annu. Rev. Condens. Matter Phys.* 1(1) (2010), 27. DOI: 10.1146/annurev-conmatphys-070909-104041.

150. W. Jeitschko, R. Glaum, and L. Boonk: Superconducting $LaRu_2P_2$ and other alkaline earth and rare earth metal ruthenium and osmium phosphides and arsenides with $ThCr_2Si_2$ structure. *J. Solid State Chem.* 69(1) (1987), 93. DOI: 10.1016/0022-4596(87)90014-4.

151. A. Thaler et al.: Physical and magnetic properties of $Ba(Fe_{1-x}Ru_x)_2As_2$ single crystals. *Phys. Rev. B* 82(1) (2010). DOI: 10.1103/PhysRevB.82.014534.

152. K. Zhao, C. Stingl, R. S. Manna, C. Q. Jin, and P. Gegenwart: Reversible tuning of the collapsed tetragonal phase transition in $CaFe_2As_2$ by separate control of chemical pressure and electron doping. *Phys. Rev. B* 92(23) (2015). DOI: 10.1103/PhysRevB.92.235132.

153. A. Kreyssig et al.: Pressure-induced volume-collapsed tetragonal phase of $CaFe_2As_2$ as seen via neutron scattering. *Phys. Rev. B* 78(18) (2008). DOI: 10.1103/PhysRevB.78.184517.

154. A. I. Goldman et al.: Lattice collapse and quenching of magnetism in $CaFe_2As_2$ under pressure: A single-crystal neutron and x-ray diffraction investigation. *Phys. Rev. B* 79(2) (2009). DOI: 10.1103/PhysRevB.79.024513.

155. W. H. Jiao, I. Felner, I. Nowik, and G. H. Cao: $EuRu_2As_2$: A New Ferromagnetic Metal with Collapsed $ThCr_2Si_2$-Type Structure. *Journal of Superconductivity and Novel Magnetism* 25(2) (2012), 441. DOI: 10.1007/s10948-011-1287-1.

156. S. Zapf et al.: Persistent Detwinning of Iron-Pnictide $EuFe_2As_2$ Crystals by Small External Magnetic Fields. *Phys. Rev. Lett.* 113(22) (2014), 227001. DOI: 10.1103/PhysRevLett.113.227001.

157. J. Maiwald, I. I. Mazin, and P. Gegenwart: Biquadratic coupling drives magnetic detwinning in $EuFe_2As_2$. *arXiv:1702.00649 [cond-mat.str-el]* (2017).

158. I. R. Fisher, L. Degiorgi, and Z. X. Shen: In-plane electronic anisotropy of underdoped '122' Fe-arsenide superconductors revealed by measurements of detwinned single crystals. *Rep. Prog. Phys.* 74(12) (2011), 124506. DOI: 10.1088/0034-4885/74/12/124506.

159. M. A. Tanatar et al.: Uniaxial-strain mechanical detwinning of $CaFe_2As_2$ and $BaFe_2As_2$ crystals: Optical and transport study. *Phys. Rev. B* 81(18) (2010), 184508. DOI: 10.1103/PhysRevB.81.184508.

160. M. Yi et al.: Symmetry-breaking orbital anisotropy observed for detwinned $Ba(Fe_{1-x}Co_x)_2As_2$ above the spin density wave transition. *Proc. Natl. Acad. Sci. U.S.A.* 108(17) (2011), 6878. DOI: 10.1073/pnas.1015572108.

161. S. Kasahara et al.: Electronic nematicity above the structural and superconducting transition in $BaFe_2(As_{1-x}P_x)_2$. *Nature* 486(7403) (2012), 382. DOI: 10.1038/nature11178.

162. J.-H. Chu, H.-H. Kuo, J. G. Analytis, and I. R. Fisher: Divergent Nematic Susceptibility in an Iron Arsenide Superconductor. *Science* 337(6095) (2012), 710. DOI: 10.1126/science.1221713.

163. C. Dhital et al.: Effect of Uniaxial Strain on the Structural and Magnetic Phase Transitions in $BaFe_2As_2$. *Phys. Rev. Lett.* 108(8) (2012), 087001. DOI: 10.1103/PhysRevLett.108.087001.

164. E. P. Rosenthal et al.: Visualization of electron nematicity and unidirectional antiferroic fluctuations at high temperatures in NaFeAs. *Nat. Phys.* 10(3) (2014), 225. DOI: 10.1038/nphys2870.

165. J.-H. Chu et al.: In-Plane Resistivity Anisotropy in an Underdoped Iron Arsenide Superconductor. *Science* 329(5993) (2010), 824. DOI: 10.1126/science.1190482.

166. J.-H. Chu et al.: In-plane electronic anisotropy in underdoped $Ba(Fe_{1-x}Co_x)_2As_2$ revealed by partial detwinning in a magnetic field. *Phys. Rev. B* 81(21) (2010), 214502. DOI: 10.1103/PhysRevB.81.214502.

167. J. P. C. Ruff et al.: Susceptibility Anisotropy in an Iron Arsenide Superconductor Revealed by X-Ray Diffraction in Pulsed Magnetic Fields. *Phys. Rev. Lett.* 109(2) (2012), 027004. DOI: 10.1103/PhysRevLett.109.027004.

168. Y. Xiao et al.: Field-induced spin reorientation and giant spin-lattice coupling in $EuFe_2As_2$. *Phys. Rev. B* 81(22) (2010), 220406(R). DOI: 10.1103/PhysRevB.81.220406.

169. A. L. Wysocki, K. D. Belashchenko, and V. P. Antropov: Consistent model of magnetism in ferropnictides. *Nat. Phys.* 7(6) (2011), 485. DOI: 10.1038/nphys1933.

170. Y. Su et al.: Antiferromagnetic ordering and structural phase transition in $Ba_2Fe_2As_2$ with Sn incorporated from the growth flux. *Phys. Rev. B* 79(6) (2009), 064504. DOI: 10.1103/PhysRevB.79.064504.

171. C. Wang et al.: Longitudinal Spin Excitations and Magnetic Anisotropy in Antiferromagnetically Ordered $BaFe_2As_2$. *Phys. Rev. X* 3(4) (2013), 041036. DOI: 10.1103/PhysRevX.3.041036.

172. I. Shein and A. Ivanovskii: Elastic properties and chemical bonding in ternary arsenide $SrFe_2As_2$ and quaternary oxyarsenide LaFeAsO – Basic phases for new 38–55K superconductors from first principles. *Physica C: Superconductivity* 469(1) (2009), 15. DOI: 10.1016/j.physc.2008.10.003.

173. A. Jesche et al.: Strong coupling between magnetic and structural order parameters in $SrFe_2As_2$. *Phys. Rev. B* 78(18) (2008), 180504. DOI: 10.1103/PhysRevB.78.180504.

174. K. J. Kurzydlowski and B. Ralph: *The Quantitative Description of the Microstructure of Materials*. CRC Press, Boca Raton, 1995.

175. M. Tegel et al.: Structural and magnetic phase transitions in the ternary iron arsenides $SrFe_2As_2$ and $EuFe_2As_2$. *J. Phys.: Condens. Matter* 20(45) (2008), 452201. DOI: 10.1088/0953-8984/20/45/452201.

176. R. White: The magnetostriction of rare-earth garnets containing gallium and europium: Old theory for new problems. *IEEE Transactions on Magnetics* 9(4) (1973), 606. DOI: 10.1109/tmag.1973.1067701.

177. B. E. Argyle and N. Miyata: Magnetoelastic Behavior of Europium Oxide. II. Magnetostriction and the $\lambda$ Anomaly. *Phys. Rev.* 171(2) (1968), 555. DOI: 10.1103/PhysRev.171.555.

178. J. J. Ying et al.: Measurements of the Anisotropic In-Plane Resistivity of Underdoped FeAs-Based Pnictide Superconductors. *Phys. Rev. Lett.* 107(6) (2011), 067001. DOI: 10.1103/PhysRevLett.107.067001.

179. Y. Shapira, S. Foner, N. F. Oliveira, and T. B. Reed: EuTe. II. Resistivity and Hall Effect. *Phys. Rev. B* 5(7) (1972), 2647. DOI: 10.1103/PhysRevB.5.2647.

180. Y. Shapira, R. Kautz, and T. Reed: Positive magnetoresistance due to conduction-band splitting in EuSe and EuTe. *Physics Letters A* 47(1) (1974), 39. DOI: 10.1016/0375-9601(74)90096-6.

181. M. Sugishima, H. Wada, A. Mitsuda, A. Kondo, and K. Kindo: Large magnetoresistance of $EuPtP_{1-x}As_x$. *Phys. Status Solidi B* 252(12) (2015), 2784. DOI: 10.1002/pssb.201552370.

182. A. Maurya, P. Bonville, A. Thamizhavel, and S. K. Dhar: $EuNiGe_3$, an anisotropic antiferromagnet. *J. Phys.: Condens. Matter* 26(21) (2014), 216001. DOI: 10.1088/0953-8984/26/21/216001.

183. K. Ishii, A. Fujiwara, H. Suematsu, and Y. Kubozono: Ferromagnetism and giant magnetoresistance in the rare-earth fullerides $Eu_{6-x}Sr_xC_{60}$. *Phys. Rev. B* 65(13) (2002), 134431. DOI: 10.1103/PhysRevB.65.134431.

184. Y. Xiao et al.: Anomalous in-plane magnetoresistance in a $EuFe_2As_2$ single crystal: Evidence of strong spin-charge-lattice coupling. *Phys. Rev. B* 85(9) (2012), 094504. DOI: 10.1103/PhysRevB.85.094504.

185. I.-M. Pietsch: Thermal expansion and magnetostriction measurements of $EuFe_2(As_{1-x}P_x)_2$. MA thesis. University of Göttingen, 2014.

186. C. GmbH: *http://crystal-gmbh.com/de/products/substrates.php*. 2015.

187. G. Kresse and J. Hafner: Ab initiomolecular dynamics for liquid metals. *Phys. Rev. B* 47(1) (1993), 558. DOI: 10.1103/PhysRevB.47.558.

188. I. I. Mazin, M. D. Johannes, L. Boeri, K. Koepernik, and D. J. Singh: Problems with reconciling density functional theory calculations with experiment in ferropnictides. *Phys. Rev. B* 78(8) (2008), 085104. DOI: 10.1103/PhysRevB.78.085104.

189. P. Villars and K. Cenzual, eds.: *$EuFe_2As_2$ Crystal Structure: Datasheet from "PAULING FILE Multinaries Edition – 2012" in SpringerMaterials*. http://materials.springer.com/isp/crystallographic/docs/sd_1628054.

# *Acknowledgements*

This project would not have been possible without the help of many people. First and foremost, I'd like to thank my supervisor Philipp Gegenwart for giving me the opportunity to work at his chair and for dealing with the administrative aspects of research in the background, leaving me the freedom to conduct my research mostly independently.

I also like to thank Hans-Albrecht Krug von Nidda for agreeing to be the second referee and Michael Lang from the University of Frankfurt for agreeing to be the external referee of this thesis.

I am grateful to Igor I. Mazin from the Naval Research Laboratory in Washington for his guidance and advice during the development of the microscopic detwining theory. I admire your dedication not only to science in general but also to teaching, which lead to us discussing our research even on weekends and high holidays. Thank you so much!

I also like to thank my various other collaborators, who tremendously helped to uncover and finally explain this intriguing magnetic detwinning effect. Shibabrata Nandi from the Indian Institute of Technology in Kanpur and Yinguo Xiao from the Forschungszentrum Jülich for conducting with me the neutron scattering experiments that finally proved the persistent magnetic detwining effect directly. H. S. Jeevan and Shuai Jiang both for providing reference samples on the parent compound, and H. S. Jeevan for additional P-doped single crystals. Also Christian Stingl, for allowing me to use his magnetostriction and thermal expansion data on the $EuFe_2As_2$ system, for introducing me to the dilatometric measurement technique, and for his willingness to always answer my questions, no matter how trivial they might have been. Sina Zapf and Martin Dressel from Stuttgart University for their prolific cooperation at the beginning of this project that led to the discovery of the persistent multistage magnetic detwinning effect in $EuFe_2As_2$. Furthermore, I thank Anton Jesche for his support during the crystal growth and general characterization phase of this project, and Sebastian Esser for conducting the AFM experiment on the Ru-doped sample. To all my collaborators, I am thankful for all the fruitful discussions we had over the years!

I thank Friedrich Freund, for his help and the pleasant atmosphere in our office. You are not only an awesome officemate, but also a friend! I always enjoyed our activities together! I am grateful to Patrick Seiler, for our intriguing and insightful conversations, whether we discussed issues of physics, society, religion or everything else under the sun. I particularly enjoyed your theoretical insights and the "mental rigor" you applied to our debates. Also, the "experimentalist meets theoretician" situations where hilarious: "No,

it's not sheet resistance...". I also thank German Hammerl for all the joyful discussions. I always admired your love of physics and your dedication to teaching! Furthermore, I like to express my gratitude to Veronika Fritsch and Alexander Tsirlin for their invaluable advice and guidance.

I feel indebted to our technical staff, in particular, Alexander Herrnberger and Klaus Wiedenmann, for their incredible lab-support, the invaluable help with the development of the in-box arc melter, the setup of the high-temperature tube furnaces, the helium supply, and their assistance with countless other technical issues. I would also like to acknowledge Eleonore Saladie, Christine Schäfer, Birgitta Eisenschmid, Chenh Dung Lai, the mechanics workshop, and, of course, the entire chair of EP VI for the support during this work. I thank you all!

Additionally, I'd like to thank all persons who were involved in proofreading this thesis, especially Veronika Fritsch and Alexander Tsirlin.

Finally, I am deeply grateful to my friends and family and, in particular, my mother! Putting up with me during the more stressful periods of this project must not have been easy. Without you I would not be where I am today!